Modelling of Contact Interfaces using Non-homogeneous Discrete Elements to predict dynamical behaviour of Assembled Structures

Vom Fachbereich Maschinenbau
an der Technischen Universität Darmstadt

zur

Erlangung des akademischen Grades Doktor-Ingenieur (Dr.-Ing.)
genehmigte

Dissertation

vorgelegt von

Anuj Sharma M.Sc

aus Shyamnagar - Indien

Berichterstatter:	Prof. Dr.-Ing. T. Melz
Mitberichterstatter:	Prof. Dr.-Ing. B. Schweizer

Tag der Einreichung:	20.06.2016
Tag der mündlichen Prüfung:	02.11.2016

Darmstadt 2017

D17

Erklärung

Hiermit erkläre ich, dass ich die vorliegende Arbeit, abgesehen von den in ihr ausdrücklich ge-nannten Hilfen, selbständig verfasst habe.

Ludwigsburg, den 20.06.2016

____________________________-

(Anuj Sharma)

Acknowledgement

This work was written during my three-year scholarship time in the work-group *Design for Vibration Reliability and Mechanics*, Robert Bosch GmbH, in close cooperation with the *Department of Adaptronics*, Fraunhofer Institute for Structural Durability and System Reliability LBF and *Department of Mechanical Engineering*, Technical University Darmstadt.

My special thanks to Prof. Dr.-Ing. Tobias Melz, Head of System Reliability and Machine Acoustics Group, Technical University of Darmstadt, for accepting to guide the thesis with keen interest and providing many valuable suggestions during different stages of the work. My sincere thanks to Prof. Dr.-Ing. Bernhard Schweizer, Head of the Institute of Applied Dynamics, Technical University of Darmstadt, for accepting to be co-referee of the thesis.

I thank Dr. rer. nat. Wolfgang Mueller-Hirsch, head of the *Design for Vibration Reliability and Mechanics* team, Robert Bosch GmbH, for the consistent motivation and support in accomplishment of the work. Furthermore, I thank Dr.-Ing. Sven Herold, head of the *Structure Dynamics and Vibration Technology* department of Fraunhofer Institute for Structural Durability and System Reliability LBF, for the valuable technical suggestions and guidance during the important phases of the work.

My sincere thanks to all my colleagues in the working group - especially to Mr. Lutz Merkle and Mr. Matthias Webber for always being available to have discussion on all possible technical and non technical issues.

A big thank to my family for unconditional support and love imparted during my research career. Many thanks to all my friends for a joyful time in Germany.

Ludwigsburg, June 2016
Anuj Sharma

Contents

List of Symbols

A	Contact area
C_{ijkl}	Compliance tensor
E	Young's modulus of elasticity
E^*	Equivalent elastic constant for two spheres in contact
F_d	Damping force
F_c	Coulomb limiting force of sliding
F_d	Dissipative force
F_N	Normal force
F_T	Tangential force
F_bv	Equivalent normal bolt force
F_el	Elastic restoring force
F_ext	External force
F_k	Frictional force for dynamic friction condition
F_{nl}	Non-linear force
F_s	Frictional force for static friction condition
G	Shear modulus of elasticity
G^*	Equivalent shear modulus for two spheres in contact
H	Hardness of the material
$H(\omega)$	Transfer function
J	Squared error
K_N	Normal contact stiffness density
K_T0	Tangential contact stiffness density
M_b	Bolt torque moment
N_H	Number of harmonics
N_e	Number of elements
P_N0	Initial pressure
P_N1	Saturation pressure as transition point between non-linear and linear regions
P_m	Pressure at which maximum damping exists
$P_\mathrm{m}^\mathrm{loc}$	Location parameter used in Rayleigh damping distribution
R	Radius of the sphere in hertzian thoery
R	Residuum
R^*	Equivalent radius of two spheres in contact
R_A	Radius of the asperity

T_{IFFT}	Inverse Fourier transformation matrix
U_0	Amplitude of steady state displacement response
U_{max}	Potential energy
ΔE	Energy dissipation per cycle
ΔW	Dissipative work
Δt	Time step
Λ	Eigen-value
Ω	Body
Φ	Scaled mode-shape matrix
Σ	Singular value
α_{r}	Mass multiplier- Rayleigh damping constant
β	Newmark parameter
β_{hys}	Hysteretic damping constant
β_{r}	Stiffness multiplier- Rayleigh damping constant
$\boldsymbol{D}$	Damping matrix
$\boldsymbol{K}$	Stiffness matrix
$\boldsymbol{M}$	Mass matrix
$\boldsymbol{q}$	Modal displacement vector
$\boldsymbol{t}$	Traction vector
$\boldsymbol{u}$	Displacement vector
χ_{ln}	Scaling facctor for Log-normal damping distribution
χ_{n}	Scaling factor for Normal damping distribution
χ_{r}	Scaling factor for Rayleigh damping distribution
$\ddot{\boldsymbol{q}}$	Modal acceleration vector
$\ddot{\boldsymbol{u}}$	Acceleration vector
$\ddot{u}$	Acceleration
δ_{N0}	Initial distance between the reference planes of two rough surfaces approaching contact
δ_{NC}	Critical interference
δ_{N}	Relative normal displacement or penetration
δ_{Tmax}	Maximum tangential displacement at start of sliding
δ_{T}	Tangential relative displacement
$\dot{\boldsymbol{q}}$	Modal velocity vector
$\dot{\boldsymbol{u}}$	Velocity vector
$\dot{\delta}_{\text{T}}$	Tangential relative velocity
$\dot{u}$	Velocity
$\dot{u}_s$	Stribeck velocity coefficient
η	Loss factor
η_{loc}	Localized contact damping loss factor
γ	Newmark parameter
$\hat{u}$	Nodal displacement
κ	Hardness factor

λ	Curvature parameter used in exponential pressure-penetration law
λ_c	Dimensional constant used in modified exponential distribution
e_i	Error
h_i	Measured transfer function
μ	Coefficient of friction
μ_k	Coefficient of dynamic friction
μ_s	Coefficient of static friction
μ_{bolt}	Coefficient of friction for bolt circumference
μ_{head}	Coefficient of friction under bolt
ν	Poisson's ratio
ω_d	Damped natural circular frequency
ω_m	Modal angular frequency
ω_n	Natural circular frequency
$\partial\Omega$	Boundary of the body
ϕ_{mexp}	Modified exponential probability distribution
ρ	Density
ρ_{cu}	Density of copper
ρ_{preg}	Density of prepreg
σ_d	Damping constant
σ_0	Initial slope of force-deflection curve in Dahl friction model
σ_{n}	Standard deviation for Normal or Log-normal damping distribution
σ_{ij}	Stress tensor
τ	Tangential stress
$\tilde{u}$	Approximate displacement
ε_{ij}	Stress tensor
ξ_{m}	Modal damping ratio
ζ	Damping ratio
a_k	Numerator coefficient of transfer function
b_i	Body forces
b_k	Denominator coefficient of transfer function
c	Dimensional constant used in modified exponential distribution
c_{k}	Constant used for smooth transition in calculation of stiffness
d	Damping of single degree of freedom
$d(x,y)$	Localized discrete damping over contact surface
d^{∞}	Damping stabilizer in Inverse absolute damping
d_{cr}	Critical damping coefficient
d_{eqv}	Equivalent visco-elastic damping coefficient
d_{head}	Average diameter of bolt head
d_{ms}	Damping in micro-slip region
d_{nom}	Nominal diameter of bolt
d_{sl}	Damping in slip region
d_{st}	Damping in stick region

d_{loc}	Localized damping constant
g_{N0}	Initial normal gap
g_{N}	Normal gap
g_{T0}	Initial tangential gap
g_{T}	Tangential gap
i	Slope-curvature parameter in Dahl friction model
k	Stiffness of single degree of freedom
k_{N}	Normal contact stiffness
k_{T0}	Initial tangential stiffness
k_{nl}	Non-linear cubic stiffness used in duffing oscillator
k_{ε}	Penalty stiffness
m	Mass of single degree of freedom
$p(r)$	Hertzian pressure distribution
p_0	Maximum Hertzian at centre of contact area
p_k	Pole of transfer function
p_{N}	Normal contact pressure
r	Radius
r_{C}	Contact radius
r_{S}	Contact radius for the stick circular zone
s_{k}	Switching function
t	Time
u_x	Tangential displacement in x direction
u_z	Normal displacement
w	Test function

Abstract

In this dissertation a new approach of modelling contact interfaces with equivalent discrete elements is presented. Various fastening techniques used for assembling structures not only account for transfer of loads but also adds damping to the structure. With vast usages of the jointed structures, the effect of contacts on the global dynamical behaviour of an assembled structure is of prime interest. Assembled structures with contact interfaces show a non-linear behaviour, with a predominance of the local energy dissipation at interfaces in comparison to the inherent material damping losses. With increasing complexity of structures used in the industrial applications, a continuous demand of robust and efficient numerical modelling exists for a better prediction of the system behaviour. Hence, numerical models capable of predicting the dynamic behaviour to good accuracy can be used as a replacement for expensive experimental investigations.

Various theoretical and empirical models have been successful in capturing the influence of the non-linearity induced through the contact interfaces, but their implementation for complex and large structures experience convergence difficulties with high computational time. To improve the computational cost, frequency domain description based on family of Harmonic Balance Methods provide a good alternative, but they have been restricted to cases involving periodic excitations. This thesis describes an equivalent localized discrete contact model, which can predict the effects of contact non-linearity on the dynamical behaviour of structure with considerable enhancements on the computational time efficiency. The proposed notion is to use an explicit non-homogeneous description to en-capture the global non-linear behaviour and a local linearized definition to retain the advantages of a linear system.

The new approach used in modelling of contacts is based on the characterization of discrete spring-damper system at the contact interface. A Damped-Pressure Dependent Joint (D-PDJ) model is developed to obtain the required local contribution of the contact stiffnesses and damping. The normal and tangential contact stiffnesses are calculated from the resulting contact pressure, based on a modified exponential pressure-penetration law and Mindlin law respectively. The contact damping is defined through the use of the discrete hysteretetic-structural damper elements at the contact interface. Based on numerical investigation for a beam fastened with a bolted joint, regions of stick, micro-slip and slide are defined. The numerical investigations show that the maximum dissipation is obtained in the micro-slip region. A Rayleigh probability distribution function based on the contact pressure is chosen for describing the contact damping distribution over the interface, with parameters governing the position of the maximum damping and magnitude of damping.

Quantitative experimental validations of the proposed D-PDJ model are done for a set of test structures. The first test structure is a double layered beam (made of stainless steel) fastened with four M6 bolted joints. The double layered beam structure is used to study the influence of operational factors such as bolting torque and excitation amplitude. Later, a copper-prepreg-copper plate is fastened between the beams to study the influence of contact pair of different materials. All investigations have shown good correlation between the experiment and simulation results for test structure experiencing moderate non-linearity (bolting torque 3 Nm and 5 Nm) in comparison to strong non-linearity (bolting torque 1 Nm). The second test structure is a set of prototype structures to resemble a large and complex structure like Electronic Control Unit (ECU). The first prototype structure is a system resembling an Engine ECU, having large contact area with localized pressure distribution near the bolt region. The Experimental Modal Analysis (EMA) results when compared to D-PDJ model showed good correlation till 2 kHz, with the results of the modal damping highly appreciable. Also, the result's accuracy and computational time efficiency have proved to be significantly better than the conventional methods. The second prototype structure is a system resembling an Airbag ECU. The second prototype structure verifies the use of model having combination of material and contact non-linearities. The comparison for the transmissibility results showed good match between the experiment and D-PDJ simulation, for base excitation setup of the prototype structure.

The proposed D-PDJ model has shown good match with various sets of experimental results and is concluded to have the capability of describing the dynamical behaviour of the assembled structures with moderate non-linearity. Also, the significant reduction in computational time motivates its usage for the complex and large structures used in industrial application.

Zusammenfassung

In dieser Dissertation wird ein neuer Modellierungsansatz für Kontaktverbindungen mit äquivalenten diskreten Elementen vorgestellt. Verschiedene Fügetechniken übertragen nicht nur die Lasten in einer Struktur sondern bringen auch eine Dämpfung ein. Wegen der breiten Verwendung von geschraubten Verbindungen, hat der Einfluss von Kontakten auf das dynamische Verhalten grösste Bedeutung. Zusammengefügte Strukturen mit Kontaktstellen zeigen ein nichtlineares Verhalten. Dominant ist dabei die lokale Energiedissipation, im Gegensatz zu den inneren Verlusten durch die Materialdämpfung. Bei steigender Rechenleistung und Verwendung von komplexeren Strukturen in der industriellen Anwendung, gibt es einen grossen Bedarf an robuster und effizienter numerischer Modellierung. Ziele sind eine bessere Prognose des Systemverhaltens und teure Experimente zu ersetzen.

Zahlreiche analytische und empirische Modelle wurden erfolgreich für die Bestimmung der Nichtlinearitäten auf Grund der Kontakte entwickelt. Aber die Implementierung von komplexen, realen Anwendungen verursachen Schwierigkeiten bei der Konvergenz und der Rechenzeit. Wenn man die Rechenzeit reduzieren möchte und deshalb versucht, die Berechnung auf Basis der harmonischen Balance Methoden im Frequenzbereich zu formulieren, so ist diese auf eine periodische Anregung beschränkt. Diese Dissertation beschreibt ein vergleichbares lokales diskretes Kontaktmodell von Schraubverbindungen, welches die Effekte der Kontakt- oder Grenzflächen-Nichtlinearität auf das dynamische Verhalten vorhersagt bei gleichzeitiger effizienter Berechnung hinsichtlich der Rechenzeit. Diese Idee wird durch eine explizite und inhomogene Beschreibung begründet, um das gänzlich nichtlinearen Verhalten zu erfassen. Gleichzeitig aber wird lokal eine Linearisierung behalten.

Die Neuheit des Kontaktmodellierungsansatzes basiert auf der Charakterisierung von diskreten Feder-Dämpfer-Elementen an den Kontaktstellen. Es wurde eine gedämpfte, druckabhängige Kontaktverbindung (Damped-Pressure Dependent Joint D-PDJ) entwickelt, um den erforderlichen Beitrag der Kontaktsteifigkeit und -dämpfung zu erhalten. Die Normal- und Kontaktsteifigkeit werden aus dem resultierenden Kontaktdruck berechnet, welcher auf einer exponentiellen Druck-Durchdringungs-Abhängigkeit basiert. Die Definition der Kontaktdämpfung geht aus der Hysterese von diskreten Struktur-Dämpfungs-Elementen am Kontaktbereich hervor. Eine verallgemeinerte Schraubverbindung weist Bereiche von Haftreibung, Mikroschlupf und Gleitreibung auf, wobei die maximale Energiedissipation im Mikroschlupfbereich stattfindet. Es wird eine Rayleighverteilungsfunktion verwendet, um die lokale Kontaktdämpfungan der Grenzschicht zu beschreiben. Der Parameter, welcher die Stelle der maximalen Dämpfung bestimmt, folgt aus dem vorher berechneten Kontaktdruck.

Das vorgestellte D-PDJ-Modell wurde mit einer Reihe von Teststrukturen experimentell validiert. Die erste Teststruktur ist ein Doppelbalken aus rostfreiem Stahl mit vier M6-Schraubverbindungen zur Analyse von realen Einflussparametern wie dem Drehmoment oder der Anregungsamplitude. Eine Kupfer-Prepreg-Kupfer-Platte wird zwischen zwei Balken geschraubt, um den Einfluss der Kontaktpaarungen von verschiedenen Materialien zu untersuchen. Alle Untersuchungen zeigen eine gute Übereinstimmung zwischen dem Experiment und der Simulation bei einer moderaten Nichtlinearität (Drehsmoment von 3 Nm und 5 Nm) im Vergleich bei einer starken Nichtlinearität (Drehsmoment von 1 Nm). Die zweite Teststruktur ist eine vereinfachte Bauweise eines elektronischen Steuergerätes mit grosser Kontaktfläche zwischen den Materialpaarungen. Die erste untersuchte Teststruktur ähnelt einem Motorsteuergerät mit grossen Kontaktflächen mit einer lokalen Druckverteilung in der Nähe der Schraube. Die experimentellen Ergebnisse im Vergleich mit dem D-PDJ-Modell zeigen sehr gute Übereinstimmung bis 2 kHz, ebenso die modalen Dämpfungen. Die Genauigkeit der Ergebnisse und die effiziente Rechenzeit sind nachweislich besser als bei kommerziellen Softwareanbieter. Die zweite Teststruktur, welche einem Airbag-Steuergerät ähnelt, wird verwendet, um Materialkombinationen und Kontakt-Nichtlinearitäten zu überprüfen. Die Ergebnisse der D-PDJ-Simulation zeigen eine gute Übereinstimmung der Übertragungsfunktion zu den im Experiment angeregten Strukturen.

Das vorgestellte D-PDJ-Modell zeigte eine gute Übereinstimmung zwischen verschiedenen experimentellen Ergebnissen und hat folglich auch die Fähigkeit, das dynamische Verhalten von schwach-nichtlinearen Strukturen beschreiben zu können. Ferner begünstigt die signifikante Reduktion der Berechnungszeit die Anwendbarkeit auf komplexere und grössere Strukturen der industriellen Anwendung.

Chapter 1

Introduction

1.1 Motivation

With the advent of smart control systems through the electronic circuits, the various operations of an auto-mobile are governed through different Electronic Control Units (ECU). Some of the examples are: Engine ECU controls the operations of an engine like throttle control, ignition, triggering etc., Airbag ECU's detect the crash situation and deploys the Airbag for passenger safety, ESP controls the stability of the vehicle on curved roads. It is imperative that the different sensors placed in the ECU function according to the requirements in the field conditions. For example, the Engine ECU is exposed continuously to excitations from the road conditions and the vibrations of the engine assemblies. Due to these excitations, complete ECU experiences dynamic loads, resulting in the excitation of the structural modes of the electronic components. This might result in higher amplitudes of vibration of the corresponding electronic components, which for a long duration of excitation results in the fatigue failure of the components .

To ensure the proper functionality of the ECU modules, tests are performed both in the field and equivalent laboratory conditions. This is required before release of any ECU for series production. The experimental methods account for high costs with large time involved. Also, it is a cumbersome process to perform tests for each of the modification done in the system. On contrary, the mass production does raise the question of how many test are sufficient to ensure no functional failure. An alternative to performing many experiments is the use of the simulation models to predict the dynamic behaviour of the systems.

The simulation models are not only capable of predicting the system behaviour in short duration of time but also provide important information, which is not possible to be measured. The simulation can further be used for studying the changes in the system behaviour for any change in both external and internal factors like temperature, excitation type, humidity and type of material, dimensions respectively. However, first a mathematical model describing the correct physics of the system is required and later its im-

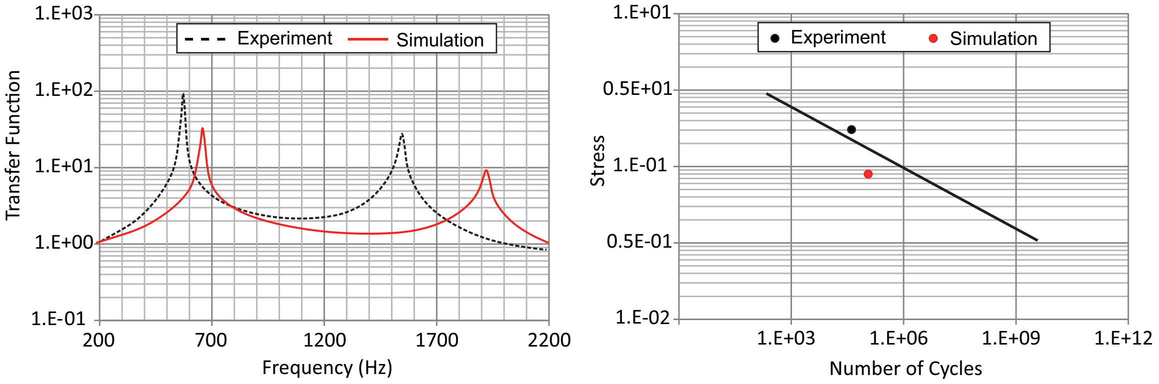

(a) High cycle fatigue.

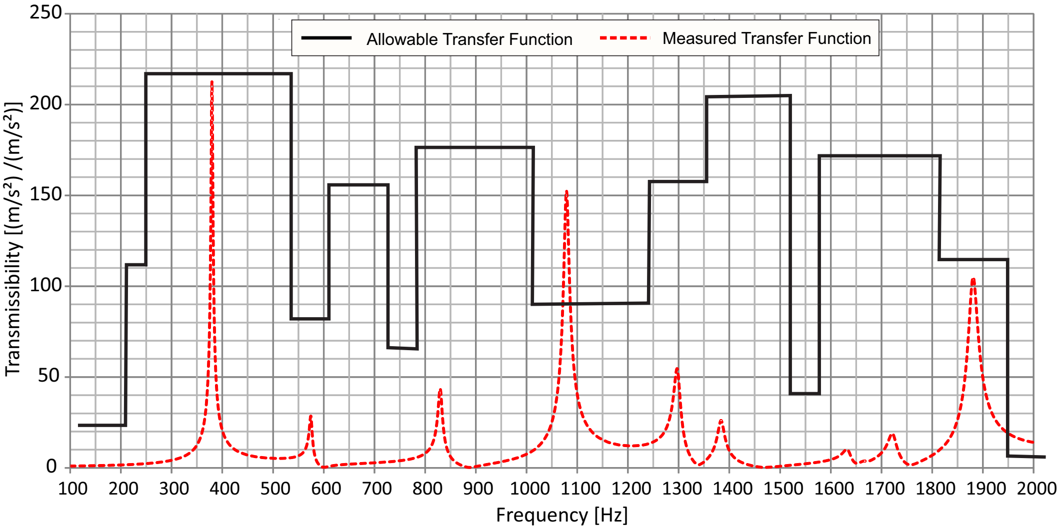

(b) Allowable amplitudes of vibration.

Figure 1.1: Use of the simulation models for predicting the dynamic behaviour of structure to be used in making fatigue calculations and investigation if the system response is with-in allowable limits.

plementation to give sensible and accurate results. Among different applications, some of the conventional use of the dynamic simulation models is the prediction of fatigue life of the electronic components mounted in the ECU. If the simulation do not predict the correct resonance frequencies and the peak amplitudes of vibration in comparison to the experimental behaviour, the fatigue damage estimation based on the S-N curve could suggest that the simulation shows no failure but in reality it has risk of failure. Other application is to test whether the response spectrum on the sensors lies within the all allowable threshold limits. In this case too, if simulation predicts non-accurate resonance frequencies and damping, the estimations based on the simulation results are not reliable. These two examples have been shown in figure 1.1.

The simulation models are hence required to be reliable to make good predictions of the dynamic behaviour of structure. For the vibrational behaviour of systems, required is the correct estimations of the resonance frequencies and amplitude of oscillation. Among different influencing factors on the dynamic behaviour, one of the most influencing factor of assembled structure like ECU is the non-linear effects induced through the contact interfaces. If the correct material properties and proper contact modelling approach is used, an accurate prediction of the resonance frequency and damping of the system can be obtained. This can enhance the prediction quality of the for fatigue life estimation too. This thesis presents an efficient contact modelling approach that can be utilized for the large system like ECU and have a good prediction of the dynamic behaviour.

1.2 Literature Survey

History of Friction. The earliest work of DA VINCI (1519) is attributed as the first work introducing the concept of friction. He showcased experimentally different kinds of friction like the sliding friction, rolling friction etc. His main observations were that the contact area has no influence on the frictional forces and there exists a linear proportionality between the loading and friction force. However, the first published results for friction theory come from findings of AMONTONS (1699), who essentially rediscovered the findings of the DA VINCI. AMONTONS idea of friction is based on the deformation of asperities under external loading. One of the most important contribution in describing the phenomenon of adhesion is attributed to the work of DESAGULIER (1724). Adhesion was explained based on an experiment performed with two lead balls, wherein the two lead balls were first loaded towards each other and then loaded in opposite directions to separate them. COULOMB (1781) provided the idea of modelling the surface roughness as the profile of wedges, such that the friction is defined as the work done in sliding over inclined wedge surface. Using this principle, the first tribometer to measure the coefficient of friction was designed. He studied the main influencing factors on the friction like - the material pairing, actual contact area, contact force etc. under different settings of temperature, humidity and vacuum conditions. His initial observation converged with AMONTONS findings that the friction is almost linear dependent on the loading and independent of the apparent contact area. He also established that the dynamic friction in general is smaller than the static friction, but for metals the difference is negligible. Coulomb model did not include the concept of frictional dissipation, as the concept of dissipation was unknown by that time in the scientific community. RENNIE (1829) further validated Coulomb's observations with other experimental set-up. He observed few more interesting things like the predominant influence of contact pairing materials on the coefficient of friction and the reduction in the friction with increasing duration of machine in-operation. STRIBECK (1902) further extended the COULOMB model for describing the lubricated contact and including the influence of viscous effects or the effect of the velocity on the friction. There are many studies made in the field of friction, but the Coulomb model still remains one of the most used and simplified ways of the modelling the frictional behaviour of bodies in contact.

Analytical Contact Models. HERTZ (1881) was one of the first among to provide analytical description for the contact between continuous non-conforming surfaces of solid bodies. The Hertzian theory comprises of formulations to determine the deformation of mating surfaces, contact pressure over contact interfaces, stresses in the body, contact area etc., under the external normal loading. However, the formulations were derived with few assumptions like only small strains are possible, the contacting surface are frictionless, the bodies in contact are isotropic and the contact area radius is negligibly smaller in comparison to the elastic bodies curvature radius. The constitutive formulations derived based on Hertzian theory gave foundation for many succeeding contact models developed later by other authors.

The successive model based on Hertzian theory started with relaxing the assumption taken by Hertz model and deriving more generalized formulations. SNEDDON (1968) reformulated the constitutive relations with relaxing the assumption of smaller contact radius in comparison to the curvature radius of contact surfaces. SPENCE (1968) extended the Hertz model for fully adhered contact and hence relaxing the assumption of frictionless condition. WILLS (1966) [120] used the numerical contour integration based on the fourier transformation to determine the dimensions of the contact area. The formulation extended the Hertzian theory for contact between anisotropic bodies. Later TURNER (1979) [113] also presented the formulations for transverse isotropic contact bodies, with formulation having similar representation as used for the isotropic hertzian contact. SWANSON [110] presented a general procedure to calculate stresses for orthotropic materials in contact. He combined methods of WILLS (1966) and PAGANO (1970) to calculate the contact size and aspect ratio for transverse loading of laminated orthotropic materials.

Further scope of extensive study on normal contact model was followed with studying and formulating the influence of the surface roughness on the constitutive relations. The Hertzain theory is capable of calculating of contact area at different contact spots, but it depends on the radius of asperity, which is unknown [43]. Hence, the relation between the contact area and loading is not possible for large surface possessing roughness. The contact between two bodies occurs at different peaks of the roughness. HOLM and BOWDEN AND TABOR explained that although the overall stresses are in the elastic range, there exists plastic deformation at the contact spots. Also, each contact spot can be visualized as a small hardness indentation [43]. Hence, the mean contact pressure can be taken as the hardness of contacting material and there exists no dependence on the loading and contact geometry. ARCHARD (1957) opposed the argument by stating that the asperities can deform plastically for initial loadings traversals but over long duration they would reach to a steady state behaviour and hence lead to elastic behaviour. BOWDEN AND TABOR used the term asperity, where as ARCHARD description of a local roughness was based on the concept of *protuberance on protuberance on protuberance*. ARCHARD explained the two ideas of influence of loading on contact area i.e. *increase in the loading leads to formation of new contact areas or increase in the size of the present contact area*. For cases where the number of contact areas remains constant, there exists a non-linear relation between the loading and contact area. For increase in number of contacts with no relative increase in average contact size, there exists a linear relation between the loading and the contact area.

GREENWOOD AND WILLIAMSON (1966) model is one of the most important work in developing constitutive relations for the normal contacts with inclusion of surface roughness effects. It was clear by then that for very rough surfaces the contact behaviour will be plastic and for smooth surfaces the contact behaviour will be elastic. GREENWOOD AND WILLIAMSON (1966) presented their first work in modelling the nominally flat surfaces in contact. The idea was to characterize the roughness as a probability distribution function to have a statistical estimation for number of asperities and number of asperities in contact. Initially a Gaussian distribution was chosen to characterize the surface roughness, which was later updated with easy choices of exponential distribution [44] to yield an closed form analytical solutions. CHANG ET.AL [21] later provided the solution for the GREENWOOD AND WILLIAMSON model for the elastic-plastic deformation, with the old approximation of the Gaussian distribution of surface roughness.

Primitive studies on the frictional behaviour of bodies in contact ideally constitute to the tangential contact models. The analytical model for the tangential contacts as an extension to Hertzian theory of curved bodies was presented by CATTENO (1938) and MINDLIN (1949). Although the authors had worked independently but they proposed similar results. The model defined a constitutive relation to determine the tangential stresses for the bodies in contact under quasi-static loading. The most important outcome of the CATTENO (1938) and MINDLIN (1949) models is the definition and inclusion of the partial slip phenomenon in the constitutive formulations. When two non-conforming bodies are in contact and a tangential load is applied, there will be regions in the contact area which are sliding and regions which are not sliding. This state is defined as the partial slip state. Later, MINDLIN (1951) extended the model for oscillating loading and presented the hysteresis behaviour between the tangential forces and the relative motion. The dissipative work associated with hysteresis of partial slip was presented, whose formulations were different for loading and reloading stages. COURTNEY-PRATT AND EISNER (1957) studied the effect of tangential loading on metallic bodies in contact and associated the partial slip behaviour under a periodic loading as a reason to the fretting corrosion phenomenon.

The dynamic modelling of frictional contact constitute to study of the frictional behaviour with respect to macroscopic time variants like velocity. The most common application of dynamic friction modelling of rigid bodies is found in control systems. AMONTONS or COULOMB model's description of friction phenomenon is characterized by discontinuity at transition from stick to sliding state. For the continuity of the friction behaviour, it is characterized by a pre-sliding state, which exists before the complete sliding. DAHL (1968) described the pre-sliding behaviour as a smooth transition from stick to sliding state. The frictional contact is idealized as a mechanical bond, which breaks for the tangential forces exceeding the bond breaking limit. DAHL made the analogy of frictional behaviour with structural mechanics behaviour of ductile material, wherein the yield point refers to the transition point of stick to slide state. The contact between two surfaces was characterized as a brush, wherein each bristle associates to the individual asperity contact. Hence, the modelling is defined as frictional model based on both macroscopic and microscopic variables, where the macroscopic variable is the gross movement of brush and the microscopic variable is the movement of each bristle.

Extension to DAHL model was first presented by CANUDAS DE WIT ET AL. (1995) [32] referred as LuGre model. The Dahl model was suitable for only dry frictional contacts, while it is also known from Stribeck effect that the friction effects reduce with increase in velocity under certain regimes. The LuGre model brings in the viscous effects in the constitutive formulation to capture the Stribeck effect. The LuGre model replaced the velocity independent friction force used in Dahl model with velocity dependent function. Also, two other terms associated with macroscopic displacement and macroscopic velocity were included in the formulation. The model finds its application for lubricated contact interfaces, wherein the parameters used in the model are obtained from experiments. Extension to LuGre model was presented by SWEVERS ET AL. (2000) [111] and is often referred as Leuven model. The motivation was to include the missing pre-sliding behaviour with reversal point memory in LuGre model. The Lueven model is also referred as an integrated friction model, as it comprises of two equations i.e. friction force equation and the state variable equation. Although this model was a representation near reality, it had difficulties in numerical implementation. The two most known disadvantages were discontinuity in friction force at the closing of hysteresis loop and the stack overflow. A modified Leuven model was presented by LAMPAERT ET.AL (2002) [59] to resolve the mentioned disadvantages, with reformulation of present form and use of discrete elements to model elasto-plastic behaviour. The discrete modelling was the motivation from the conventional discrete Maxwell-slip model. BOUC-WEN model is another improved model, where BOUC presented the hysteresis behaviour for quasi-static loading and WEN presented the evolution equation involving the state variables. Another more generalized form was presented by DUHEM, wherein using maximum number of parameters, all above discussed models can be described with a single formulation.

Experimental Observations. Most of the historical work in frictional contact was studied through experimental investigations, based on which the formulations describing friction phenomenon were developed. Experimental investigations to understand the contact dissipation phenomenon under dynamic excitations were started in 1950's. GOODMAN AND KLUMPP (1956) presented the first detailed work to study the effect of the joints on the dynamics of structure, like Turbines. The turbines have high stresses at resonance, which lead to fatigue damage. GOODMAN AND KLUMPP (1956) proposed the use of joints, such that the addition of damping from the joints leads to reduction of stresses. The important finding of their study was that at some optimum pressure (not high and not low), a high amount of damping from joints can be achieved. Hence, an efficient design of joints with an optimum pressure adds maximum damping to the structure, thus lowering the stress and improving the fatigue life of structure. The other important observation was that the dissipation through the inherent properties of material is less than the dissipation associated with the joints. They also established that the friction coefficient is velocity dependent and can vary in small values for increased number of cyclic loading, which was against the findings of the Coulomb model. However, till date engineers like to keep frictional coefficient constant for most of applications to avoid complexity. Goodman (1959) extended the observations from experiment to establish a power law between the input force and the energy dissipated per cycle. For the Coulomb friction, the exponent of power law was found to be 3. This was later reconfirmed based on experimental investigation of a lap-joint under uniform clamping pressure by Metherell and Diller (1968). Lazan and Goodman (1961) performed experiments to distinguish between the dissipation associated with only material characteristics and dissipation associated with the joints. While the dissipation associated with material deformation is characterized by the plasticity phenomenon, the dissipation associated with joints were characterized by friction phenomenon.

Ungar (1973) performed experiments to define the dissipation in structural members as structural damping, wherein the dissipation is caused due to the friction between different planes of the structural material. A detailed experimental study was performed to show the effects of the type and orientation of loading on the contact dissipation. Important observation was that the dissipation for the dry contact is due to the micro-slip behaviour and the dissipation for the lubricated contacts is predominantly due to the viscous effects. Rogers and Boothroyd (1975) presented one of the most important observation for the dry contacts i.e. the frictional joint damping is independent of the frequency of excitation. They performed experiments and fitted the measured hysteresis curve with discrete model based on Masing (1923) model. Further experimental investigations which are often cited by authors relates to work done by Beards (1975). He performed a series of experiments to show that the predominance of the damping is due to the joint damping, in comparison to the material damping. Also, quantitative study was performed to observe the influence of the contact pressure on the damping. The observations reconfirmed the results of Goodman, that the maximum dissipation occurs at some optimum pressure, which is in between the high and low clamping pressure.

Ottl et.al (1979) performed experiments on Butt-strap joint of connecting Aluminium plates using a bolt connection. Two sets of experiments were performed to excite the Butt-strap joints. The first investigation was with a quasi-static periodic longitudinal loading and the other investigation was done with a torsional loading. Both experiments showed no-dependence of loading frequency on the hysteresis curve. However, the latter case showed an exponential increase in hysteresis area with increase in loading amplitude. Coulomb model was used as the analytical model for the correlation with experimental results. Based on the observations of Ottl et.al work, authors like Griffen (1986) developed continuous model as the cumulation of various discrete Iwan elements. Later, Kolsch (1993) extended the Ottl et.al observation with use of a new and more generalized discrete modelling approach based on Bouc-Wen model and described hysteresis shapes generated due to the joint damping.

As the initial research on the joint damping showed the importance of achieving the optimum pressure, GOULD AND MIKIC (1972) performed experiments to study the profile and magnitudes of the pressure distribution over the contact interface for bolted joints. The computational and experimental results were matched, wherein the bolts were modelled in numerical description with an equivalent distributed surface load under on the bolt head interface. ZIADA AND ABD (1980) extended the former model with more realistic external loading including the bolt geometrical model too. ZIADA AND ABD (1980) showed that there is a influence of the bolt diameter on the pressure distribution and hence the geometrical model of the bolts should always be considered. The important observations from GOULD AND MIKIC (1972) and ZIADA AND ABD (1980) study is that the pressure distribution over the contact interface due to the bolted joints has a parabolic behaviour and the profile of the pressure distribution is independent of the bolting torque. Also, the circular contact zone is approximately 3.5 times the diameter of bolt used for connecting two plates. Other authors like KENDALL AND TABOR (1971) performed experiments to measure the contact pressure based on the ultrasonic reflection methods. NANDA AND BEHERA (1998) have studied the dynamic slip behaviour in accordance to the observations of the ZIADA AND ABD work. NANDA AND BEHERA (1998) empirically established that to obtain an uniform pressure distribution, the bolts have to be separated by an approximate distance of twice the diameter of connecting bolt.

The most cited work in recent past for characterization of the dynamics of structure with bolted joints is attributed to GAUL and his successors. GAUL (1981) performed experimental investigations to study the isolated joint behaviour to accommodate the local non-linear behaviour in a global assembled structure. The experiment results were also the input to the numerical contact model based on the Coulomb friction law. Later GAUL (1983) extended the experimental investigation to the lap joints. The most important contribution is the experimental set-up of torsional and longitudinal resonators to excite the torsional and longitudinal modes of a lap joint respectively. GAUL AND BOHLEN (1984) explained the concepts of the reflection, transmission and dissipation of the mechanical waves at the contact interfaces with use of both experimental and numerical models. GAUL AND BOHLEN used a lumped joint model to characterize the contact interfaces with parameters available from the experimental results and applied it in the grid frame structure used in spacecraft industry. GAUL ET.AL (1994) discussed the leaf-shape of the hysteresis for joints, which were different from the parallelogram hysteresis shape obtained from conventional Coulomb model. The lap joint model was modelled with a continuous varying pressure distribution, while the predecessors modelled the contact interface with uniform pressure distribution. With use of distributed joint model and Coulomb constitutive formulation, the leaf shape hysteresis was obtained. GAUL AND LENZ (1997) described the longitudinal and torsional resonator and made a qualitative study on the influence of the bolting torque and excitation amplitude on the hysteresis shapes and area of dissipation. A continuous-lumped joint model was used based on the Valanis model to capture the hysteresis with better accuracy than the model based on the Coulomb model. GAUL AND NITSCHE (2000) developed the concept of active or semi-active joints. The idea was to control the contact pressure in joints such that the damping of the global structure can be modulated according to the requirement.

Numerical Implementation. With advent of the numerical techniques, approximate solution for a complex model is possible to a good degree of accuracy. The same holds true for the numerical modelling of the contact interfaces. Essentially the use of finite element method enhanced the application and provided more opportunities to model the contact behaviour in the continuum bodies. The foundation of the finite element modelling is attributed to the work of ARGYRIS, CLOUGH and ZIENKIEWICZ. Finite elements used for the contact formulation were referred as the interface elements based on the work of ZIENKIEWICZ. GOODMANN, TAYLOR AND BREKKE (1968) presented the modelling approach of jointed rock using a zero thickness element formulation. PANDE AND SHARMA (1979) discussed the implementation of the interface elements in details and their numerical ill-conditioning. Later, DESAI AND ZAMAN (1984) and SHARMA AND DESAI (1992) presented the improved interface thin layer and its implementation in finite elements for modelling of jointed rocks. The other industrial applications of jointed interface like spot welds, bolted joints, rivet joints etc. were too implemented using finite elements by authors like WILLNER, LAURSEN AND SIMO, AHMADIN ET.AL and many others.

The other advancements in the numerical modelling of the contact mechanics is attributed to the algorithms of contact formulations. The contact problem based on the variational principle was reduced to an optimization problem, to be solved for minimization of the residuum. The algorithms were developed by authors like SIMO, WRIGGERS AND TAYLOR (1985), KIKUCHI AND ODEN (1988), SIMO AND LAURSEN (1992) and later followed by many extensions. The commercial software use these algorithms like penalty, Lagrange and augmented Lagrange methods for solving the contact problems.

The dynamic or vibrational problems involving contact interface are conventionally solved in time domain based on the implicit numerical methods. Explicit numerical methods are often used for simulating drop and crash problems, as they are computationally time efficient in comparison to implicit codes. However, the explicit numerical solving techniques are restricted with stability issues. Broadly, the frictional contact problems are solved in time domain, like the work of MAYER (2007) presented the formulation for the micro-slip modelling for the bolted joints.

Alternatively with the advent of the fast fourier transformation, the vibrational behaviour of the assembled structure under periodic excitation is also made possible in frequency domain. The alternative approach to cumbersome time domain calculations is the Harmonic Balance Method (HBM). HBM was first proposed by URABE (1966) with investigations on the convergence condition and its numerical applications, and proved to be efficient as the method presents a direct implementation in frequency domain. LAU (1981) extended the approach to incremental HBM which provides better convergence and stability. HBM and its derivatives became popular for the use of the applications involving the non-linear vibration, in specific for the structures excited with a periodic loading. PIERRE (1985) extended the HBM method with use of multi harmonics to describe the non-linear behaviour with respect to sub and higher harmonics too. LING (1987) further developed a method with use of fast Fourier transform to improve the computational time. CARDONA ET.AL presented the HBM solution and its other derivative methods in conjecture with continuation method to describe the unstable regions through arc length control techniques. However, today the use of HBM in conventional form is not often used, but in a hybrid form i.e Alternate Frequency Time (AFT) domain method. Many authors CARDONA, LIU, WILLNER ET.AL etc have worked further on the AFT domain representations.

1.3 Aim and Work Outline

The broad aim of this thesis is to develop and implement a contact model to capture the non-linear effects from the contact interfaces on the dynamical behaviour of assembled structures. The two challenges that exist for the numerical techniques to model non-linear effects are model size and field conditions. The conventional methods either suffers from numerical convergence issues or from computational cost when used for the complex large structure under broad band dynamic excitations like random excitation. This defines the specific goal of the thesis to propose a contact model which is capable of not only handling the large structures in terms of computational cost but also capable of predicting the vibrational behaviour of structure under the random excitations. To achieve this in systematic approach, the aim of thesis is divided into two phases of - model development and model implementation.

The model development phase concentrates on developing an equivalent quasi-linearised method. The equivalent definition ensures the models capability to capture the non-linear effects from the contacts on the dynamic behaviour. The quasi-linearised definition ensures that the advantages of the linear system are retained. In specific, advantages of having a linear basis are that the broad band excitation can be numerically solved based on the modal superposition analysis and the large models can be solved with less computational cost. The model implementation phase concentrates on the implementation of the model in terms of the conventional commercial software (like Ansys) based on finite element methods. The other part is the interpretation of the parameters used in model to define the equivalent stiffness and damping, to be used in the vibration equation. Further, the opportunities of extensions to the present model should be viable. In specific, this thesis concentrates on the pre-stress modal superposition harmonic and random PSD analysis, with modelling the contact interfaces based on the proposed model defined as Damped-Pressure Dependent Joint (D-PDJ) model.

The thesis is divided into six main chapters. Chapter 1 discussed the motivation of this thesis and relevant literature study on contact modelling.

Chapter 2 describes the conventional contact mechanics foundation and the constitutive equations governing the contact behaviour under quasi-static and dynamic loadings. The generalized results of the conventional constitutive laws form the basis to develop the new contact model.

Chapter 3 shows the different analytical and numerical techniques of solving the dynamic problems involving non-linearity. This chapter describes the two conventional techniques of solving dynamic problems- in the time and frequency domain. Few examples discussing the implementation of the non-linear constitutive laws are presented. Apart from the understanding of the solving process, the chapter discusses in detail the disadvantages of the conventional solving techniques of non-linear problems, based on the results of used examples. The chapter also gives a brief introduction on the experimental methods for data acquisition and analysis of the vibration measurements.

Chapter 4 describes the derivation and development of the new proposed contact model. The model is defined in terms of the equivalent dynamic terms of contact stiffness and the damping from the contacts. A detail discussion on the use of different parameters to develop the formulations for the proposed D-PDJ model is presented.

Chapter 5 presents a parametric study on the test structure to investigate the influence on the dynamic properties under set of external operational factors like bonding pressure, excitation force and the contact pairing materials. The influence of the external factors on dynamic behaviour is studied by quantifying the influence on the resonance frequencies and the damping of the global systems. For each case, the optimal choice of parameters used in the proposed new contact model is presented and conclusions are made to judge the capability of proposed D-PDJ model.

Chapter 6 shows the implementation of the proposed D-PDJ model on two prototype structures resembling the ECU structures. The chapter investigates the applicability of the proposed model in terms of accuracy in predicting the dynamical behaviour for large models. Also, a qualitative comparison between the conventional commercial software techniques is done to quantify the improvements not only in the accuracy but also in the computational time.

Chapter 2

Fundamentals of Contact Physics

Contact physics relates to the field dealing with estimation of the contact stresses, forces of adhesion, friction phenomena of slip and slide behaviour, wear of material, conductance and resistance, chemical bonding etc. It has been always a challenge to characterize the contact mechanics phenomenon through some constitutive-governing laws and the implementation of those laws in the field of classical mechanics. Among many influencing parameters governing the contact physics description, the most important parameters for the field of mechanics are materials in contact, surface roughness and external loading. This chapter discusses some of the most important governing laws of classical contact mechanics for quasi-static and dynamic loadings. The emphasis will be to obtain the relations between the contact forces and the relative displacement. This lays the foundation in deriving the equivalent contact stiffness and damping of the new proposed contact model in this thesis.

2.1 Quasi-static contact models

Bodies in contact are governed through the relation between the loading and displacements, wherein the deformation at contact interfaces are dependent on the contact pressure, surface roughness and material properties. A quasi-static loading problem constitutes to cases wherein the description of the contact are independent of the transient effects. General tribology phenomenons like friction, lubrication, wear, tear etc., require a contact between two bodies, which is always initiated by a normal contact. The normal contact problem associate to the initiation of the contact and the tangential contact problem associate to the change in the contact status. This section shows the constitutive governing equations for both the normal and tangential contact problems.

2.1.1 Normal Contact Law

The contact between any two bodies is initiated with a normal contact problem, wherein the two bodies experience normal displacement with forces perpendicular to their surfaces. The normal contact problems have been studied in detail by authors like, Hertz (1881) model being one of the first models for describing elastic contacts, extension of Hertz model for the plastic deformations was studied by Chang et.al (CEB model) [20–22], Kogut and Etison (KE model) [57] and many others. The influence of the surface roughness in the contact modelling was presented by Greenwood and Williamson et.al [42, 43, 45]. This section describes the formulations of the constitutive laws for normal contacts for elastic and plastic deformation. Later described are the formulations for the influence of the surface roughness.

2.1.1.1 Hertz model- Elastic deformation

One of the primitive analytical solution for the normal contact behaviour was proposed by Hertz (1881). The contact between two isotropic spheres or between a sphere and isotropic elastic half space is used to formulate the relations between the normal force and normal displacement. The Hertzian contact assumes a frictionless contact condition, which is justified for bodies under normal loading. For a continuous Herztian pressure distribution ($p(r)$) over the contact interface, the normal displacement (u_z) can be calculated by integrating the normal stress (here pressure) over the contact interface area [53, 89] as,

$$u_z = \frac{(1-\nu^2)}{\pi E}\int\int p(r)\frac{dxdy}{r} = \frac{\pi p_0 r_C}{2E'} - \frac{\pi p_0 r^2}{4 r_C E'}, \tag{2.1}$$

where, the Hertzian pressure distribution is $p(r) = p_0\left(1 - r^2/r_C^2\right)^{1/2}$ for $0 \leq r \leq r_C$ and the equivalent elastic constant is $E' = E/(1-\nu^2)$.

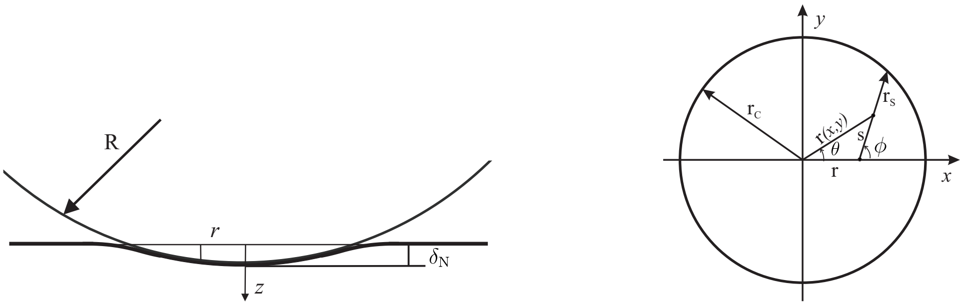

(a) Contact between a rigid sphere and elastic half space acted upon by Hertzian pressure distribution.

(b) Circular contact zone with radius r_C.

Figure 2.1: Deformation of an half elastic space under a rigid sphere leading to circular contact zone [89].

The normal displacement can also be calculated with respect to normal penetration (δ_{N}) and radius of rigid sphere (R) as [89] (see figure 2.1),

$$u_z = \delta_{\mathrm{N}} - \frac{r^2}{R}, \qquad \text{for } r <<< R. \tag{2.2}$$

From equations (2.1) and (2.2), the normal penetration (δ_{N}) and contact radius (r_{C}) can be obtained as,

$$\delta_{\mathrm{N}} = \frac{\pi p_0 r_{\mathrm{C}}}{2E'} \qquad \text{and} \qquad r_{\mathrm{C}} = \frac{\pi p_0 R}{2E'}. \tag{2.3}$$

The normal contact force (F_{N}) can be calculated as the integration of Hertzian pressure distribution over the contact area and is obtained as,

$$F_{\mathrm{N}} = \int_0^{r_{\mathrm{C}}} p_0 \left(1 - \frac{r^2}{r_{\mathrm{C}}^2}\right)^{1/2} 2\pi r dr = \frac{2}{3} p_0 \pi r_{\mathrm{C}}^2. \tag{2.4}$$

From equations (2.3) and (2.4), the normal force is rewritten in terms of penetration as,

$$F_{\mathrm{N}} = \frac{4}{3} E' R^{1/2} \delta_{\mathrm{N}}^{3/2}. \tag{2.5}$$

The above equation shows a non-linear dependence of the normal force with respect to the penetration, where the elastic constant (E') and radius of the sphere (R) are constant parameters. This formulation is derived for the case of an elastic half space deformation under influence of a rigid sphere indenter. The formulation for the case of two elastic spheres in contact requires the substitution of the elastic modulus and radius of sphere with composite elastic modulus (E^*) and composite radius (R^*) respectively. The equivalent elastic constant is calculated as the superposition of elastic constants of two materials in contact. The normal force for two elastic spheres in contact can thus be calculated as,

$$F_{\mathrm{N}} = \frac{4}{3} E^* R^{*1/2} \delta_{\mathrm{N}}^{3/2}, \tag{2.6}$$

where, $1/E^* = \Big((1-\nu_1^2)/E_1\Big) + \Big((1-\nu_2^2)/E_2\Big)$ and $1/R^* = \big(1/R_1\big) + \big(1/R_2\big)$.

The normal contact stiffness is calculated as the derivative of the normal force with respect to the normal relative displacement. Equation (2.6) is used to determine the normal contact stiffness for two elastic spheres in contact as,

$$k_{\mathrm{N}} = \frac{dF_{\mathrm{N}}}{d\delta_{\mathrm{N}}} = 2E^* R^{1/2} {\delta_{\mathrm{N}}}^{1/2}, \qquad r_{\mathrm{C}} = \sqrt{\delta_{\mathrm{N}} R^*}. \tag{2.7}$$

The normal contact stiffness shows a non-linear dependence on the normal relative displacement. This definition of normal contact stiffness forms the basic foundation for solving the normal contact problems under static loads. However, this definition of normal contact stiffness is valid for hertzian pressure having elastic deformations. The formulations for plastic deformations are presented in the following section.

2.1.1.2 Hertz model- Plastic deformation

For large magnitudes of external loading, the contact interface will deform plastically. The Hertz elastic model cannot be used for such cases. The extension of elastic Hertzian model to elastic-plastic deformation has been presented by CEB model [21] and other models. The elastic-plastic deformation phenomenon is governed through a yield point limit on the normal penetration, referred as critical interference. For deformations below the critical interference, the behaviour is elastic and for the deformations above the critical interference, the behaviour is plastic. The formulation to define the relation between the normal forces and deformations based on CEB model [21] are presented as [34],

$$F_{\mathrm{N}} = \begin{cases} \frac{4}{3}E^{*}R^{1/2}{\delta_{\mathrm{N}}}^{3/2} & \delta_{\mathrm{N}} \leq \delta_{\mathrm{NC}}, \\ \pi\kappa HR\big(2\delta_{\mathrm{N}}-\delta_{\mathrm{NC}}\big) & \delta_{\mathrm{NC}} < \delta_{\mathrm{N}}, \end{cases} \tag{2.8}$$

wherein, H is the Hardness of the material and $\kappa = 0.454 + 0.41\,\nu$ is the hardness factor. The critical interference (δ_{NC}) is dependent on the hardness, elastic constant and radius of indenter and is expressed as,

$$\delta_{\mathrm{NC}} = \left(\frac{\pi\kappa H}{2E^{*}}\right)^{2} R. \tag{2.9}$$

The relation between normal force and relative displacement from CEB model for the elastic deformation is same as the Hertz model. For the plastic deformation, the relationship between the normal force and relative displacement is linear. Hence, the transition from elastic to plastic deformation at critical interference is the transition in force-displacement relation from non-linear to linear behaviour. The normal contact stiffness is calculated as the derivative of the normal force with respect to the penetration. The contact stiffness associated with elastic-plastic CEB model is calculated distinctly in regions of elastic and plastic deformation, as shown in the below equation,

$$k_{\mathrm{N}} = \begin{cases} 2E^{*}R^{1/2}{\delta_{\mathrm{N}}}^{1/2} & \delta_{\mathrm{N}} \leq \delta_{\mathrm{NC}}. \\ 2\pi\kappa HR & \delta_{\mathrm{NC}} < \delta_{\mathrm{N}}. \end{cases} \tag{2.10}$$

From above equation, it can be seen that the normal contact stiffness is independent of the relative normal displacement and is only dependent on the constant parameters like the hardness of material, hardness factor and radius of sphere. Based on the formulations presented for two spheres in contact, the macroscopic modelling of the surfaces in contact can be visualized as the contact of finite number of such spheres. Each contact pair with their respective stiffness is then characterized as a point to point contact. However, the contact stiffness depends on the geometry of spheres i.e. radius of sphere, which can be assumed as a constant value and can be calculated as the mean on the surface roughness. This is a very simplified case and does not include the effects of surface roughness on the constitutive relations of force-displacement relation. The next section shows the constitutive relation including the influence of the surface roughness and its application in determining contact stiffness.

Influence of surface roughness

All engineering surfaces posses surface roughness, which should be considered while modelling contacts. Theoretical and empirical models to accommodate the influence of roughness have been studied in detail by authors like Archard et.al [7, 79, 119], Greenwood and Williamson [43], Bower and Johnson [14] and many others. The inclusion of surface roughness in contact mechanics was motivated due to the shortcoming of the Hertzian theory. Although Hertzian theory proposed an analytical solution of a single asperity contact, but the relationship between loading and penetration require the prior knowledge about the contact geometry and contact area [43]. There exists two concepts of contact area- apparent and actual contact area. The apparent contact area is defined as the macroscopic area, which is calculated based geometrical boundaries of the contact surface. The actual contact area is defined as the summation of the individual contact area occurring at various asperities. Due to inclusion of the surfaces roughness in contact modelling, the actual contact area can be calculated and therefore the estimation of the local contact stress are more realistic.

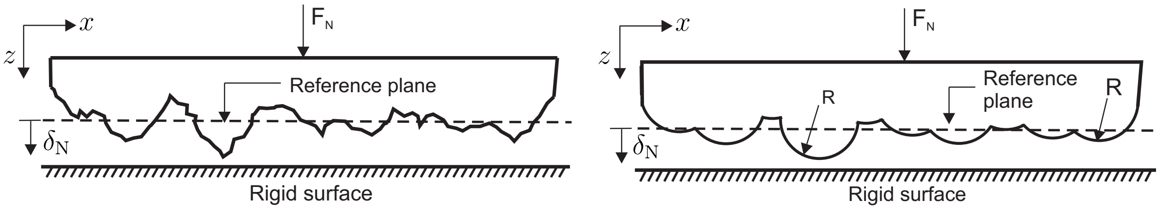

(a) A rough surface in contact with a rigid surface. (b) Asperity peaks represented using spheres.

Figure 2.2: Modelling of surface roughness peaks as spherical asperities of same radius based on Greenwood and Williamson model.

Greenwood and Williamson [43] approximated the surface roughness with a Gaussian normal distribution. An assumption of all asperities possessing a spherical geometry with same radius of curvature is taken, see figure 2.2. Figure 2.3 shows an approximation of surface roughness with normal distribution. The probability of initiation of contact will be at the peaks of the surface roughness. This allows the choice of distribution to be taken as exponential, where the predominant effects of peak-asperities can be captured. However the main advantage of using exponential distribution is the availability of analytical closed form solutions, which is not possible for Gaussian distribution.

Greenwood and Williamson (1977) [44] later showed that an exponential distribution is a simplified choice for roughness distribution and does not comply with Gaussian distribution, as evident from figure 2.3(b). A modified exponential distribution [44, 88] was proposed to have better correlation to the Gaussian distribution for the predominance at the peaks, see figure 2.3(b).

The probability distribution for modified exponential distribution fit is,

$$\phi_{\mathrm{mexp}}(z) = c\exp\left(-\lambda_c \frac{z}{\sigma_r}\right), \tag{2.11}$$

wherein, c and λ_c represent the dimensionless constant coefficients and σ_r is the standard deviation of the surface roughness. For all practical purposes, the values of $c = 17$ and $\lambda_c = 3$ are feasible [88].

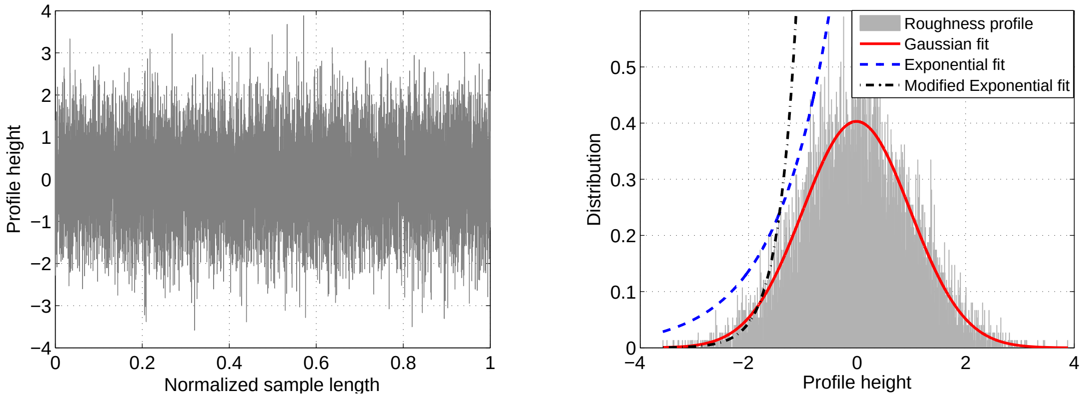

(a) Random surface roughness. (b) Distribution fits for peaks.

Figure 2.3: Use of different distribution function to capture the surface roughness based on the GREENWOOD AND WILLIAMSON model.

A simplified assumption of same asperity radius R_{A} for all peaks is taken. The individual contact pair's contact area and normal force at various profile height are formulated based on the results of the Hertzian contact as,

$$A(z) = \pi R_{\mathrm{A}}(z-\delta_{\mathrm{N}}), \tag{2.12}$$

$$F_{\mathrm{N}}(z) = \frac{4}{3}E^* R_{\mathrm{A}}^{1/2}\left(z-\delta_{\mathrm{N}}\right)^{3/2}. \tag{2.13}$$

The total area and force with use of modified exponential distribution are calculated as the summation of local contact area and force respectively and are obtained as,

$$\begin{aligned} A &= \frac{cn\pi R_{\mathrm{A}}\sigma_r}{\lambda_c^2}\exp\left(-\lambda_c\frac{\delta_{\mathrm{N}}}{\sigma_r}\right), \\ F_{\mathrm{N}} &= \frac{c\pi^{1/2} n E^* R_{\mathrm{A}}^{1/2}\sigma_r^{3/2}}{\lambda_c^{5/2}}\exp\left(-\lambda_c\frac{\delta_{\mathrm{N}}}{\sigma_r}\right). \end{aligned} \tag{2.14}$$

Equation (2.14) represents the constitutive relation for normal contact law including the surface roughness parameters. The normal contact stiffness is then calculated as the derivative of the force with respect to the displacement and is obtained as,

$$k_{\mathrm{N}} = \frac{dF_{\mathrm{N}}}{d\delta_{\mathrm{N}}} = \frac{\lambda_c}{\sigma_r}F_{\mathrm{N}}. \tag{2.15}$$

The stiffness formulation forms the basis of tribology motivated constitutive law, used for defining the normal contact law in this thesis, as discussed in chapter 4. Similar to the extension of Hertz model for plastic deformation, CHANG ET.AL (CEB model) formulated the elastic-plastic deformations for Greenwood and Williamson model too. The critical interface limit defining the transition from elastic to plastic deformation in other models is defined as plasticity index. In WHITEHOUSE AND ARCHARD model, the elastic deformation is defined for the plasticity index values less than 0.6 and plastic deformation is defined for the plasticity index value more than 1. The behaviour in between values of 0.6 and 1 is unknown. BOWER AND JOHNSON [14] model defines the magnitude of wear with respect to the plasticity index. This thesis does not deal with the large plastic deformation and wear related topics for the contact interface. Hence, the simplified GREENWOOD AND WILLIAMSON model with assumption of modified exponential distributions is sufficient for proposing the governing laws for the contact mechanics, required to model the structural dynamic systems, as covered in chapter 4.

2.1.2 Tangential Contact Law

For tangential loading, the contact model requires the modelling of the frictional behaviour with the estimation of the tangential stresses. Similar to the case of Hertzian theory of same materials in contact, the relative displacement is same on both mating surfaces for tangential loading too. Hence, the contact area dimensions depend only on the applied normal force and geometry of profiles in contact. For different materials in contact, the tangential force couples with the normal pressure. This section presents the relation between the tangential forces and relative displacements for different states of contact based on the amplitudes of loading.

2.1.2.1 Sliding Contact

Large tangential loading for two spherical bodies in contact leads to a large relative displacement. Due to this the bonding between the two bodies is broken. This contact state of complete slip between the bodies is called as sliding contact. The primitive constitutive law for modelling sliding behaviour is based on AMONTONS (1699) law, to define a constant tangential stress in sliding as,

$$\frac{|\tau|}{p} = \mu, \tag{2.16}$$

where, μ is the coefficient of friction and p is the normal pressure. The same equation is extended to tangential force (F_{T}) in the sliding state as the product of the coefficient of friction (μ) and normal force (F_{N}). For tangential forces (F_{T}) less than the magnitude of limiting force friction (μF_{N}) value, there will be no sliding. The state which occurs before the sliding is referred to as a stick state. The pictorial description of the two states of contact under tangential loading is shown in figure 2.4.

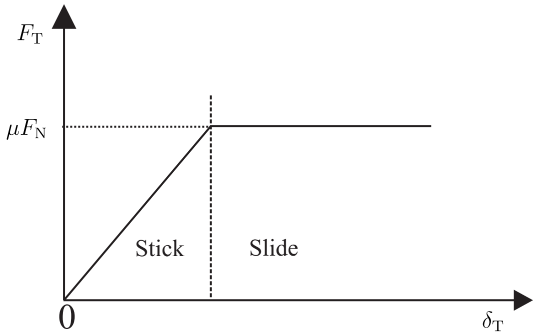

Figure 2.4: Stick and sliding region for the tangential loading with transition from stick to slide region for load exceeding the limit of friction force (μF_N).

With use of Hertzian pressure distribution ($p(r)$), the tangential stress ($\tau(r)$) in full sliding motion can be defined in terms of the contact geometry and normal load as,

$$|\tau(r)| = \mu p_0 \left(1 - \frac{r^2}{r_C^2}\right)^{1/2} = \frac{3\mu F_N}{2\pi r_C^2}\left(1 - \frac{r^2}{r_C^2}\right)^{1/2}. \tag{2.17}$$

From the above equation, it is can be seen that at the condition of complete sliding, the tangential stress depends on the normal force (F_N), contact radius (r_C) and coefficient of friction (μ). The next section explains the formulation of the tangential forces for stick region and the transition from stick to slide region.

2.1.2.2 Stick Contact

The state of contact as fully adhered or stick suggests no relative motion between the bodies in contact. However, due to the tangential loading there should be some amount of traction force existing. The relationship between the tangential displacement and forces can be established in a similar approach as used in hertzian contact model based on theory of elasticity. For an in-plane unidirectional tangential load at origin, a uniform stress distribution is obtained. The tangential displacement of elastic half space can be calculated for a uniform tangential stress distribution at the interface in a similar way as presented in equation (2.1) as,

$$u_x = \frac{1}{4\pi G}\int\int \tau(r)\frac{dxdy}{r} = \frac{(2-\nu)\pi\tau_0 r_C}{4G}, \tag{2.18}$$

where, the uniform tangential stress distribution is $\tau(r) = \tau_0\left(1 - r^2/r_C^2\right)^{-1/2}$. The relative tangential displacement between the two spheres in contact is calculated as,

$$\delta_T = u_{x,\text{top}} - u_{x,\text{bottom}} = \frac{\pi\tau_0 r_C}{G^*}. \tag{2.19}$$

The equivalent shear modulus (G^*) used in equation (2.19) is calculated as,

$$\frac{1}{G^*} = \frac{(2-\nu_1)}{G_1} + \frac{(2-\nu_2)}{G_2}. \tag{2.20}$$

The tangential force acting over the contact interface due to an uniform stress distribution is calculated by integrating the stress distribution over the interface area. Using the equation (2.19) of relative tangential displacement, the tangential force is re-formulated with respect to the relative tangential displacement.

$$F_\mathrm{T} \;=\; \int\limits_0^{r_\mathrm{C}} \tau(r) 2\pi r dr \;=\; 2\pi\tau_0 r_\mathrm{C}^2 = \; 8G^* r_\mathrm{C}\delta_\mathrm{T}. \tag{2.21}$$

From equation (2.21), it is observed that the tangential force is linearly dependent on the relative displacement, with an assumption of no variation in contact radius and equivalent shear modulus with respect to the loading. This is depicted in figure 2.4. The tangential stiffness of the stick state can be calculated by differentiating the tangential force with respect to the tangential relative displacement.

$$k_\mathrm{T0} = \frac{dF_\mathrm{T}}{d\delta_\mathrm{T}} = 8G^* r_\mathrm{C}. \tag{2.22}$$

The tangential contact stiffness for stick state is a constant value and is dependent on the shear modulus constant and contact radius. As the contact area and the material elastic constant are same for both normal and tangential loading, the contact radius can be estimated in-terms of the normal stiffness from equation (2.7). The relation between the normal and tangential contact stiffness for the combination of normal load and tangential load in stick state is calculated as,

$$k_\mathrm{T0} = \frac{4G^* k_\mathrm{N}}{E^*}. \tag{2.23}$$

It can be seen that the tangential linear stiffness for stick state can be estimated from the normal stiffness and equivalent composite elastic constants only, eliminating the direct dependence on contact geometry. For same isotropic elastic materials in contact, it further reduces to function of the Poisson's ratio only.

2.1.2.3 Mindlin model- Partial Slip

The preceding section described the stick state constitutive relations based on the uniform stress distribution at the contact interface. However, the choice of uniform stress distribution yields non-physical solution at the boundary of the contact zone, i.e $\tau(r = r_\mathrm{c}) = \infty$, while the Hertzian pressure is zero $p(r = r_\mathrm{c}) = 0$. This implies that for any magnitude of tangential loading, there cannot be complete stick state existing throughout the contact

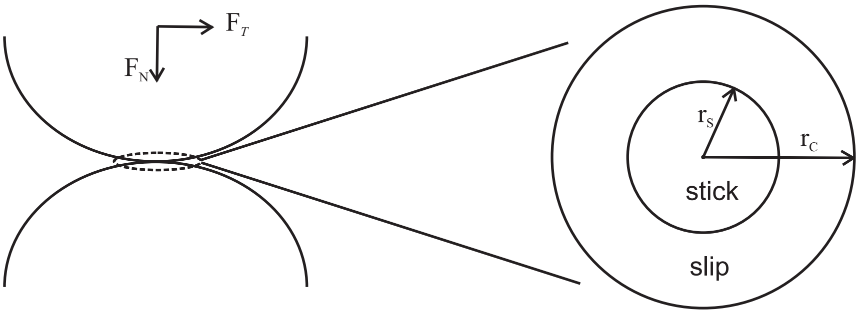

Figure 2.5: The region of stick and slip at the interface of two spheres in contact under normal loading.

interface. Hence, there should be a transition from stick state to slide at some radius say r_s, such that there is a continuity of stress distribution. The existence of both stick and slide regions in contact interface is referred as to the partial slip state. Figure 2.5, shows a pictorial representation of division of contact zone into stick and slip state with their respective radii. CATTENO (1938) and MINDLIN (1949) [71] were the first ones to propose the analytical solution for tangential contact problems with description of the partial slip formulations. For state of sliding, the stress distribution is calculated based on equation (2.17). The superposition of two Hertzian tangential stress distribution is idealized to fulfil the contact conditions at the boundary of the transition from stick to slip state [53, 89].

$$\tau = \begin{cases} \tau^{(1)} + \tau^{(2)} & 0 \le r \le r_{\mathrm{S}}. \\ \tau^{(1)} & r_{\mathrm{S}} \le r \le r_{\mathrm{C}}. \end{cases} \tag{2.24}$$

where in, $\tau^{(1)} = \mu p_0 \left(1 - r^2/r_{\mathrm{C}}^2\right)^{1/2}$ and $\tau^{(2)} = -\mu p_0 \left(r_{\mathrm{S}}/r_{\mathrm{C}}\right)\left(1 - r^2/r_{\mathrm{S}}^2\right)^{1/2}$.

The displacement and relative displacement of elastic spheres in contact with combined stress distribution can then be obtained in a similar way of integrating stress distribution over contact area [53] and are obtained as,

$$u_x = u_x^{(1)} + u_x^{(2)} = \frac{\pi \mu p_0 (2-\nu)}{8 G r_{\mathrm{C}}} (r_{\mathrm{C}}^2 - r_{\mathrm{S}}^2), \tag{2.25}$$

$$\delta_x = \frac{\pi \mu p_0}{8 G^* r_{\mathrm{C}}} (r_{\mathrm{C}}^2 - r_{\mathrm{S}}^2). \tag{2.26}$$

The tangential force can be calculated by integrating the tangential stress distribution over the contact interface area. As two states of stick and slip exists, the addition of the individual force in each state gives the total tangential force for partial slip state as,

$$F_{\mathrm{T}} = \int_0^{r_{\mathrm{C}}} \tau^{(1)} 2\pi r dr + \int_0^{r_{\mathrm{S}}} \tau^{(2)} 2\pi r dr = \mu F_{\mathrm{N}} \left(1 - \frac{r_{\mathrm{S}}^3}{r_{\mathrm{C}}^3}\right). \tag{2.27}$$

From equation (2.27), the contact radius of stick state in the complete contact zone can be calculated in terms of the tangential force and limit friction force as,

$$r_{\mathrm{S}} = r_{\mathrm{C}} \left(1 - \frac{F_{\mathrm{T}}}{\mu F_{\mathrm{N}}} \right)^{1/3}. \tag{2.28}$$

The above expression can be substituted in the formulation of relative displacement in equation (2.26) and the result of Mindlin model for partial slip is obtained as,

$$\delta_{\mathrm{T}} = \frac{3\mu F_{\mathrm{N}}}{16G^{*} r_{\mathrm{C}}} \left(1 - \frac{r_{\mathrm{S}}^{2}}{r_{\mathrm{C}}^{2}} \right) = \frac{3\mu F_{\mathrm{N}}}{16G^{*} r_{\mathrm{C}}} \left(1 - \left(1 - \frac{F_{\mathrm{T}}}{\mu F_{\mathrm{N}}} \right)^{(2/3)} \right). \tag{2.29}$$

The above expression is symmetric and hence the tangential force can be equated in terms of relative displacement as,

$$F_{\mathrm{T}} = \mu F_{\mathrm{N}} \left(1 - \left(1 - \frac{\delta_{\mathrm{T}}}{\delta_{\mathrm{Tmax}}} \right)^{3/2} \right), \tag{2.30}$$

wherein, $\delta_{\mathrm{Tmax}} = \left(3\mu F_{\mathrm{N}} / 16G^{*} r_{\mathrm{C}} \right)$ refers to the maximum relative displacement at which sliding is initiated.

The contact stiffness in partial slip can be estimated by differentiating the tangential force with respect to tangential relative displacement and is expressed as following,

$$k_{\mathrm{T}} = \frac{dF_{\mathrm{T}}}{d\delta_{\mathrm{T}}} = k_{\mathrm{T0}} \left(1 - \frac{\delta_{\mathrm{T}}}{\delta_{\mathrm{Tmax}}} \right)^{1/2} = k_{\mathrm{T0}} \left(1 - \frac{F_{\mathrm{T}}}{\mu F_{\mathrm{N}}} \right)^{1/3}. \tag{2.31}$$

For F_{T} less than μF_{N}, the tangential contact stiffness (k_{T}) is equal to contact stiffness of the stick state (k_{T0}). For complete sliding state the contact stiffness is zero.

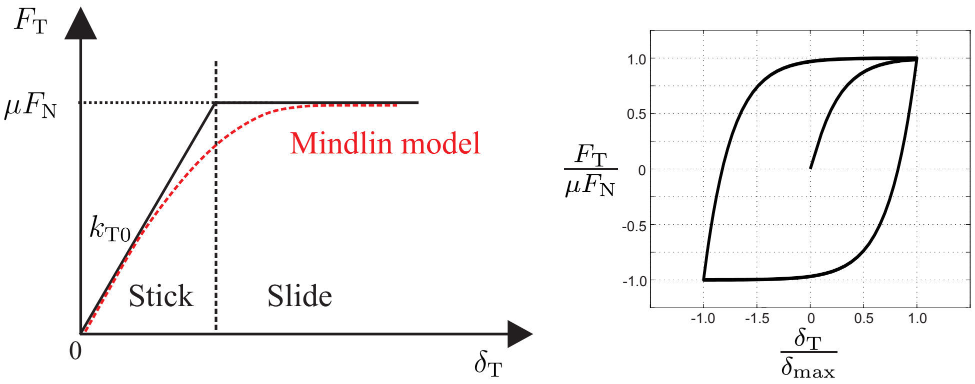

(a) Force-displacement relation.

(b) Hysteresis for harmonic load.

Figure 2.6: The Mindlin model showing a non-linear continuous relation for force-displacement curve and generation of conventional Mindlin hysteresis shape for a harmonic loading.

The contact stiffness from stick to complete sliding state varies non-linearly based on the equation (2.31), as depicted in figure 2.6(a). The relation between the tangential force and relative displacement are expressed for quasi-static loading, which extended to periodic loading leads to the formation of a hysteresis. The area under hysteresis is associated with the contact dissipation, see figure 2.6(b). The dissipation associated with periodic loading has been analytically estimated by MINDLIN (1951) [72] for a period of oscillation as,

$$\Delta W = \frac{9\mu^2 F_\mathrm{N}^2}{10G^* r_\mathrm{c}}\left(1-\left(1-\frac{F_\mathrm{m}}{\mu F_\mathrm{N}}\right)^{5/3}-\frac{5F_\mathrm{m}}{6\mu F_\mathrm{N}}\left(1+\left(1-\frac{F_\mathrm{m}}{\mu F_\mathrm{N}}\right)^{2/3}\right)\right), \tag{2.32}$$

where F_m refers to the maximum force reached in the hysteresis shape. Hence, it is concluded for tangential contact, that the constitutive relations show a non-linear behaviour with dissipative terms and is time independent.

This section has depicted the formulations for the tangential contact stiffness definition for different contact status. The dissipation observed in tangential contacts depicts the frictional losses due to tangential relative displacement between the bodies in contact. These formulations are used as building blocks in chapter 4 for the proposed new contact model definition of contact stiffness in this thesis. The next section extends the discussion of constitutive relations for the dynamic frictional contact modelling.

2.2 Dynamic contact models

Bodies in contact when excited with dynamic loads lead to the frictional losses. Assembled structures having metallic bodies in contact without lubricated surfaces constitute to the problems of dry frictional contacts. The formulations of dry contacts are independent of velocity, but dependent on the velocity reversals. The conventional dynamic contact models are COULOMB model, DAHL model, LUGRE model etc. Other dynamic models are further extension to these classical dynamic models. COULOMB (1781) model presented the dynamic fromulation of stick and slip phenomenons. DAHL model formulates the smooth transitions from stick to slip states. LUGRE model is the extension of the Dahl model for lubricated surfaces.

This section discusses the most important constitutive laws required for dynamic contact modelling. Later in the section, the modification to the conventional Dahl model is presented with an aim to capture the physical phenomenon observed in analogy to the solid mechanics. The constitutive relations for the modified model are used in chapter 4 in building the proposed contact model's damping phenomena.

2.2.1 Coulomb Friction Model

The COULOMB (1781) model is motivated from the formulations of the Amontons's law in dynamical domain with modelling stick-slide behaviour. Coulomb defined two states of friction contact- Static and kinetic friction. For bodies at rest, the resistance force of friction is referred as static friction. For bodies in motion, the resistance force of friction is referred as kinetic friction. Both representations are presented below in equations as,

$$\begin{aligned} \text{Static friction:} \quad & F_s = \mu_s F_N, \\ \text{Kinetic friction:} \quad & F_k = \mu_k F_N. \end{aligned} \tag{2.33}$$

In the above equation, μ_s and μ_k are the coefficient of static and kinetic friction respectively. The important observations are : F_s and F_k are ideally independent of the contact area or roughness but dependent on the contacting material, μ_s is greater than μ_k but with not large difference between them and the kinetic friction for dry contacts is independent of the sliding velocity.

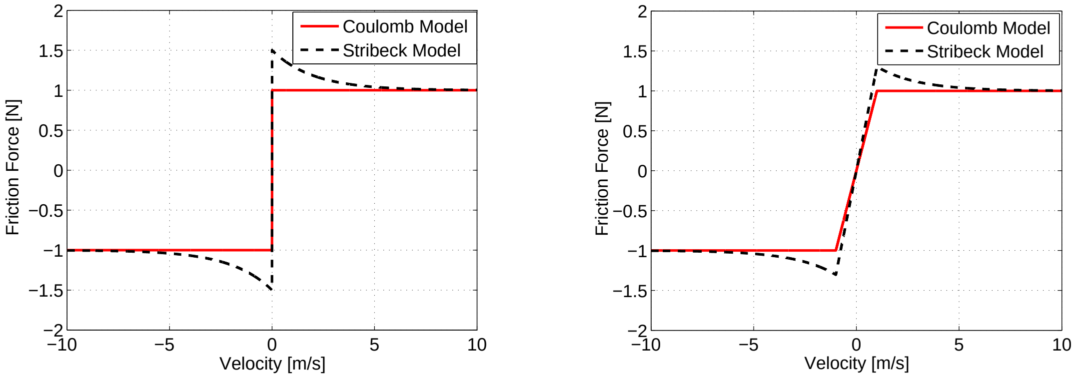

(a) Pure Sliding model.

(b) Stick-Slip model.

Figure 2.7: Coulomb describing a dry frictional contact and Stribeck model used for viscous-lubricated contact.

The Coulomb friction model in simplified form with a coulomb friction limit or the sliding friction force $F_c = \mu F_N$ is represented as [5],

$$F = \begin{cases} F_c \mathrm{sgn}(\dot{u}) & \text{for} \quad \dot{u} > 0, \\ F_{\mathrm{ext}} & \text{for} \quad \dot{u} = 0, F_{\mathrm{ext}} < F_c, \end{cases}$$

where, $\dot{u}$ is the sliding velocity. Further extension to the Coulomb model for modelling the lubricating surface with inclusion of static friction is described by Stribeck curve. The formulation of Stribeck curve is represented as [107],

$$F = \big(F_c + (F_s - F_c)\exp(-|\dot{u}|/\dot{u}_s)\big)\mathrm{sgn}(\dot{u}) + k_s \dot{u}, \tag{2.34}$$

In the previous equation, $\dot{u}_s$ is the stribeck velocity coefficient and k_s is the viscous force coefficient. Figure 2.7 show the comparison of the Coulomb model and Stribeck curve. For a periodic excitation of a system having contact interfaces, the system experiences stick-slip phases with generation of a hysteresis. Considering the coulomb model with dependence on the sign of the velocity, the model can be defined as the combination of the elastic and dissipative part. The elastic part is associated with the stick phase and the dissipative is associated with the sliding. With assumption of $u(t) = U_0 \cos(\omega t)$, the associated dissipation energy from the sliding friction can be calculated by integrating the dissipative forces over a period of oscillation.

$$\Delta E = \oint F_d du == \int_0^{\frac{2\pi}{\omega}} F_c \mathrm{sgn}(v) v dt = 4 F_c U_0. \tag{2.35}$$

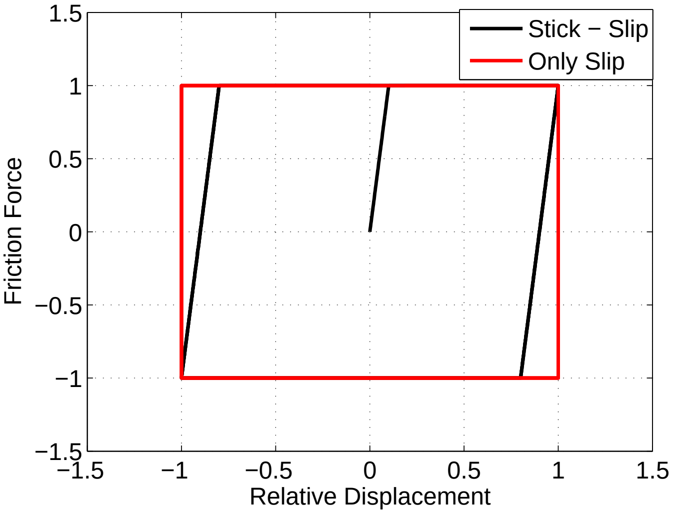

Figure 2.8: Hysteresis generated by Coulomb friction models under periodic loading.

It can be seen from equation (2.35), that the loss increases linearly with increase in the amplitude of displacement. Hence, the non-linear behaviour of the friction when modelled using Coulomb law depends only on the displacement and reversal points (or sign of velocity) for a periodic excitation. Figure 2.8 shows the dissipative hysteresis behaviour of Coulomb model for both stick-slip and only slip models. Although Coulomb model and its other derivatives have been conventional models, they do not depict the real behaviours of contacts, like modelling of micro-slip effects. The following section will address the topics of micro-slip behaviour for dynamical modelling.

2.2.2 Dahl Brush Model

DAHL (1968) [28, 29] proposed a model to include the micro-slip effect in the conventional Coulomb friction model. The motivation comes from the experimental observations conducted by Dahl on ball bearings, wherein for small amplitude of force excitations the ball bearings responded with small amplitudes of restoring forces. A contact is idealized as a mechanical bond, which is preserved until the tangential forces or shear stress acting does not exceed the breaking limit. The Dahl model can be depicted by combination of different bristle as the bonding between bodies in contact, see figure 2.9.

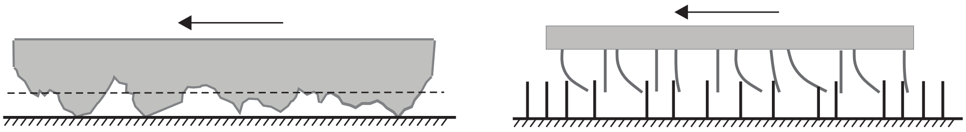
(a) A body sliding over a rigid surface. (b) Dahl brush model representation.

Figure 2.9: Representation of a rough surface using equivalent Dahl brush model for dry contacts.

The Dahl model as solid friction model finds an analogy to stress strain relationship for ductile materials. The abrupt sudden transition in the Coulomb model from stick to slip is non-physical and hence a smooth transition from stick to slip state is required to obtain a stable process. This is depicted with the basic idea of Dahl's formulation of modelling friction behaviour as an elasto-plastic model. For small amplitude of excitation, the relative motion between the interfaces is small and shows an elastic behaviour. For the loading step, the elastic deformation of the bristle occurs and for un-loading step the bristle return to the original position. This small amplitude of excitation leads to the elastic deflection of the bristle with bristle stiffness being constant. For large loadings, the bristle deflects significantly and after a certain critical value the behaviour of deflection tends to be non-linear. The bristle deflects to an amount such that upon unloading

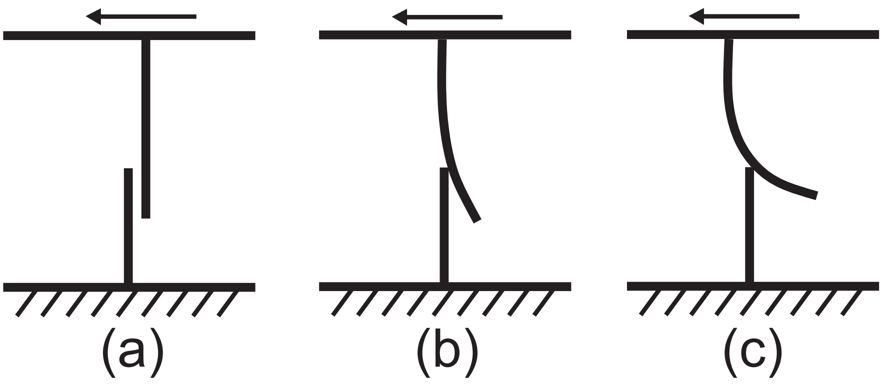

Figure 2.10: Dahl bristle friction model representation with stick phase related to an elastic bending of bristle, micro-slip as the elasto-plastic bending of bristle.

the bristle does not return to its original un-deformed position. This behaviour is associated with stress strain relation for elastic-plastic phase after the yield point. This results in the hysteresis behaviour between the applied load and deflection, similar to that of a elastic plastic material. For very large loadings, all bristle deform plastically and the brush starts sliding over the surface. This is associated with the complete sliding state of the brush similar to Coulomb model. Figure 2.10 shows an pictorial representation of the bristle deflection with increasing tangential load initiating relative motion of a body over fixed rigid surface.

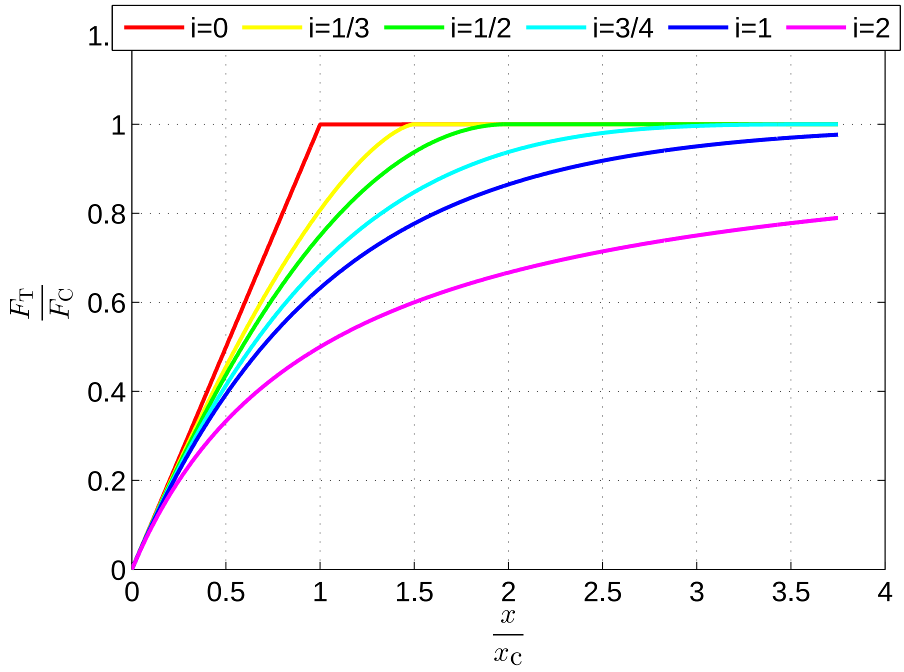

Figure 2.11: Effect of the curvature parameter in Dahl formulation for relation between the tangential force and relative displacement.

Dahl formulation in a way models the coulomb model with continuous description of stick-slip state.

$$\frac{dF_{\mathrm{T}}}{d\delta_{\mathrm{T}}} = \sigma_0 \left|1 - \mathrm{sgn}\left(\dot{\delta_{\mathrm{T}}}\right)\frac{F_{\mathrm{T}}}{F_{\mathrm{C}}}\right|^i \mathrm{sgn}\left(1 - \mathrm{sgn}\left(\dot{\delta_{\mathrm{T}}}\right)\frac{F_{\mathrm{T}}}{F_{\mathrm{C}}}\right). \tag{2.36}$$

Here, σ_0 represents the initial slope of the force- deflection curve. This can be associated to the initial tangential stiffness of the local contact spot before any tangential loading. Also, the deflection is directly associated to the relative tangential displacement between the surfaces. The formulation shown in the equation (2.36) depicts the varying contact stiffness with increasing load. As the tangential force reaches the value of limiting Coulomb friction F_{C}, the stiffness tends to zero. This related to the complete sliding between the two mating surfaces. Figure 2.11 shows the influence of the slope-curvature parameter i on the force-deflection curve. The behaviour of Dahl formulation predicts completely the Coulomb friction law for slope-curvature parameter $i = 0$. For all values of $i < 0$, it can be associated with Mindlin-Catteno model. However, the Dahl formulation for all practical purposes of the contact modelling with stick slip phenomenon is described in reduced form with unit value of slope-curvature parameters as,

$$\frac{dF_{\mathrm{T}}}{d\delta_{\mathrm{T}}} = k_{\mathrm{T0}} = k_{\mathrm{T0}} \left(1 - \mathrm{sgn}\left(\dot{\delta_{\mathrm{T}}}\right) \frac{F_{\mathrm{T}}}{F_{\mathrm{C}}} \right). \tag{2.37}$$

The above equation is a simplified formulation of variation of the bristle contact stiffness with increasing tangential loading. The stiffness at load reversal is controlled with the sign of velocity. One of the criticisms of the Dahl's formulation is that the tangential force is twice in magnitude at velocity reversals, which is not physical. This leads to the large hysteresis area in comparison to the hysteresis area without the error at velocity reversals. The Dahl's formulation of the tangential force is only dependent on the displacement and the velocity reversals, and applicable for dry contacts. The direct extension to accommodate the effect of velocity for lubricated surface for the calculation of the tangential force is accompanied by models like LuGre [32] and Leuven models [111].

2.2.3 Modified Dahl Model

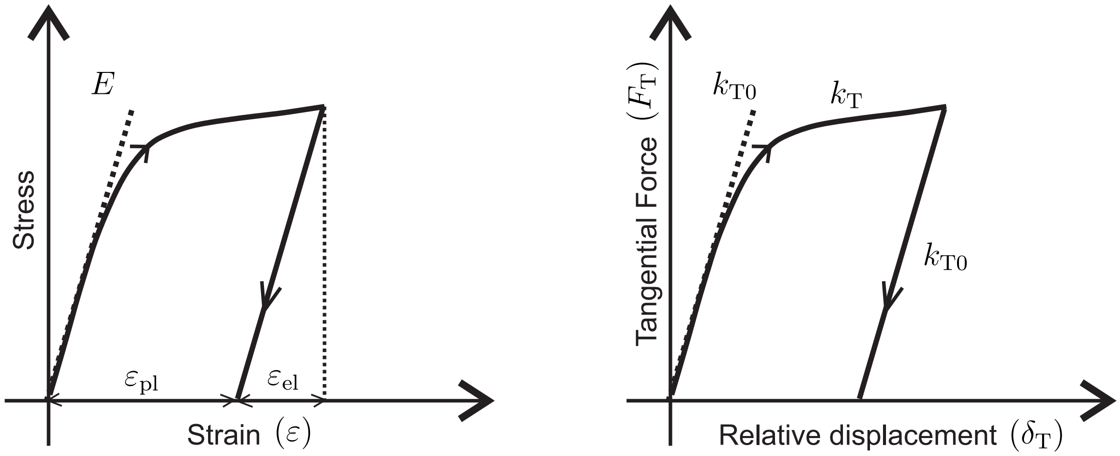

(a) Stress-strain relation. (b) Force-displacement relation.

Figure 2.12: Stress-strain relation for ductile materials with elastic strain ($\varepsilon_{\mathrm{el}}$) and plastic ($\varepsilon_{\mathrm{pl}}$) strain (left). Tangential frictional force-relative displacement relation with behaviour similar to stress-strain relation (right).

The conventional formulation of the Dahl model describes both the loading and unloading stages with a non-linear behaviour. In analogy to solid mechanics, the behaviour of stick to slip transition is associated with stress-strain behaviour of ductile materials, wherein the yield point refers to the transition phase [29]. Extending the same analogy between stick-slip behaviour and stress-strain relation for un-loading stage, the structure comes to a state of zero stress with non-zero strain. The non-zero strain accounts for the plastic deformation. The unloading step is associated with conservative elastic part and follows a linear elastic stiffness release. Figure 2.12 shows the pictorial representation of the discussed phenomenon. Also, many experiments used for measuring the hysteresis shape due to the contact show a linear release for the unloading phase. Thus, it can be concluded for the hysteresis shape that the loading stage has a non-linear behaviour and the unloading stage has a linear behaviour.

Mayer [67] formulated a switching function for the Mindlin-Catteno model. The switching function gives one continuous hysteresis formulation capable of defining the non-linear behaviour for loading and linear behaviour for unloading step [67]. Although the switching function was proposed for Mindlin-Catteno model, it can also be used for the Dahl model. The conventional Dahl formulation is modified with use of such an switching function, to explicitly control the switching between non-linear to linear behaviour for loading and unloading stages respectively, and vice versa. The modified Dahl formulation is presented below in equation (2.38).

$$\frac{dF_{\mathrm{T}}}{d\delta_{\mathrm{T}}} = k_{\mathrm{T}} = k_{\mathrm{T0}}\left(1 - s_{\mathrm{k}}\mathrm{sgn}\left(\dot{\delta}_{\mathrm{T}}\right)\frac{F_{\mathrm{T}}}{F_{\mathrm{C}}}\right), \tag{2.38}$$

where, the switching function is $s_{\mathrm{k}} = \left(\dfrac{1 + \mathrm{sgn}(\dot{\delta}_{\mathrm{T}} F_{\mathrm{T}})}{2}\right)$.

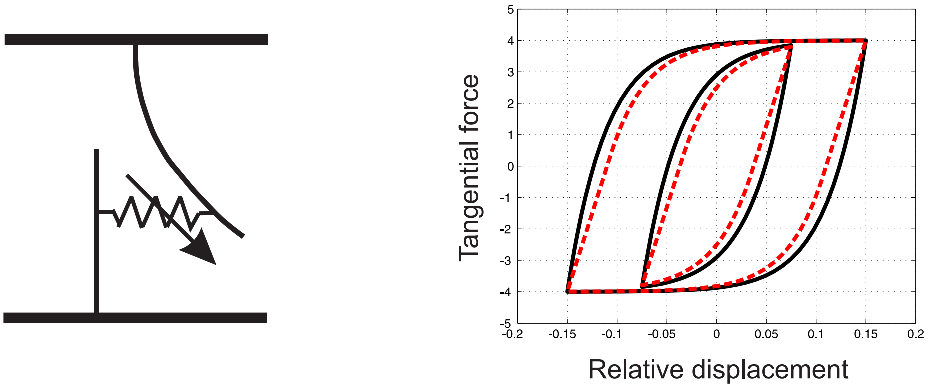

Figure 2.13: Hysteresis behaviour of Dahl friction models with two sets of excitation amplitudes. The conventional Dahl model has both loading and unloading as non-linear behaviour. The modified Dahl formulation has the loading as non-linear behaviour and unloading as linear behaviour.

Also, the criticism of Dahl model of having double the stiffness at velocity reversal is also controlled by the use of this switching function. The modified Dahl model formulation, due to the reduced slope for the unloading phase, leads to less dissipation area of hysteresis shapes than the conventional Dahl formulation. The difference in the hysteresis between the modified and conventional Dahl formulation is shown in figure 2.13, for two choices of excitation levels. Although the modified Dahl formulation traces the hysteresis curve with different stiffness in unloading stage, but the maximum value of the tangential force and relative displacement are same in both formulations.

Summary

This chapter described some of most important constitutive laws of contact mechanics for both static and dynamic loading. The contact modelling is divided into normal and tangential contact behaviour, with their respective constitutive equations describing the relation between the force and the relative displacement. The normal contact laws based on the modelling of the contact interfaces with inclusion of the surfaces roughness is discussed, which will be used as the basis for developing the constitutive equations for the proposed new model of this thesis in chapter 4. The tangential contact laws are discussed with emphasis on defining states of contact under dynamic loading - stick and slip state. The contact dissipation as hysteresis loss is depicted by dynamic dry friction model. The discussed tangential contact models will be used in chapter 3 to describe the numerical implementation of non-linear behaviour of mechanical systems having contact interfaces. A switching function is used to modify the conventional Dahl dynamic contact model. This enables a non-linear behaviour for loading step and a linear behaviour for unloading step in the hysteresis curve. Thus, the modified Dahl model overcomes the criticism of conventional Dahl model having double stiffness at load reversals. This modified Dahl model will be used in chapter 4 to derive the damping phenomenon of the proposed new model in this thesis.

Chapter 3

Structural Dynamics- Linear and Non-linear systems

The structural dynamics is the field of mechanics to study behaviour of structures under dynamic loads. The dynamical behaviour can be characterized in both time and frequency domain based on the required application. For the frequency domain representation, the important outputs for studying the vibrational behaviour are the resonance frequency and the response amplitude at resonance frequencies. This chapter discusses the modelling approaches used in analytical and experimental methods for identification of system's dynamical characteristics.

3.1 Elastodynamics

The governing equation of motion for an elastic media is obtained by use of continuum physics. For an elastic continuum, the governing equations are derived based on the kinematic, equilibrium and constitutive relations. The continuity equation for small deformation and the conservation of linear momentum defines the well known Cauchy's equation of motion. A generalized Hooke's law defines the constitutive law for elastic medium, also known as the material law. This defines a linear relation between the stress and strain tensors with a material constant called as compliance tensor. Based on mentioned laws, the governing equation for elastodynamics is obtained from equations (3.1), (3.2) and (3.3) and shown in equation(3.4).

$$\text{Cauchy motion equation:} \qquad \sigma_{ji,j} + \rho b_i = \rho \ddot{u}_i. \tag{3.1}$$

$$\text{Kinematic equation:} \qquad \varepsilon_{ij} = \frac{1}{2}\left(\frac{\partial u_i}{\partial x_j} + \frac{\partial u_j}{\partial x_i}\right). \tag{3.2}$$

$$\text{Constitutive equation:} \qquad \sigma_{ij} = C_{ijkl}\varepsilon_{kl}. \tag{3.3}$$

Elasto-dynamics governing equation:

$$C_{ijkl}u_{k,ij} + \rho b_i = \rho \ddot{u}_i. \tag{3.4}$$

The governing equation (3.4) represented in the differential form, also referred to as the strong form, requires both the boundary and initial conditions to solve the equation in space and time. The boundary conditions are defined on the primary (displacement) and secondary variable (traction), referred as Dirichlet and Neumann boundary condition respectively. The initial conditions are defined on the displacement and velocity.

Dirichlet Boundary condition:

$$u_i = \bar{u}, \qquad \text{for} \quad \partial\Omega = \partial\Omega_u. \tag{3.5}$$

Neumann Boundary condition:

$$t_i = \bar{t}, \qquad \text{for} \quad \partial\Omega = \partial\Omega_t. \tag{3.6}$$

Initial conditions:

$$\begin{aligned} u_i(t=0) &= u_i^0, & \text{for} \quad \Omega. \\ \dot{u}_i(t=0) &= \dot{u}_i^0, & \text{for} \quad \Omega. \qquad (3.7) \\ & & (3.8) \end{aligned}$$

Finite Element Method

The finite element method [130] is one of the most famous numerical method to obtain the approximate solutions for the boundary value problems in structural mechanics. For a body (Ω) with certain prescribed boundary condition, the body can be discretized into the combination of different small continuum domains. The strong form of the governing equation is required to be transformed into a weak form, also referred as the integral form. The integral form representation reduces the order of equation and satisfies the natural boundary condition over domain boundaries. Although, the solutions obtained are approximate solutions, the accuracy of approximate solution depends on the order of the discretization. Among different methods of weighted residuals, generally used is Galerkin Method [130], wherein the integral form of elastodynamics equation can be obtained by weighting the integral residue with a test function w as,

$$\int_{\Omega} \Big(C_{ijkl}\tilde{u}_{k,lj} - \rho\ddot{\tilde{u}}_i + \rho b_i \Big) w_i \mathrm{d}\Omega = 0. \tag{3.9}$$

Here, the analytical solution (u) is replaced with an approximate solution ($\tilde{u}$). When the inertia term $\rho\ddot{\tilde{u}}_i$ is zero, the elastodynamics problem reduces to the elastostatics problem. Elastostatic problem is governed only based on the spacial displacement and forces acting on the body.

The finite element method essentially uses the test function to be chosen as a virtual displacement i.e. $w = \delta\tilde{u}$, based on the approach of Bubnov-Galerkin [130]. The approximate displacement solution is described by use of finite elements, wherein the shape functions (N) are defined at elements level for N_e number of elements as,

$$\tilde{u}(\boldsymbol{x},t)=\sum_{n=1}^{N_\mathrm{e}} N_n(\boldsymbol{x})\hat{u}_n(t). \tag{3.10}$$

Hence, the elastodynamics equation in integral form on a discretized domain can be represented in the generalized form of equilibrium as,

$$\underbrace{\int_\Omega \delta\hat{\boldsymbol{u}}^T \boldsymbol{N}^T \boldsymbol{N}\rho\ddot{\hat{\boldsymbol{u}}}\ \mathrm{d}\partial\Omega}_{\delta W_\mathrm{dyn}}+\underbrace{\int_\Omega \delta\hat{\boldsymbol{u}}^T \boldsymbol{D}^T \mathbb{C}\boldsymbol{D}\hat{\boldsymbol{u}}\ \mathrm{d}\Omega}_{\delta W_\mathrm{int}}=\underbrace{\int_{\partial\Omega} \delta\hat{\boldsymbol{u}}^T \boldsymbol{N}^T \boldsymbol{t}\ \mathrm{d}\partial\Omega+\int_\Omega \delta\hat{\boldsymbol{u}}^T \boldsymbol{N}^T \rho\boldsymbol{b}\ \mathrm{d}\Omega}_{\delta W_\mathrm{ext}}. \tag{3.11}$$

The above representation contains the common term of virtual displacement $\delta\hat{\boldsymbol{u}}^T$ on both left hand side and right hand side of equation and hence can be cancelled on both side. Thus, reformulating to the conventional reduced FE equation described as the summation of the dynamical forces, inner forces and external forces. This leads to the generalized form of vibration equation and is represented as,

$$\boldsymbol{M}\ddot{\boldsymbol{u}}(t)+\boldsymbol{K}\boldsymbol{u}(t)=\boldsymbol{F}(t), \tag{3.12}$$

where, $\boldsymbol{M}$ and $\boldsymbol{K}$ refers to the mass matrix and stiffness matrix of the system respectively. Also $\boldsymbol{F}(t)$ represents the time varying external forces acting on the system.

3.1.1 Linear Vibrations

The elasto-dynamic equation represents the balancing of inner and external forces, wherein the inner forces are defined as the contribution from the inertia and elastic restoring forces. However, to depict the actual behaviour of systems, the different losses existing for the system need to be included. The generalized vibration equation is represented with an equivalent viscous damping coefficient $\boldsymbol{D}$ as [9],

$$\boldsymbol{M}\ddot{\boldsymbol{u}}(t)+\boldsymbol{D}\dot{\boldsymbol{u}}(t)+\boldsymbol{K}\boldsymbol{u}(t)=\boldsymbol{F}(t). \tag{3.13}$$

The above generalized form of vibration equation describes a system in space and time with differential operator of second order. With assumption of mass, damping and stiffness being independent of time, equation (3.13) is defined as a linear system. The theory of free vibration is first introduced by LORD RAYLEIGH(1887) [95]. The steady state response of system can be taken as $\boldsymbol{u}(x,t)=\boldsymbol{\phi}(x)\exp(i\omega t)$. The solution for the free vibration of the system is obtained by taking zero forces of excitation and solving for a set of homogeneous equations.

$$\left(-\omega^2\boldsymbol{M}+\boldsymbol{K}\right)\boldsymbol{\phi}(x)\exp(i\omega t)=0. \tag{3.14}$$

The equation (3.14) posses the non-trivial solution and is solved as an eigenvalue problem, i.e. $\det(\boldsymbol{K}-\omega^2\boldsymbol{M})=0$. The results of eigenvalues corresponds to the natural angular frequency (modal angular frequency) and the eigenvectors corresponds to the mode shape. With mass ortho-normalization, the equivalent modal mass and stiffness can be reduced to unit matrix and diagonal matrix of modal angular frequencies respectively,

$$\begin{aligned}\Phi^T_{[\mathrm{Nn\ x\ Nm}]}\boldsymbol{M}_{[\mathrm{Nn\ x\ Nn}]}\Phi_{[\mathrm{Nn\ x\ Nm}]} &= I_{[\mathrm{Nm\ x\ Nm}]},\\ \Phi^T_{[\mathrm{Nn\ x\ Nm}]}\boldsymbol{K}_{[\mathrm{Nn\ x\ Nn}]}\Phi_{[\mathrm{Nn\ x\ Nm}]} &= \mathrm{diag}(\omega^2_{\mathrm{m}})_{[\mathrm{Nm\ x\ Nm}]}.\end{aligned} \tag{3.15}$$

The ortho-normality principle makes the transformation from physical co-ordinates to modal co-ordinates using : $\boldsymbol{u}=\boldsymbol{\Phi q}$. The vibration equation can be re-written in modal co-ordinate by using the reduced diagonal matrices based on equation (3.15), leading to system of de-coupled equations.

$$\begin{aligned}\Phi^T\boldsymbol{M}\Phi\ddot{\boldsymbol{q}}+\Phi^T\boldsymbol{D}\Phi\dot{\boldsymbol{q}}+\Phi^T\boldsymbol{K}\Phi\boldsymbol{q} &= \Phi^T\boldsymbol{F}.\\ \boldsymbol{I}\ddot{\boldsymbol{q}}+\Phi^T\boldsymbol{D}\Phi\dot{\boldsymbol{q}}+\omega^2_m\boldsymbol{q} &= \Phi^T\boldsymbol{F}.\end{aligned} \tag{3.16}$$

The estimation of damping is quite difficult, as it needs to accommodate for all predominant losses. A direct implementation of damping in modal co-ordinates needs the reduction of damping matrix to a diagonal matrix. Following section discusses the formulations of vibration damping in linear systems.

3.1.1.1 Formulations for Vibration Damping

The damping is either inherent in the material or added through external means. There are different formulations available to accommodate the damping behaviour for the structural vibrations, but still damping remains to be a challenging topic. The vibration equation (3.16) in modal coordinates essentially reduces the system matrices to diagonal terms, and similar reduction for damping matrix is too required. A brief introduction to the role of damping in vibration can be found in work of CRANDALL [26] and GAUL [35, 37]. Formulations of viscous and non-viscous damping for the general vibration equation are presented in following discussions.

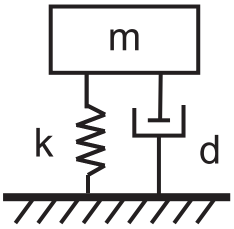

Figure 3.1: A schematic representation of single degree freedom system with mass, damper and stiffness.

Viscous- Material damping

Material damping on a macro-scale is associated with the dissipation of the continuum media. The simplest definition of the damping in dynamics is visco-elastic damping motivated from the fluid mechanics. For a single degree of freedom (*sdof*) system as shown in figure 3.1, the vibration equation is written the in reduced and decoupled form with use of the damping ratio as [51],

$$m\ddot{u} + d\dot{u} + ku = F(t) \implies \ddot{u} + 2\zeta\omega_n\dot{u} + \omega_n^2 u = f_0(t), \tag{3.17}$$

here, the damping ratio ζ is defined as the ratio of the actual to critical damping. The values of $\zeta < 1$, $\zeta = 1$ and $\zeta > 1$ refer to cases of under damped (oscillations), critical damped and over damped system (no oscillations) respectively. The damped angular frequency (ω_d) and damping ratio are calculated in terms of natural angular frequency (ω_n) as,

$$\omega_d = \omega_n\sqrt{1-\zeta^2}; \quad \omega_n = \sqrt{\frac{k}{m}} \qquad \text{where,} \quad \zeta = \frac{d}{d_{\text{cr}}} = \frac{d}{2m\omega_n}. \tag{3.18}$$

The total internal force (F_{int}) is the addition of the elastic restoring force (F_{el}) and the viscous dissipative force (F_{d}). The relation between the total internal force and the displacement is an inclined ellipse. The area of the ellipse is associated to the damping loss and the inclination is associated to the stiffness of the system. Figure 3.2 shows the visco-elastic system hysteresis for steady state harmonic response $u = U_0\cos(\omega t)$ of a *sdof* system.

$$F_{\text{d}} = d\dot{u} \qquad \text{and} \qquad F_{\text{el}} = ku \tag{3.19}$$

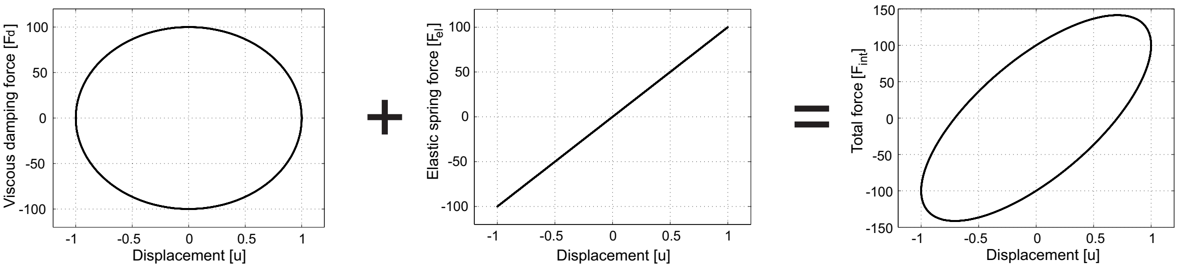

Viscous force Elastic force Visco-elastic force

Figure 3.2: The hysteresis of the visco-elastic system as the superposition of the viscous damping and elastic force.

The energy loss for the visco-elastic system is obtained by integrating the damping force for a period of oscillation as,

$$\Delta E = \oint F_d du = \int_0^{2\pi/\omega} d\dot{u}^2 dt = \int_0^{2\pi/\omega} d\omega U_0^2 \cos^2(\omega t) dt = \pi d\omega U_0^2. \tag{3.20}$$

The loss factor (η) is defined as the ratio of the viscous dissipation energy to the elastic stored energy. The elastic energy is equal to the potential energy associated with elastic spring. For excitation angular frequency equal to the natural angular frequency, the loss factor is twice the damping ratio.

$$\eta = \frac{\Delta E}{2\pi U_{\max}} = \frac{\pi d\omega U_0^2}{2\pi(1/2kU_0^2)} = \frac{d\omega}{k} = 2\big(\zeta\big)_{\omega=\omega_n} \tag{3.21}$$

Multi degree of freedom (*mdof*) system has many modes, wherein assigning each mode with an equivalent damping ratio is a cumbersome process. Definition of complete visco-elastic damping matrix (D) is required for vibration equation, see equation (3.16). The necessary condition, derived by CAUGHEY AND O'KELLY [19, 78], to attain normal mode pertaining to the general choices of the mass, damping and stiffness matrices is $\boldsymbol{K}\boldsymbol{M}^{-1}\boldsymbol{C} = \boldsymbol{C}\boldsymbol{M}^{-1}\boldsymbol{K}$. A proportional damping matrix is built on the summation of mass and stiffness matrix with their corresponding scaling factors, is often referred as the Rayleigh Damping. This form of damping can also be represented in modal angular frequency to give corresponding modal damping ratios.

$$\boldsymbol{D} = \alpha_{\mathrm{r}}\boldsymbol{M} + \beta_{\mathrm{r}}\boldsymbol{K} \quad \text{or} \quad \xi_{\mathrm{m}} = \zeta = \frac{\alpha_{\mathrm{r}}}{2\omega_{\mathrm{m}}} + \frac{\beta_{\mathrm{r}}\omega_{\mathrm{m}}}{2}. \tag{3.22}$$

The other necessary and sufficient conditions with respective arguments to attain the normal modes based on the proportional damping are covered in detail by authors NEWLAND [75], ADHIKARI [1] and PHANI [84, 85]. But it is eventually not an usual case to always have classical damping definition, wherein the damping matrices can be reduced to a diagonal matrix. Identification and solution of eigen value problem of non-viscous damping is studied by PRATER AND SINGH [54], ADHIKARI [1], PHANI [85] and others. A generalized solution method for non-proportional damping system is based on the quadratic eigen-value problem by reformulating using the state space representation as,

$$\begin{bmatrix} \dot{u} \\ \ddot{u} \end{bmatrix} = \begin{bmatrix} \mathbf{0} & \mathbf{I} \\ -\boldsymbol{M}^{-1}\boldsymbol{K} & -\boldsymbol{M}^{-1}\boldsymbol{D} \end{bmatrix} \begin{bmatrix} u \\ \dot{u} \end{bmatrix}. \tag{3.23}$$

The above equation results into $2n$ eigenvalues, i.e the conjugate pairs of the eigenvalues. Further reading on detailed understanding for the viscous non-proportional damping can be found in literature [56, 90, 108].

Non-viscous damping

Structural materials show a hysteresis behaviour under steady state excitation, wherein the hysteresis area is independent of the loading frequency. The source of this dissipation is related to the internal friction between different planes of the material under deformation. Materials or structures undergoing this form of energy dissipation are referred to hysteretic damping or structural damping [62, 87]. As the energy dissipation (ΔE) is dependent on the deformation and independent of loading frequency, they are classified under non-viscous damped systems. The energy loss due to the structural damping for a *sdof* system is calculated as [23],

$$\Delta E = \pi k \beta_{\text{hys}} U_0^2, \tag{3.24}$$

where, β_{hys} refers to the non-dimensional hysteretic damping constant. Also, this can be equated to the viscous damping ratio based on equation (3.21), such that $\beta_{\text{hys}} = 2\zeta$. Different relations between the viscous and structural damping is studied by SOROK [104]. An equivalent viscous damping coefficient (d_{eqv}) for the structural damping can be estimated by equating viscous energy dissipation to hysteretic energy dissipation as,

$$\pi d_{\text{eqv}} \omega^2 U_0^2 = \pi k \beta_{\text{hys}} U_0^2 \implies d_{\text{eqv}} = \frac{\beta_{\text{hys}} k}{\omega}. \tag{3.25}$$

The vibration equation with structural damping can be described with both equivalent visco-elastic damping or with the hysteretetic damping constant as [49],

$$m\ddot{u} + \frac{\beta_{\text{hys}} k}{\omega}\dot{u} + ku = F(t) \qquad \text{(or)} \qquad m\ddot{u} + k(1 + i\beta_{\text{hys}})u = F(t). \tag{3.26}$$

The complex formulation of the vibration equation leads to the definition of the complex stiffness, with the real part representing the elastic part and the imaginary part representing the dissipative part. Further extensive reading on the modelling of the hysteretic damping and viscous damping in terms of the complex vibration equation can be seen in NEUMARK [74], wherein many analytical formulations associated to the frequency ratio and damping loss factors are derived.

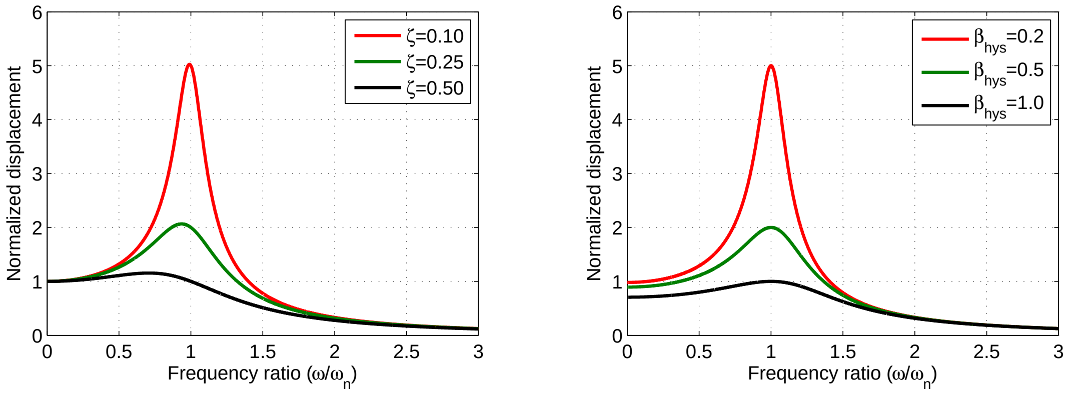

(a) Viscous damping system. (b) Structural damping system.

Figure 3.3: Effect of the damping on the frequency response of normalized displacement for a single degree of freedom system.

Figure 3.3 shows the influence of the increasing damping on the peak amplitudes and resonance frequency, for both viscous damping and structural damping. It is clearly evident that with increase in damping factor, the resonance frequency decreases in viscous damping systems. However, the resonance frequency does not change with increase in damping factor for the structural damping system.

The other forms of non-viscous damping are the system damping related to the external factors other than the inherent material property of the structural members. Some of these common sources of damping are from the joint interfaces, fluid-acoustic damping, hydro-mechanical damping, electro-mechanical interactions and other sources [62]. Among all these, the structural vibrations associated with assembled structures involving contact interfaces are interest of study in this thesis- referred to friction damping see section 2.2. This type of damping is non-linear in nature and covered in the following section of non-linear vibrations.

3.1.2 Non-linear Vibrations

A structure experiences different forms of non-linearities from geometry, material and boundary conditions [118]. All these non-linearities essentially define the change in the dynamic stiffness with respect to the loading and hence the generalized vibration equation for the non-linear system is represented as,

$$\boldsymbol{M}\ddot{\boldsymbol{u}}(t)+\boldsymbol{D}(\boldsymbol{u},\dot{\boldsymbol{u}})\dot{\boldsymbol{u}}(t)+\boldsymbol{K}(\boldsymbol{u},\dot{\boldsymbol{u}})\boldsymbol{u}(t)=\boldsymbol{F}(t). \tag{3.27}$$

Classical examples for the study of non-linear dynamic systems in terms of non-linear stiffness and damping continuations are the *Duffing's Oscillator* and the *Van-der-Pol* respectively. The Duffing's Oscillator defines a non-linear cubic stiffness and the Van-der-Pole oscillator defines a quadratic damping, as shown in the below equation [27].

$$\begin{array}{ccc} \text{Duffing's Oscillator} & & \text{Van der Pol Oscillator} \\ m\ddot{u}+d\dot{u}+ku+k_{\text{nl}}u^3=F(t) & \text{and} & m\ddot{u}-d(1-u^2)\dot{u}+ku=F(t). \end{array} \tag{3.28}$$

3.1.2.1 Numerical Solution- Duffing Oscillator

Analytical solutions are not available for all cases of non-linearity and their applications are only valid for simple geometries. Numerical methods provide a good alternative to obtain the results for non-linear problems to arguably good accuracy. The mathematical model is numerically divided into Boundary Value Problem (BVP) and Initial Value Problem (IVP). The Finite Elements (FE) are used for the domain discretization to describe the weak form of the equilibrium equation. The solution for initial value problem in combination with boundary value problem are obtained using one-stage or multi-stage time integration numerical techniques. The conventional approaches for solving IVP are Euler methods, central difference method, Runge-Kutta method etc. The solution for a non-linear equation is obtained by use of iterative Newton methods [ANANDARAJAH, Chap. 8] [4]. The non-linear system are conventionally solved in time domain but frequency domain methods can also be used to obtain steady state solution.

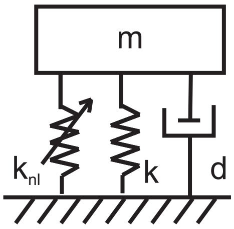

Figure 3.4: A schematic representation of Duffing's oscillator with a single degree of freedom system having non-linear cubic stiffness.

Time domain

The time domain implementation is ideally used for highly non-linear systems, to have a better prediction of the actual behaviour. Among different numerical techniques, Newmark methods have been most famous in modelling the transient behaviour of a dynamic system. The generalized approach used by NEWMARK [76] is based on the interpolation of the velocity and displacements, as presented in equations below. The equations are discretized in the time interval of $[0, T]$ with a constant time step of Δt,

$$\begin{aligned} \dot{u}^{t+\Delta t} &= \dot{u}^t + (1-\gamma)\ddot{u}^t \Delta t + \gamma \ddot{u}^{t+\Delta t} \Delta t, \\ u^{t+\Delta t} &= u^t + \dot{u}^t \Delta t + \left(\frac{1}{2} - \beta\right) \ddot{u}^t (\Delta t)^2 + \beta \ddot{u}^{t+\Delta t} (\Delta t)^2, \end{aligned} \tag{3.29}$$

wherein, γ and β are the Newmark parameters. The adaptive algorithms allow varying time steps to be used for efficient calculation [50, 98, 127]. Choices of $\gamma = 1/2$ and $\beta = 1/4$ leads to unconditional stable solution and referred as average constant acceleration algorithm. With choices of $\gamma = 1/2$ and $\beta = 0$, the numerical integration scheme is same as the central difference algorithm, with conditional stability. The Duffing's oscillator equation using respective numerical integration techniques is shown in following equations.

Central Difference Explicit method

$$\left(\frac{m}{\Delta t^2} + \frac{d}{2\Delta t}\right) u^{t+\Delta t} = F^t + \left(\frac{2m}{\Delta t^2} - k\right) u^t + \left(\frac{d}{2\Delta t} - \frac{m}{\Delta t^2}\right) u^{t-\Delta t}. \tag{3.30}$$

Newmark-β Implicit method

$$\begin{gathered} \left(\frac{m}{\beta \Delta t^2} + \frac{d\gamma}{\beta \Delta t} + k\right) u^{t+\Delta t} + k_{\mathrm{nl}} \left(u^{t+\Delta t}\right)^3 = F^{t+\Delta t} + \left(\frac{m}{\beta \Delta t^2} + \frac{d\gamma}{\beta \Delta t}\right) u^{\mathrm{t}} + \\ \left(\frac{m}{\beta \Delta t} - d\left(1 - \frac{\gamma}{\beta}\right)\right) \dot{u}^t + \left(m\left(\frac{1}{2\beta} - 1\right) - d\Delta t\left(1 - \frac{\gamma}{2\beta}\right)\right) \ddot{u}^t. \end{gathered} \tag{3.31}$$

The results from Newmark Implicit and Central difference methods are presented in figures 3.5(a) and 3.5(b) for free and forced vibration respectively. Both methods show a good match for both frequency and amplitudes of motion for the free vibration behaviour.

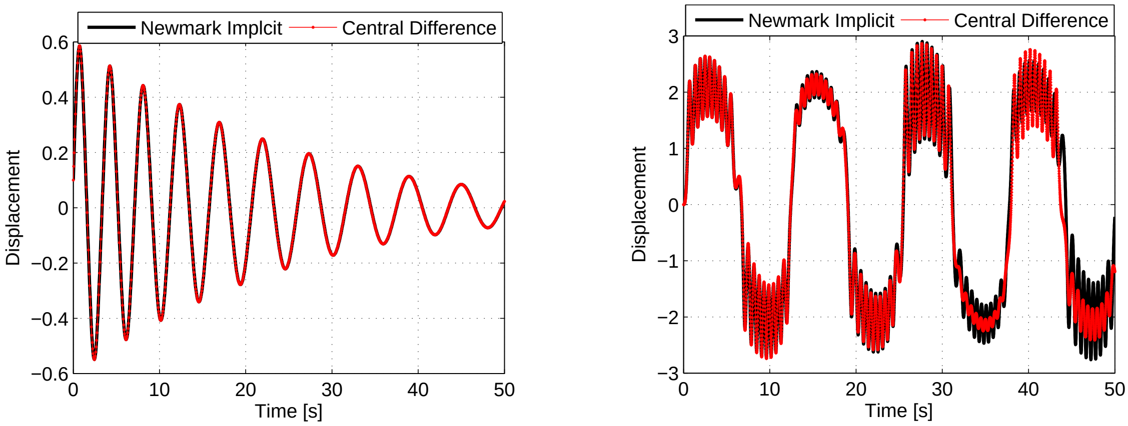

(a) Free Vibration

(b) Forced Vibration

Figure 3.5: Time marching techniques to model Duffing oscillator in free and force vibration states. Parameters used : $m = 1, d = 0.2, k = 1, k_{nl} = 10$, with free vibration initial condition of $[u(0), \dot{u}(0)] = [0.1, 1]$ and forced excitation with zero initial condition: $F(t) = 100\ \sin(0.5t) + 10\ \sin(t) + 1\ \sin(1.5t)$.

For the forced excitation, there is variation in amplitudes of vibration between the two methods at large time intervals. However, with reducing the time step size, the errors can be reduced.

Although time domain implementation is a direct non-linear form implementation with capturing the non-linear effect to a good accuracy, it is computational costly. The Newton iteration used to solve non-linear problem, has often problems with convergence which also depends on the initial guess value. Explicit method being faster than implicit can be used, but the explicit methods suffer the in-stability issues with respect to the time and space discretization for large systems used in FEM. Following section discusses the frequency domain representation of non-linear system like Duffing's oscillator.

Frequency domain

The disadvantage of time domain description are overcome here by describing the vibration equation in frequency domain, to describe the stationary part of the solution. One of the methods used to describe the non-linear system in frequency domain is the Harmonic Balance Method (HBM). The harmonic balance method is the transformation of the non-linear forcing term into series of Fourier coefficients, such that the non-linear vibration equation is transformed into a equation involving Fourier terms as the unknown primary variables. URABE (1966) [116] was one among the first to present the method. Later LAU AND CHEUNG [24, 60] extended the method and is referred as Incremental HBM. The incremental HBM was used to solve a beam structure with local cubic non-linearity [60]. The conventional HBM involves two steps. First step is to determine the linear dynamic stiffness matrix and in second step the non-linear forces are represented in terms of Fourier coefficients. Following equations show the representation of the Duffing's oscillator using HBM.

$$u(t) = u_0 + \sum_{n=1}^{N_\mathrm{H}} u_{2n-1}\cos(n\omega t) + u_{2n}\sin(n\omega t) \tag{3.32}$$

$$\dot{u}(t) = \sum_{n=1}^{N_\mathrm{H}} -n\omega u_{2n-1}\sin(n\omega t) + n\omega u_{2n}\cos(n\omega t) \tag{3.33}$$

$$\ddot{u}(t) = \sum_{n=1}^{N_\mathrm{H}} -n^2\omega^2 u_{2n-1}\cos(n\omega t) - n^2\omega^2 u_{2n}\sin(n\omega t) \tag{3.34}$$

The non-linear cubic term of the Duffing's oscillator can be rewritten in Fourier coefficients as,

$$u(t)^3 \simeq r_0 + \sum_{n=1}^{N_\mathrm{H}} r_{2n-1}\cos(n\omega t) + r_{2n}\sin(n\omega t). \tag{3.35}$$

The Fourier coefficients of the non-linear term (r_0, r_{2n-1} and r_{2n}) are calculated by inverse Fourier transformation as,

$$\begin{aligned} r_0 &= \frac{1}{T}\int_0^T \left(u_0 + \sum_{n=1}^{N_\mathrm{H}} u_{2n-1}\cos(n\omega t) + u_{2n}\sin(n\omega t) \right)^3 dt. \\ r_{2n-1} &= \frac{2}{T}\int_0^T \left(u_0 + \sum_{n=1}^{N_\mathrm{H}} u_{2n-1}\cos(n\omega t) + u_{2n}\sin(n\omega t) \right)^3 \cos(\omega t) dt. \\ r_{2n} &= \frac{2}{T}\int_0^T \left(u_0 + \sum_{n=1}^{N_\mathrm{H}} u_{2n-1}\cos(n\omega t) + u_{2n}\sin(n\omega t) \right)^3 \sin(\omega t) dt. \end{aligned} \tag{3.36}$$

Replacing above equations in the Duffing's oscillator equation (3.28), non-linear cubic stiffness terms in frequency domain is obtained. A sinusoidal force excitation with assumptions of $u_0 = 0$ and $r_0 = 0$ are used to analytically calculate the non-linear Fourier terms with a reduced size of the problem.

$$-m\omega^2 u_1 + d\omega u_2 + k u_1 + \frac{3}{4}k_{nl}\left(u_1{}^3 + u_1 u_2{}^2\right) = 0. \tag{3.37}$$

$$\underbrace{-m\omega^2 u_2 - d\omega u_1 + k u_2}_{\text{linear part}} + \underbrace{\frac{3}{4}k_{nl}\left(u_2{}^3 + u_2 u_1{}^2\right)}_{\text{non-linear part}} = F_0. \tag{3.38}$$

Solving equations (3.37) and (3.38) for both forward and backward sweep of sinusoidal excitation, results in two different frequency response spectrum, as shown in figure 3.6(a). The Duffing oscillator having the cubic displacement term suggests existence of the three solutions, with all three stable solutions existing in the range of angular frequency (1.6 - 2.3) rad/s.

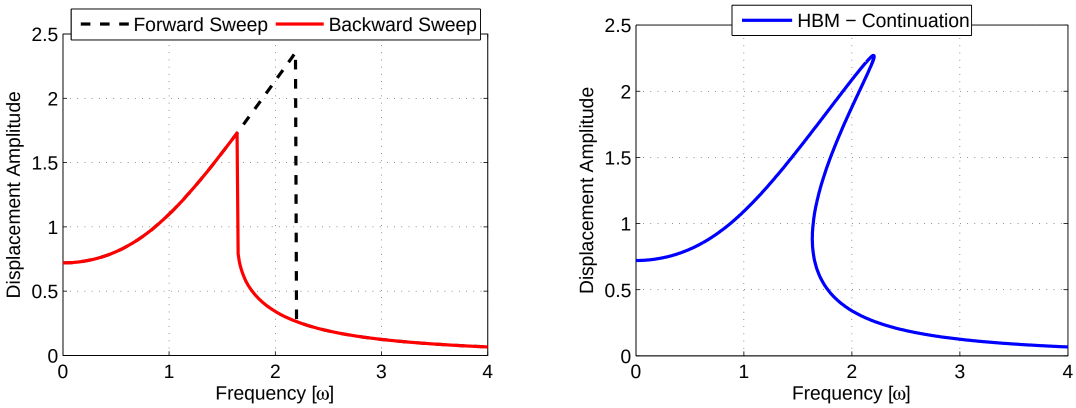

(a) Harmonic Balance with Newton raphson iterations

(b) Harmonic Balance with continuation method

Figure 3.6: Duffing's Oscillator in frequency domain with region of instability-cubic term having all three valid equilibrium solutions. Parameters Used : $m = 1, d = 0.2, k = 1, k_{nl} = 1, F(t) = \sin(\omega t)$.

The HB equation when solved using the newton iterations can only yield one solution in a sweep direction and hence leads to two different branches with respect to sweeping direction. With use of continuation methods, the non-linear frequency response behaviour in the unstable-hysteresis region can be captured, see figure 3.6. This is similar to arc control method used in non-linear mechanics [117]. In the continuation method, the residue equation is modified with inclusion of frequency also an unknown variable.

$$R(u_1; u_2) \overset{!}{=} 0 \qquad \rightarrow \qquad R(\omega; u_1; u_2) \overset{!}{=} 0. \tag{3.39}$$

The linear system have no influence of excitation amplitude on the frequency response function. For a non-linear system, with increase in the excitation amplitude change in the frequency response function amplitude and the resonance frequency is obtained. For a non-linear system like the Duffing Oscillator, the non-linear behaviour with respect to excitation amplitude is shown in figure 3.7.

HBM with one harmonic is not sufficient to capture the higher and sub-harmonics existing in non-linear system. Work of CARDON ET.AL [16, 17] and other authors on multi harmonic balance method have been successful in modelling the higher and sub-harmonics. The Alternating Frequency Time (AFT) domain representation [15, 17] have been helpful in terms of dealing strong non-linearities. One of derivatives and approximate method of AFT is High Dimensional-Harmonic Balance Method (HD-HBM) [65, 66]. The HD-HBM is advantageous in capturing the higher harmonics of the system with requirements of no analytical expression of non-linear terms in Fourier coefficients. Following steps describe the usage of HD-HBM for Duffing's oscillator.

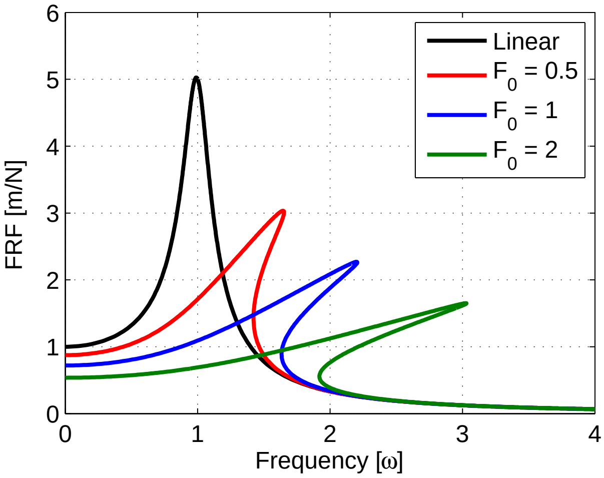

Figure 3.7: Non-linear behaviour of Duffing's Oscillator in frequency domain using Harmonic Balance Continuation method with one harmonic.

Step 1: Representing $(2N_\mathrm{H}+1)$ harmonics for displacement Fourier coefficients with $(2N_\mathrm{H}+1)$ equally time spaced displacement in the time domain.

$$\hat{U} = T_{\mathrm{IFFT}}\tilde{U}, \tag{3.40}$$

$$\hat{U} = \begin{bmatrix} u_0 \\ u_1 \\ u_2 \\ . \\ . \\ . \\ . \\ u_{2N_\mathrm{H}} \end{bmatrix}; \quad \tilde{U} = \begin{bmatrix} u(t_0) \\ u(t_1) \\ u(t_2) \\ . \\ . \\ . \\ . \\ u(t_{2N_\mathrm{H}}) \end{bmatrix}; \quad T_{\mathrm{IFFT}} = \begin{bmatrix} 1/2 & 1/2 & \dots & 1/2 \\ \cos(t_0) & \cos(t_1) & \dots & \cos(t_{2N_\mathrm{H}}) \\ \sin(t_0) & \sin(t_1) & \dots & \sin(t_{2N_\mathrm{H}}) \\ \cos(2t_0) & \cos(2t_1) & \dots & \cos(t_{2N_\mathrm{H}}) \\ \sin(2t_0) & \sin(2t_1) & \dots & \sin(t_{2N_\mathrm{H}}) \\ . & . & & . \\ . & . & & . \\ . & . & & . \\ \cos(N_\mathrm{H}t_0) & \cos(N_\mathrm{H}t_1) & \dots & \cos(N_\mathrm{H}t_{2N_\mathrm{H}}) \\ \sin(N_\mathrm{H}t_0) & \sin(N_\mathrm{H}t_1) & \dots & \sin(N_\mathrm{H}t_{2N_\mathrm{H}}) \end{bmatrix}.$$

Step 2: Defining the cubic non-linearity and excitation forces in $(2N_\mathrm{H}+1)$ equally time spaces as,

$$\tilde{R} = \begin{bmatrix} u(t_0)^3 \\ u(t_1)^3 \\ u(t_2)^3 \\ . \\ . \\ . \\ . \\ u(t_{2N_\mathrm{H}})^3 \end{bmatrix}; \quad \tilde{F} = \begin{bmatrix} F(t_0) \\ F(t_1) \\ F(t_2) \\ . \\ . \\ . \\ . \\ F(t_{2N_\mathrm{H}}) \end{bmatrix}. \tag{3.41}$$

Step 3: Transforming the representation of the HBM equation to HD-HBM, by transforming the Fourier coefficients to time domain using T_{IFFT} and later multiplying by ${T_{\text{IFFT}}}^{-1}$,

$$K_{\text{lin}}\left(T_{\text{IFFT}}\tilde{U}\right)+k_{\text{nl}}\left(T_{\text{IFFT}}\tilde{R}\right) = T_{\text{IFFT}}\tilde{F}, \tag{3.42}$$

$$\left({T_{\text{IFFT}}}^{-1}K_{\text{lin}}T_{\text{IFFT}}\right)\tilde{U}+k_{\text{nl}}\tilde{R} = \tilde{F}, \tag{3.43}$$

where, K_{lin} is the linear dynamic stiffness. Above HD-HBM equation (3.43) is defined in time domain, which can be directly solved using the conventional time marching techniques for a choice of frequency of excitation. It has been shown that the accuracy of the results improves with increases in the number of harmonics and convergences to analytical HB solution for number harmonics equal to infinity. Figure 3.8 shows the frequency response displacements for cases of forward and backward sweeps using one and eight harmonics. It is clearly seen from the results that forward sweep does not capture any non-linear resonance using one harmonic but with use of 8 harmonics, the peak amplitude for the forward sweep is correctly captured. In both forward and backward sweep, the sub-harmonic peak scan be seen for choice for higher harmonics case.

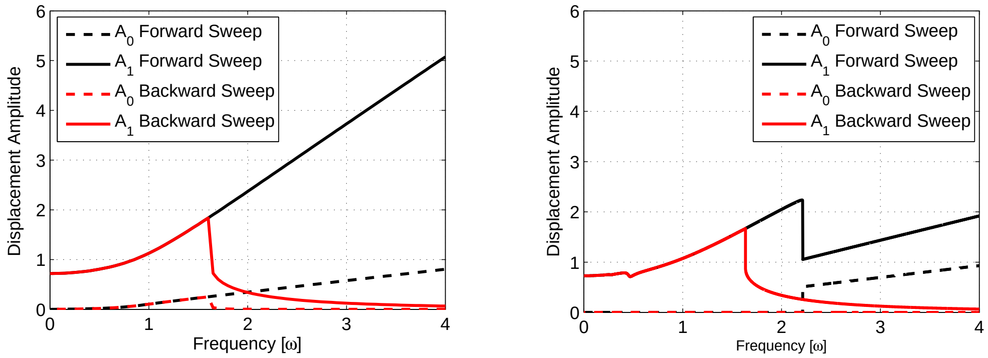

(a) HD-HBM with 1 harmonic. (b) HD-HBM with 8 harmonics.

Figure 3.8: HD-HBM with forward and backward sweep to capture the frequency response of Duffings Oscillator. Parameters Used : $m = 1, d = 0.2, k = 1, k_{nl} = 1, F(t) = \sin(\omega t)$. Harmonics amplitude : $A_0 = |u_0|$ and $A_1 = \sqrt{u_1^2 + u_2^2}$.

It was also showed later by Dai et.al 2012 [30], that the HD-HBM is essentially a derived form of time collocation method. Other methods too, like Non-linear Output FRF [82], Improved Incremental HB-Galerkin method and many more are proposed by authors in literature for non-linear system representation in frequency domain. But it is to be realized that with increasing harmonics, the number of equations are increased and hence the increase in computational efforts. Also, the implementations have been on the non-linear behaviour for the stationary operation under harmonic loading. The HBM and its derivatives are not feasible for multi modal excitations like broad band random excitation. The vibration behaviour with systems having contact is studied briefly in the next section based on the presented approaches.

3.1.2.2 Numerical Solution- Vibration with contacts

The Duffing or Van der Pol non-linear oscillator are good academic examples but implementation of more generalized non-linear constitutive laws, like dry friction contacts is still very challenging. The complexity come from the change in the state of the system (stick or slip) under dynamic excitation. This section will give a brief discussion on the implementation of the time and frequency domain approaches for the constitutive contact laws of Coulomb friction and Mindlin-Catteno contact models. The formulations related to both Coulomb and Mindlin-Catteno models have been discussed in chapter 2.

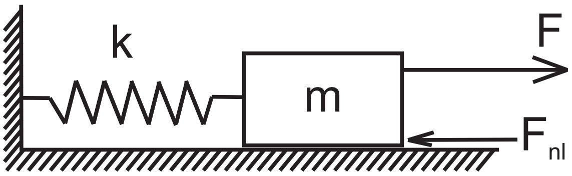

Figure 3.9: A schematic representation of single degree of freedom system with friction force from contact interface.

Time domain

The non-linear contribution from the contacts is taken as an equivalent term of inner force (F_{nl}) in the vibration equation. The non-linear force due to contact can be described based on the constitutive friction laws. The time domain vibration equation for *sdof* systems with non-linear force term is presented below as,

$$m\ddot{u}(t)+d\dot{u}(t)+ku(t)+F_{\mathrm{nl}}=F(t), \tag{3.44}$$

where,

$$F_{\mathrm{nl}}=\begin{cases} F_{\mathrm{c}}\mathrm{sgn}(\dot{u}) & \text{Coulomb model.} \\ F_{\mathrm{c}}\left(1-\left(1-\dfrac{u(t)}{u_{\max}}\right)^{3/2}\right) & \text{Mindlin-Catteno model.} \end{cases} \tag{3.45}$$

Figure 3.10 shows the time displacement response of a *sdof* system for free vibration using the two models of dry friction contact. The system is solved with zero viscous damping input and the damped response is completely due to the influence from the contact damping. For the Coulomb model, there stick and slip state. The transition point is defined for a critical displacement limit, above which the system slides and below which the system is in stick phase. However, as discussed in the chapter 2 on contact modelling for microscopic scales, ideally there exists the micro-slip damping too in the stick state. This is captured using the Mindlin-Catteno model, which shows a continuous smooth damped response with region of stick undergoing the micro-slip damping.

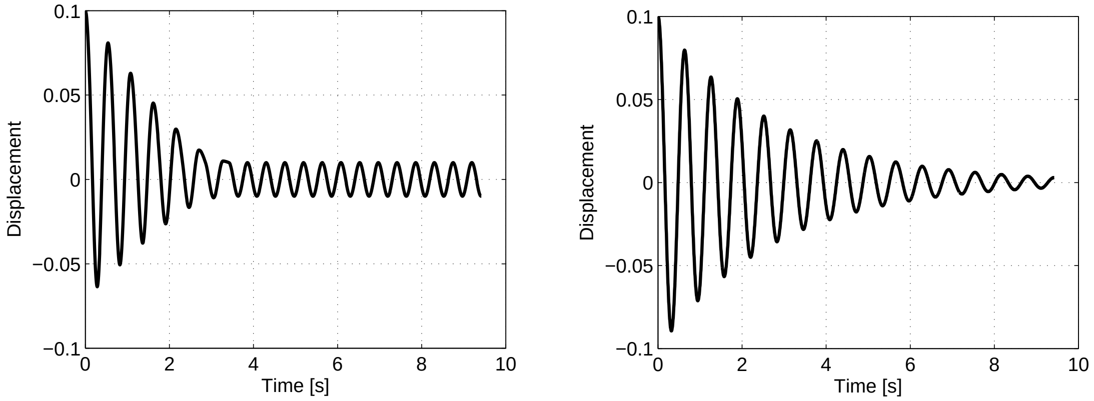

(a) Coulomb Model

(b) Mindlin-Catteno Model

Figure 3.10: Free vibrational behaviour of a *sdof* with Coulomb and Mindlin-Catteno model. Parameters Used : $m = 1, d = 0, k = 1, F_c = 1$. Initial conditions are $u(t = 0) = 0.1$ and $\dot{u}(t = 0) = 0$.

A *sdof* having non-linear force due to dry contact leads to generation of hysteresis between the non-linear force and the displacement. For steady state excitation like a sine sweep, it is observed that the hysteresis generated is a well defined closed loop with area under hysteresis associated to contact damping, see figure 3.11. Also, it is observed that the hysteresis generated is independent of frequency of excitation. However, for the random excitation the generated hysteresis has chaotic behaviour, see figure 3.12. This shows that contact formulations for the non-deterministic excitations lead to very complex behaviour, which cannot be directly interpreted as the equivalent damping from the contacts. Hence, it is concluded that the time domain representation has lot of complexity when dealing with large models excited under random vibrations.

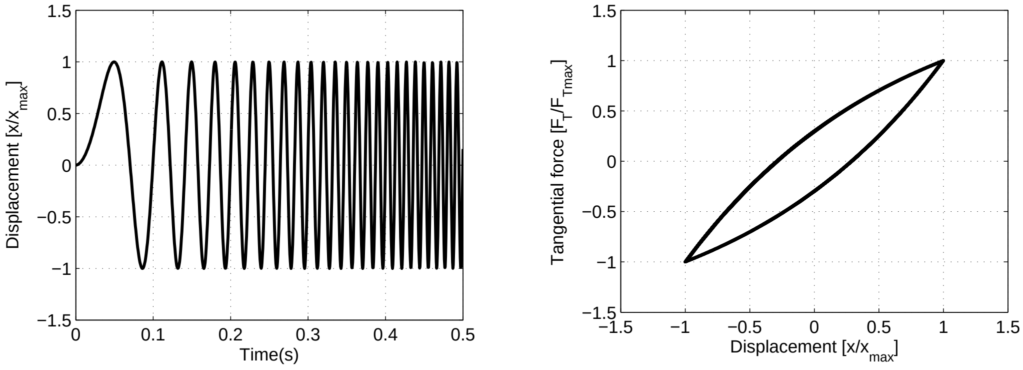

(a) Input sinesweep displacement

(b) Hysteresis for sinesweep input

Figure 3.11: The generation of hysteresis due to steady state excitation based on the Dahl model for dry frictional contacts under sine sweep excitation.

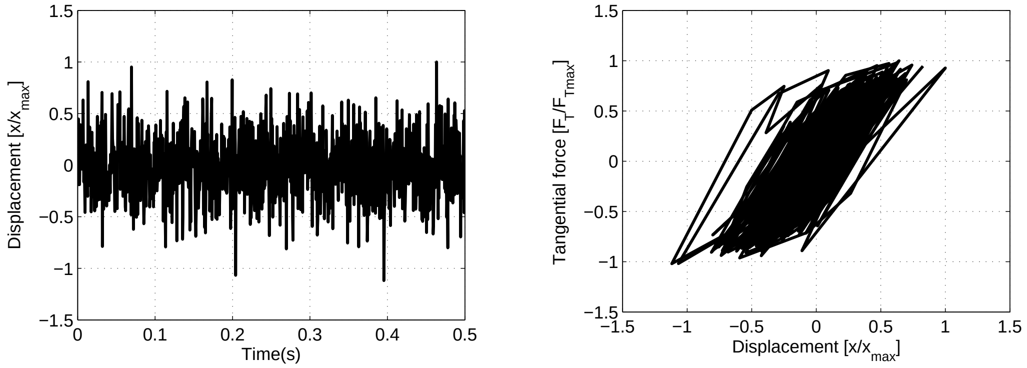

(a) Input random displacement (b) Hysteresis for random input

Figure 3.12: The generation of hysteresis due to steady state excitation based on the Dahl model for dry frictional contacts under random excitation.

Frequency domain

The frequency domain representation for the Coulomb friction is possible with use of equivalent contribution as Coulomb damping. Based on the energy dissipation for a period of oscillation, the equivalent viscous damping for Coulomb friction force is obtained as,

$$\pi d^{c}_{eqv}\omega U_0^2 = 4F_cU_0 \qquad \Longrightarrow \qquad d^{c}_{eqv} = \frac{4F_c}{\pi U_0\omega}. \tag{3.46}$$

Hence, the non-linear force for Coulomb model can be equated with the above expression, which is similar to the equivalent viscous damping coefficient for structural damping presented in equation (3.25). Here the equivalent damping has inverse proportionality to the excitation frequency. This suggest that the damping due to the frictional contacts can be characterized with structural damping. The important aspect of the equivalent damping coefficient is the dependence on the amplitude of response U_0. The analytical expression for the displacement frequency response for a *sdof* with above equivalent damping expression can be obtained as [51],

$$\frac{kU_0}{F_0} = \frac{(1-(4F_c/\pi F_0)^2)}{|(1-(\omega/\omega_n)^2)|}. \tag{3.47}$$

The displacement response is infinite at the resonance, which essentially relates to the un-damped resonance behaviour of the system although defined is a equivalent damping. However, there is certainly an amount of damping (numerator), which damps the systems with equal values for all the frequencies. Also, the steady state response formulations are valid for the condition that the excitation force amplitude (F_0) is $4/\pi$ times larger than the Coulomb sliding limit (F_c). While solving in frequency domain i.e. for the steady state representation, the Coulomb model formulation remains constant and needed is a discontinuous switching function. This leads to instability and divergence. Also, the behaviour of the Coulomb model is essentially to model the behaviour of systems while under sliding and the behaviour in the stick region with some elastic linear behaviour.

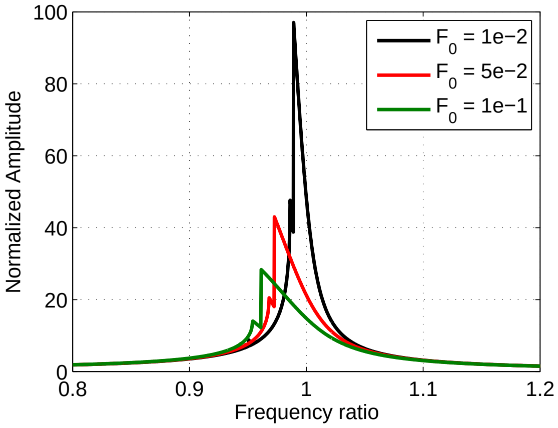

Figure 3.13: Non-linear frequency response of normalized displacement for modelling the micro-slip behaviour using Mindli-Catteno model, for sdof system with friction see figure 3.9.
Parameters Used : $m = 1, d = 0, k = 3000, F_c = 1, F = F_0 \sin(\omega t)$.

The Mindlin-Catteno model representation in frequency domain with equivalent damping is not possible analytically. A possible implementation is through the use of HD-HBM method, with calculations of the non-linear force vector in time domain at discrete harmonic time intervals. Figure 3.13 shows the non-linear behaviour of frequency response normalized displacement with increase in the excitation amplitudes. The Mindlin-Catteno formulation leads to increase in the hysteresis area with increase in the excitation amplitude and hence increase in damping. The increase in the hysteresis area with change in shape of hysteresis leads to decrease in the equivalent stiffness. Hence, the resonance frequency of system decreases with increase in excitation amplitude. But the results show instability near before resonance, which is due to the shortcoming of the frequency domain representation of non-linearity.

From the study on non-linear vibrations (Duffing's oscillator and frictional contacts), it is evident that the numerical techniques provides good approximations to capture the dynamical behaviour in both time and frequency domain. However the methods do not look promising for large degree of freedom system under broad band excitations. The time domain methods experience difficulties in convergence with large computational time. The frequency domain methods require higher harmonics, which leads to large model size. The random excitations too cannot be captured with family of HB methods. These observations with conventional techniques motivates to build a new model to capture non-linearity and is feasible for large systems under broad band excitations. The quality of the simulation results are always validated with measurement results. The next section discusses the different experiment methods for system identification through data acquisition and analysis.

3.2 System Identification : Experimental Methods

The system identification relates to identifying the essential system parameters having influence on the dynamical behaviour. The concept of building the experimental modal model to estimate the dynamical characteristics of natural frequency, damping and mode shapes of a structure is referred as *Modal testing*. The experimental model is a two stage process of data acquisition and data analysis. The data acquisition relates to measurement of the raw data. The data analysis relates to interpretation of measured data in a simplified form. The experimental methods for vibration testing are used for the validation of the analytical or numerical models. Hence, the experimental results with substantial accuracy are required. The Modal testing for estimation of modal parameters is usually divided into two approaches, based on the application. The first method is Experimental Modal Analysis (EMA). Here the structure is excited with a known input, with an aim to obtain the natural dynamical behaviour of the system. The other approach is Operational Modal Analysis (OMA). Here the structural response for the field conditions with unknowns excitation force is considered and parameters estimation are made based only on the measured data. The discussion on the fundamentals of modal testing can be found in EWINS(2000). This section will discuss the topics of data acquisition and parameter estimation techniques for data analysis.

3.2.1 Experimental Data Acquisition

As the experimental results are used for the validation process, required is good quality and accuracy of the measured data. The various factor that can influence the quality of measurement data are required to be controlled like- optimal experimental set-up, uniform and constant environment temperature, de-coupling of set-up to ground and other external vibrations etc. The following section will discuss the most common excitation types and measurement techniques used in vibration analysis.

Excitation

The type and magnitude of excitation influences the system response. Excitations can be a single point or multipoint excitation for a structure. Important is the location of the excitation in modal testing, such that all the modes in the required frequency range can be excited. There exists different types of excitation, which can be characterised into two forms i.e. closed loop and open loop excitations. A closed loop controlled excitation is essentially an experiment setup with a feedback system, such that the input excitation can be controlled to some predefined user values, for example electrodynamic shaker excitation. The open-loop non-controlled excitation are the cases where the excitation can be measured but not controlled, for example modal hammer impulse excitation etc. The excitation types are discussed in following topics.

a. Sinusoidal Excitation

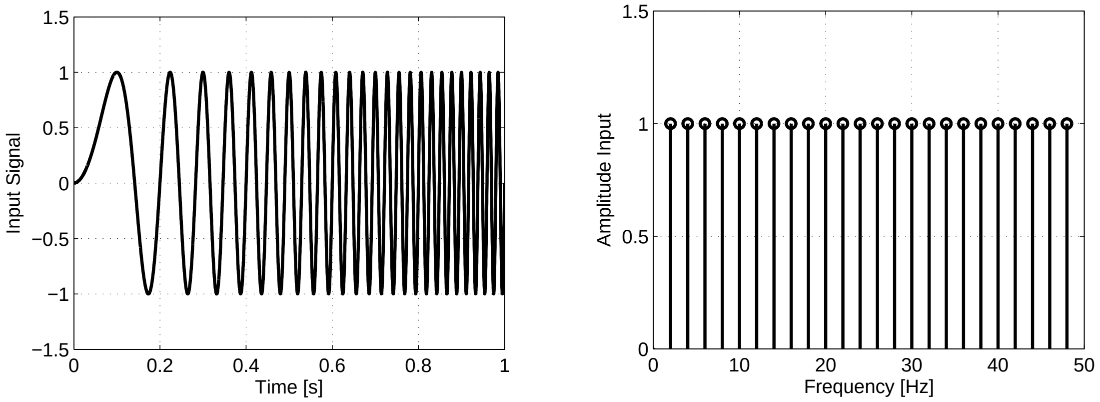

(a) Sine sweep excitation.

(b) Step sine excitation.

Figure 3.14: Amplitude controlled harmonic excitations used in experiments.

A harmonic excitation refers to exciting the structure with a mono-frequency periodic signal. This excitation method is used for the modelling of systems to describe the steady state behaviour. There are essentially two types of the harmonic excitations- sine sweep / chirp and step sine excitations. A sine sweep excitation is essentially sweeping up or down the frequencies in a specific range. Figure 3.14(a) shows an example of swept sine signal with constant amplitude in the frequency range of 0-100 Hz. There exists different sweeping techniques like- linear, exponential, log sweep etc. Although, sine sweep is a faster way to get the response of a structure for wide range of excitation frequency, but it cannot measure the peak amplitude to good accuracy. On the contrary, the step sine methods are very good in terms of providing the measurement of amplitudes of the response with very good accuracy. Here the structure is excited with every single frequency for a certain number of periodic oscillations or fixed time duration. This leads to very long duration of measurement for a systems having broad band frequency range of excitation. A representation of the step sine signal is shown in the figure 3.14(b).

b. Random Excitation

Unlike swept sine or stepped sine excitation, the field conditions experiences excitations which are essentially random in nature. The random excitations are class of non-deterministic and non-periodic signals, such that the precise magnitude at a specific time cannot be found nor be defined using a mathematical function [106]. For experimental testing for random excitations, the random signals are characterized using statistical distribution functions such that the magnitude of the input signals can be determined. The data is fitted with standard probability distribution function, such that the statistical parameters like mean, standard deviation and rms values of input amplitude can be calculated. For experimental testing, an equivalent random time signal profile is generated using the electrodynamic shaker. The time signal is generated with preserving the statistical parameter of rms amplitude, provided as an user input in some specific frequency band. Figure 3.15 shows an example of a random power spectral density profile [PSD-Power Spectral Density ($(m/s^2)^2/Hz$)] excitation and its equivalent time signals based on the inverse FFT of the frequency spectrum signals. The input profile is generally given as an input in the PSD units with discrete frequency and the interpolation between the frequency values are performed with a constant sample frequency.

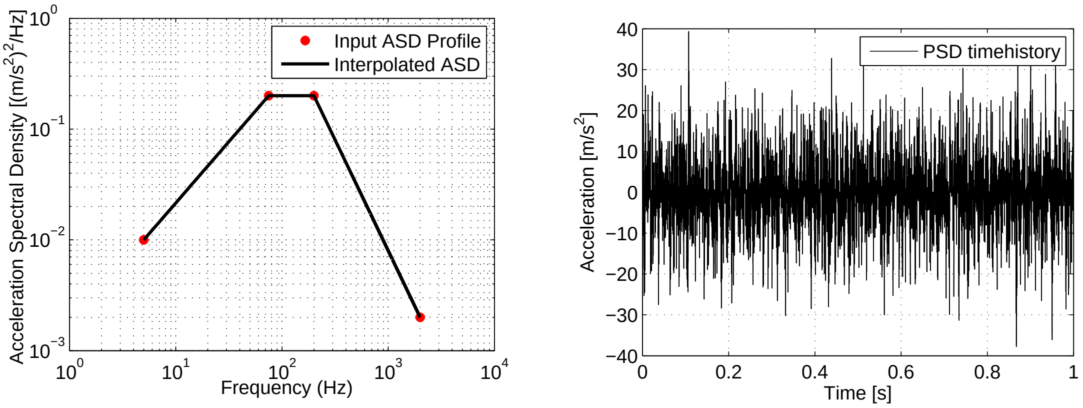

(a) Input PSD spectrum Profile.

(b) Equivalent Input time signal.

Figure 3.15: An example of input PSD profile on log-log scale with PSD values for set of frequency points specified by user in shaker settings (left). The equivalent time signal for PSD input profile used by conventional electrodynamic shaker to excite the structure for given input PSD profile with rms acceleration value of 45.2090 m/s^2 (right).

c. Impulse Excitation

Two types of impulse excitation methods are possible- roving measurement or roving excitation. In roving measurement, the measurement is taken at different locations of the structure while the excitation location remains fixed. In roving excitation, the excitation is provided at different locations while the measurement point remains fixed. For linear systems having the property of reciprocity, both roving measurement or roving excitation give the same results. The impulse excitation method is more easy and fast way of data acquisition. The impulse excitation is accomplished using a modal hammer. The system response is ideally the natural behaviour, as the excitation hammer is not connected to the structure. The choice of a modal hammer tip is important for the frequency range required to be excited. For narrow and broad frequency ranges- a soft and hard tip hammer are used respectively. This is explained as follows, the width of the impulse signal profile ideally governs the frequency range that can be excited, with constant amplitude of excitation in that frequency range. A soft and harder tip leads to broad and thin widths of the impulse profile respectively, shown in figure 3.16.

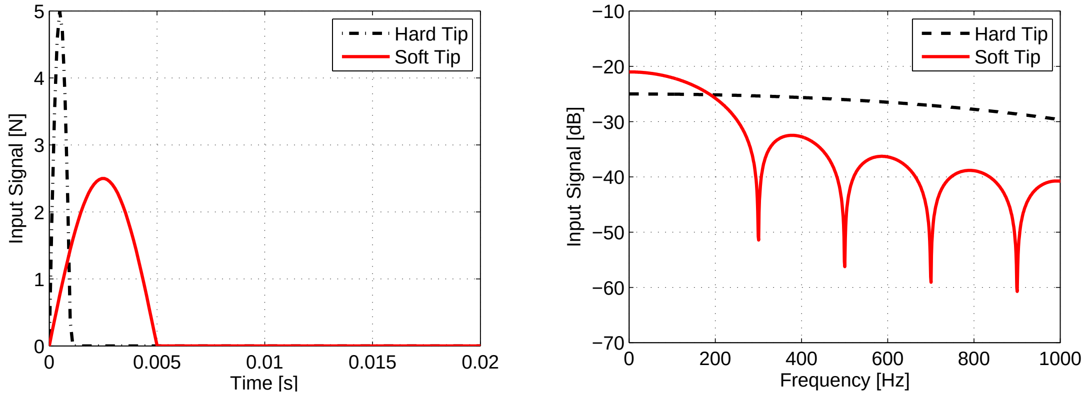

(a) Impulse signal in time domain. (b) Impulse signal in frequncy domain.

Figure 3.16: Conventional impulse excitation from hammer- with hard and soft tip showing the range of frequency excited.

Measurement

A single point measurement is possible by use of an accelerometer sensor or Laser vibrometer, where the accelerometer sensor measures the acceleration and laser vibrometer measures the velocity. For a roving measurement using accelerometers, there can be many accelerometers placed at different locations and measured simultaneously. This leads to addition of large external mass to structure from accelerometers and hence effects the dynamical characteristics. Laser vibrometer can be used for roving measurement by moving the Laser point at different locations for measurement. But the Laser can measure only upto certain levels of vibration amplitudes. Hence, a balance has to be found according to the limitation and application of both methods. When building up the mode shape of a structure, it is required to measure sufficient number of points so as to have smooth deformable continuous shapes. A fast and abstract approach of deciding on the quality of the measured data is through the calculation of coherence. Coherence defines the correlation between two signals, here in EMA between input and output signals. Unit value of coherence accounts for very good accuracy of measured data. The coherence can be evaluated reasonably by averaging the measured data. The measured data in time domain is transformed in to frequency domain and the averaging is done for the frequency spectrum signals. With use of averaging, the effect of noises can be reduced and reproducible results can be obtained. Windowing functions are used to improve the signal leakages effects. Some of the typical windowing functions used in measurements are for random excitations- Hanning/Hamming window is used for the response signal, for impulse excitation- force window is used for the input force excitation signal and exponential window is used for the response signal.

A Transfer Function (TF) is defined as the ratio of the output signal to the input signal. For the specific cases where the excitation units are of force, it is referred as Frequency Response Function (FRF). For displacement, velocity and acceleration being the measured output signal, the FRF is defined as dynamic compliance, mobility and inertance FRF's respectively. FRF's are of most importance in measurements for system identification. Linearity is defined on three principles of- superposition, homogeneity and reciprocity, i.e FRF has no dependence on the excitation type, no dependence on excitation amplitude and no dependence on switching between roving measurement-roving excitation respectively. The non-linearities are of different kinds, like a local non-linearity based on joints, which have significant influence on the global behaviour of system. With different excitation amplitudes, a linear system shows no change in FRF but a non-linear system shows different FRF. An example of two beam fastened with 4 bolted joints [see Test Structure in chapter 5] shows the variation in FRF, when excited with different levels of excitation amplitude, identifying the presence of non-linearity in system, see figure 3.17.

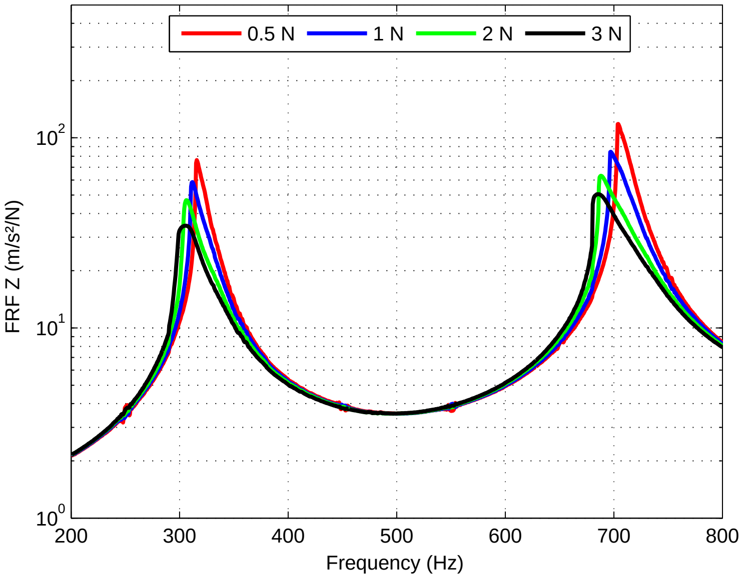

Figure 3.17: FRF for sine sweep excitation with shaker stinger experiment for set of different excitation amplitudes, for a double layered beam with nonlineat contact surfaces (see Test Structure in chapter 5).

3.2.2 Experimental Data Analysis

After successful accomplishment of data acquisition, a modal model can be developed to estimate the resonance frequencies and modal damping ratios. There exists many different mode indicator and parameter identification algorithms. Among different algorithms, main classification is done into a temporal or spatial based algorithms. The temporal algorithms (time/frequency measured data) in the first step estimates the modal frequencies or poles and in the second step it estimates the spatial information like mode shapes for the corresponding modes. The spatial algorithm is a reverse approach of temporal algorithm, where first the mode shapes are estimated and then the modal frequencies [3].

Comparison between different modal identification algorithms is presented in [92, 93]. There has been significant advances in the modal parameter estimations for the OMA, among different techniques the OMAX algorithm is one of the most robust and accurate.

The Transfer Function or FRF from measurements can be expressed into two conventional representations- rational fraction form and partial fraction form. The rational fraction form is a ratio of two polynomials, wherein the order of the numerator and denominator polynomials are independent to each other. The denominator polynomial is the characteristic polynomial, with root of the characteristics equation relating to the poles of the transfer function [96]. Also, the roots of the numerator polynomial relates to zeros of transfer function.

$$H(\omega)=\frac{\sum\limits_{k=0}^{m} a_k(j\omega)^k}{\sum\limits_{k=0}^{n} b_k(j\omega)^k} \tag{3.48}$$

A rational fraction form of FRF is a curve fitted with the measured FRF, such that the locations of poles and zeros of the transfer function can be evaluated for the modal parameter estimation. The curve fitting algorithm finds the unknown coefficients a_k and b_k of the numerator and denominator polynomial respectively, with minimizing the error function. The error calculation is shown in below equation, which is solved later with use of orthogonality property by extending the FRF in negative frequency axis [96].

$$\mathrm{e}_i=\sum_{k=0}^{m} a_k(j\omega)^k-\mathrm{h}_i\left(\sum_{k=0}^{n} b_k(j\omega)^k+(j\omega)^n\right), \tag{3.49}$$

$$J=\sum_{i=1}^{N}\mathrm{e}_i^*\mathrm{e}_i=\mathrm{E}^*\mathrm{E}, \tag{3.50}$$

where, h_i is the measured FRF and J is the squared error. A partial fraction form is a representation of FRF directly in terms of the modal parameters. The numerator contains the pairs of complex conjugate residues and the denominator contains poles, as shown in below equation.

$$H(\omega)=\sum_{k=1}^{N}\frac{R_k}{j\omega-p_k}+\frac{R_k^*}{j\omega-p_k^*}, \tag{3.51}$$

where, R_k is a constant numerator part of FRF, referred as the residue matrix for mode k. Also, p_k is the pole location. This representation of FRF matrix is curve-fitted with measured FRF. However, a direct curve fit algorithm is not possible and hence some numerical techniques for modal parameter estimation are required. The Complex Mode Indicator Function (CMIF) is one of the most famous and used algorithms in commercial software for the EMA measured FRF. A CMIF builds a normal matrix as the Hermitian product of the FRF matrices. Hence, a plot of the eigenvalues of the corresponding matrix on the frequency axis defines the peak locations as the resonance frequency and the peak amplitude as the amount of damping. While the initial approaches were based on the Eigen

Value Decomposition (EVD), further advances in CMIF realize better estimation based on Singular Value Decomposition (SVD) [2], as shown in below equations.

$$(H(\omega))^H(H(\omega)) = V(\omega)[\Lambda(\omega)]V(\omega)^H, \tag{3.52}$$

$$H(\omega) = V(\omega)[\Sigma(\omega)]V(\omega)^H, \tag{3.53}$$

wherein, $(H(\omega))^H$ is the Hermitian matrix of FRF, $\Lambda(\omega)$ is the eigenvalue and $\Sigma(\omega)$ is the singular value. Although the magnitudes of the normal matrix are same in both approaches of EVD and SVD (as $\Lambda(\omega) = \Sigma(\omega)^2$), but the EVD have real valued eigenvector and SVD has complex valued singular vectors. The SVD approach can be described for the imaginary part of FRF, but it is only applicable for the dynamic stiffness or receptance FRF [2]. The CMIF is essentially a spatial domain algorithm [86], with estimation of modal vectors in the first stage and the estimation of the modal frequencies and modal scaling constant in second stage. The terms used in equation (3.51) are further broken down into representations of dynamical quantities to have the understanding for the modal parameters :

$$p_k = -\sigma_d(k) + j\omega_d(k), \tag{3.54}$$

where, σ_d is the damping constant or stability and the ω_d is the damped modal frequency. The modal damping ratio and natural frequency for mode k is calculated based on the damped frequency and stability as,

$$\xi_k = \frac{\sigma_d(k)}{\sqrt{\sigma_d(k)^2 + \omega_d(k)^2}}, \quad \omega_n(k) = \sqrt{\sigma_d(k)^2 + \omega_d(k)^2}. \tag{3.55}$$

The residue matrix is also referred as modal constant matrix. It is the product between the displacement vectors measured at different locations for every frequency step k, as shown in below equation.

$$R_{ijk} = q_k u_{ik} u_{jk}. \tag{3.56}$$

Here q_k is referred as modal scaling constant or the modal participation factor. The modal scaling constant can be evaluated based on the principle of modal superposition and reformulation of the mass matrix in terms of diagonal matrix of modal masses, for each mode represented in the modal co-ordinates.

$$q_k = \frac{1}{2M_k\omega_k} \qquad \text{with } \ (u^T M u)_k = M_k. \tag{3.57}$$

For a measured driving point FRF, assumption of unit modal masses leads to estimation of modal constant as a function of only modal frequencies i.e. $q_k = 1/2\omega_k$.

The curve fitting of the FRF is essentially very efficient for a system experiencing largely distinct separated modes. With modal coupling and closely spaced modes, the curve fitting techniques requires emphasis on the proper identification in the mode pairs in the selected frequency range. The common curve fitting techniques are distinguished into 4 ways- local SDOF, local MDOF, Global fitting and Poly Reference [63]. The EMA prediction for modal parameters is applicable for lightly damped linear system. With systems incorporating high non-linearity, the modal parameters estimation is not proposed with an unique approach. Some of the works done in identifying the non-linearity and its applications on modal analysis have been presented in [18, 121]. The present commercial software's like LMS Test Labs, MEScope VES, PULSE Modal Test etc, are designed to estimate modal parameter with good accuracy. Also, these software have possibility to perform the complexity check on the measured data.

Summary

This chapter discussed the numerical and experimental techniques to describe the vibrational behaviour of structures. The numerical implementation of the structural dynamics is described in both time and frequency domain. Implementation of various numerical techniques for classical Duffing's oscillator is presented to describe the non-linear behaviour of mechanical systems in both time and frequency domain. Later, the implementation of the non-linear constitutive contact laws in vibration equation is done to discuss the limitations of the constitutive equations and their numerical implementation. The time domain representation although has good prediction but requires large computational time, especially when dealing with broad band excitation and large models. The frequency domain implementation using family of harmonic balance methods improves the computational time but are restricted to the periodic excitations and still non-feasible for large models. The numerical convergence is also difficult for both time and frequency domain representations for large and complex structure solved based on a non-linear governing laws. The complexity and disadvantages of non-linear representation motivates to have a new model, which is capable of describing the influence of contact for large and complex structures with improvement in computational time. The chapter also describes the experimental techniques used for measuring and quantifying the vibrational behaviour of structures. These experiment techniques will be used in chapter 5 for making comparison between the experimental and simulation results.

Chapter 4

Non-homogeneous Local Linearized Contact Model

The complexity of modelling a non-linear system, especially for the source of non-linearity from contacts, has been discussed in the preceding chapters. Although the numerical methods provide an advantage of solving the non-linear formulations to considerable accuracy, there exists a demand on the improvement of the convergence rate and computational efficiency. To achieve a balance between modelling the non-linear behaviour and an easy-efficient implementation on large system, this thesis proposes a new methodology of modelling contact interface. The proposed new model is motivated by characterising the contact interface as combination of discrete local linear elements, whose spatially varying contributions lead to a non-homogeneous description on the global level. This chapter describes the new modelling approach in two phases- definitions of the equivalent contact stiffness and contact damping. The contact stiffness definition are based on the work of BITTNER [13], which has been extended with inclusion of the pre-stress deformations for the dynamical excitation like random excitation. The contact damping definition has been developed based on the observation from the numerical investigations. Later, at the end of the chapter, the implementation of the proposed new model in finite element method is discussed.

4.1 Contact Mechanics : Formulations

A brief introduction to the numerical modelling of contact mechanics for continuum bodies is presented in this section. Previous chapter showed some numerical techniques of solving vibration problems with non-linear contact laws, but they have been solved for a *sdof* system. With use of the finite elements, extension to *mdof* system is possible. In the literature, an extensive study on topics of numerical modelling of contacts for finite small and large deformations are dealt by authors like LAURSEN AND SIMO [61], WRIGGERS [122–125], KONYUKHOV AND SCHWEIZERHOF [58], YASTREBOV [126] and many more. A contact between two bodies is defined as the combination of two problems- normal and tangential contact problem. The normal contact problem deals with modelling of penetration behaviour and the tangential contact problem deals with modelling of in-plane relative motion between the bodies. The elastic deformations based on the continuum theory, with infinitesimal small deformation and relative displacement are briefly discussed here.

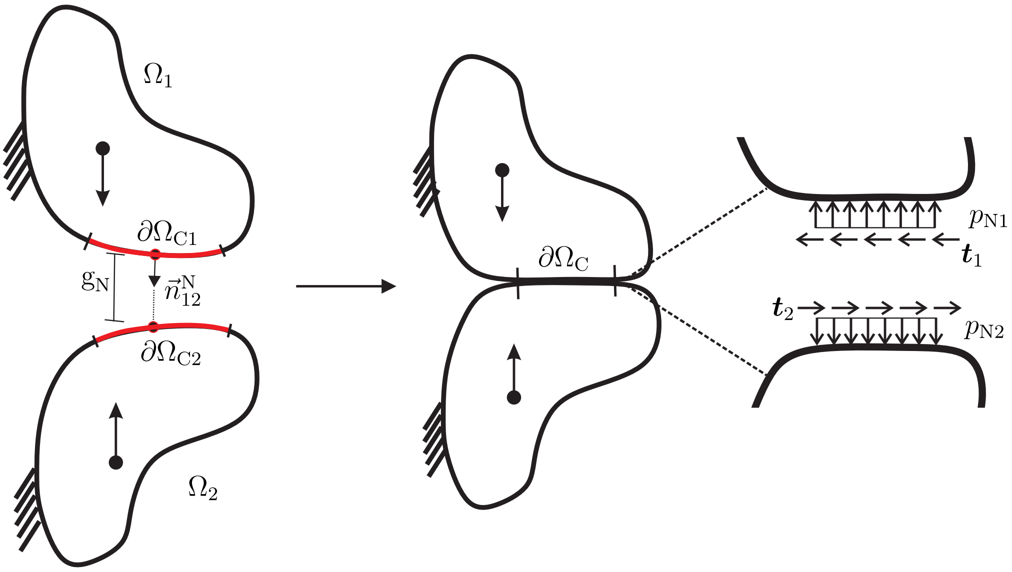

Figure 4.1: Contact between two deformable bodies at $\partial\Omega_C$ based on projection of normal vector from slave to master body with traction field continuity at closed contact status.

A contact between two 3-Dimensional bodies (Ω_1,Ω_2) is characterized by a common boundary ($\partial\Omega_C$) leading to a finite contact area, such that there is a continuity of traction field at the common boundary, see figure 4.1. For two bodies in contact, the contact status is defined based on the non-penetration condition, motivated from the Signorini conditions [126]. A non-penetration condition is similar to calculation of the minimum normal distance between two convex bodies, based on projection method. The normal distance between the bodies is calculated as [124],

$$g_N = \left(\boldsymbol{u}^{(2)} - \boldsymbol{u}^{(1)}\right)\vec{n}^{N}_{12} + g_{N0} \geq 0, \tag{4.1}$$

where, $\boldsymbol{u}^{(i)}$ is the displacement of the i^{th} body with normal vector of $\vec{n}^{N}_{12}$ projected from body 1 to 2. Also, g_{N0} represents the initial gap between the two bodies. The perpendicular to the normal vector gives the tangential vector, required to define the tangential displacement similar to the calculation of a normal gap (4.1). At the contact region, the curvilinear co-ordinate system is used for tracing the curved surfaces using tangential vectors [124].

$$\boldsymbol{g}_T = \left(\boldsymbol{u}^{(2)} - \boldsymbol{u}^{(1)}\right)\vec{n}^{T}_{12} + \boldsymbol{g}_{T0}. \tag{4.2}$$

The continuity of the tractions on the contact surface is idealized with Newtons law of reaction. The traction in the normal direction is related to the contact pressure and in the tangential direction is related to the shear stresses.

$$
\begin{aligned}
p_{\mathrm{N}} &= -p_{\mathrm{N1}} = p_{\mathrm{N2}}. \\
\boldsymbol{t} &= -\boldsymbol{t}_1 = \boldsymbol{t}_2.
\end{aligned}
\tag{4.3}
$$

For no penetration condition, the normal displacement for the normal contact problem is generalized in terms of the inequality condition as $g_{\mathrm{N}} \geq 0$. This can be disintegrated into two forms : closed contact as $g_{\mathrm{N}} = 0$ and open contact as $g_{\mathrm{N}} > 0$. Similarly, for the completely closed contact condition the normal traction (or pressure) is non-zero and for the open contact condition normal traction is equal to zero. Both the conditions on normal displacement and pressure can be combined to formulate the complete normal contact condition, as shown in equation (4.4). This condition for normal contact is similar to the *Kuhn-Tucker* condition in the optimization theory. The optimization problem is associated with the weak form of the elasto-dynamics, where the objective function is to minimize the residuum with constraint conditions as the contact conditions.

$$
\begin{aligned}
&\text{Open contact} && g_{\mathrm{N}} \geq 0 \rightarrow p_{\mathrm{N}} = 0. \\
&\text{Closed contact} && p_{\mathrm{N}} \geq 0 \rightarrow g_{\mathrm{N}} = 0. \\
&\text{Constraint condition} && p_{\mathrm{N}} g_{\mathrm{N}} = 0, \quad \text{with } g_{\mathrm{N}} \geq 0 \text{ and } p_{\mathrm{N}} \geq 0.
\end{aligned}
\tag{4.4}
$$

The generalized discretized weak form of elastodynamics with contacts contribution is presented as,

$$
\begin{aligned}
\int_{\Omega} \delta\hat{\boldsymbol{u}}^T \boldsymbol{N}^T \boldsymbol{N} \rho \ddot{\hat{\boldsymbol{u}}}\ \mathrm{d}\partial\Omega + \int_{\Omega} \delta\hat{\boldsymbol{u}}^T \boldsymbol{D}^T \mathbb{C} \boldsymbol{D} \hat{\boldsymbol{u}}\ \mathrm{d}\Omega \ &= \int_{\partial\Omega} \delta\hat{\boldsymbol{u}}^T \boldsymbol{N}^T \boldsymbol{t}\ \mathrm{d}\partial\Omega + \int_{\partial\Omega_{\mathrm{C}}} \delta\hat{\boldsymbol{g}}^T \boldsymbol{N}^T \boldsymbol{t} \mathrm{d}\partial\Omega_{\mathrm{C}} \\
&+ \int_{\Omega} \delta\hat{\boldsymbol{u}}^T \boldsymbol{N}^T \rho \boldsymbol{b}\ \mathrm{d}\Omega.
\end{aligned}
\tag{4.5}
$$

As mentioned earlier, the weak form of elastodynamics represents an optimization problem, which can be solved using the conventional techniques like Penalty method, Lagrange multipliers method and Augmented Lagrangian method. A virtual stiffness like a penalty term is added in the Penalty method, to allow penetration of contact surface. Due to an additional stiffness in the system, the functional tends to be smooth and no additional constraint equations are required. But the choice of the penalty term is however based on trial and error, as small values lead to large penetration and large values lead to ill-condition of global matrix [55, 124, 126]. A Lagrange multiplier method includes an extra reaction force constraint condition, such that the search for a minimum point is transformed to solving for the saddle points. Due to the additional constraint, the size of problem is increased and has a non-smooth behaviour, but the solution obtained is exact [81, 103]. An Augmented Lagrange method is a combination of both Penalty and Lagrange multiplier method, having the advantages of both methods to obtain the exact solution with smooth functional behaviour. However, the method still experience disadvantage of the increased size of the problem with increased computational efforts in implementation [101]. Other advanced algorithms and techniques too have been developed on foundations of above mentioned methods [124], to enhance the convergence and stability.

The FEM implementation is accomplished with discretizing the domain using the conventional 3D shape functions, while the contact regions require special discretization. Among different discretization techniques, the main methods are : node-to-node, node to surface and surface to surface contact discretization. While node to node discretization is one of the simplest method, it allows only small deformations and requires conformed meshes for the master and slave surfaces. The surface-to-surface contact discretization allows large deformation with modelling being independent from the mesh conformity. However, the contact pressure is constant over one segment region and the implementation of the elements are quite complicated in comparison to node-to-node coupling. Mortar discretization techniques have been advantageous to handle non-conforming meshes. Use of zero thickness elements have been used for modelling the linear and non-linear contact stiffness for both transient or frequency domain analysis [11, 39, 40, 67].

The constitutive laws for the normal and tangential contact laws have been discussed in previous chapters 2 and 3. An elastic contact problem with no friction condition is solved based on the *Kuhn-Tucker* normal contact conditions. The conventional constitutive law for frictional contact problem used in most of the commercial software is the Coulomb friction model. The contact status is defined into two stages of stick or slip, based on the Coulomb limiting friction values. The description of the states with its corresponding constitutive modelling is shown in equation (4.6). The Newton Raphson method experience convergence issues for the change in contact status from stick to slip and vice-versa. For a better stability, the radial return mapping algorithm in analogy to modelling of elasto-plasticity is used [67, 102, 124, 128].

$$\begin{array}{lll} \text{Stick} : |\boldsymbol{t}| < \mu p_{\mathrm{N}}, & \dfrac{\partial \Delta \boldsymbol{t}}{\partial \Delta \boldsymbol{g}_{\mathrm{T}}} = k_{\varepsilon} \mathbb{I}, & \dfrac{\partial \Delta \boldsymbol{t}}{\partial \Delta g_{\mathrm{N}}} = 0, \\ \text{Slip} : |\boldsymbol{t}| \geq \mu p_{\mathrm{N}}, & \dfrac{\partial \Delta \boldsymbol{t}}{\partial \Delta \boldsymbol{g}_{\mathrm{T}}} = k_{\varepsilon} \left[\mathbb{I} - \dfrac{\boldsymbol{t}}{|\boldsymbol{t}|} \otimes \dfrac{\boldsymbol{t}}{|\boldsymbol{t}|} \right], & \dfrac{\partial \Delta \boldsymbol{t}}{\partial \Delta g_{\mathrm{N}}} = \mu \dfrac{\partial p_{\mathrm{N}}}{\partial g_{\mathrm{N}}} \dfrac{\boldsymbol{t}}{|\boldsymbol{t}|}, \end{array} \tag{4.6}$$

where, k_{ε} is the virtual penalty stiffness.

The modelling of contacts based on the continuum laws are presently being used for industrial applications with arguably good accuracy. However, the implementation and usage for the complex system under dynamic excitation still remain a challenge with the present modelling approaches. For large system with moderate non-linearity through the contacts, emphasis is to have a model which can sufficiently capture the predominant non-linear behaviour. Also, it should be easy to implement and computationally time efficient than present techniques.

4.2 Pressure Dependent Joint

An essential part of dynamic modelling is the determination of the contact stiffness. The contact traction boundary condition in the weak form defines a consistent tangent operator based on the contact forces and relative displacements. A generalized full contact stiffness matrix (or consistent tangent) is obtained as the gradient of the contact forces or stresses in normal and tangential directions, as shown below in equation (4.7). The stiffness matrix is un-symmetric, as there is a coupling between the normal and tangential components.

$$\boldsymbol{K} = \frac{\partial \boldsymbol{F}}{\partial \boldsymbol{\delta}} = \begin{bmatrix} \dfrac{\partial F_{\mathrm{N}}}{\partial \delta_{\mathrm{N}}} & \dfrac{\partial F_{\mathrm{N}}}{\partial \boldsymbol{\delta}_{\mathrm{T}}} \\ \dfrac{\partial \boldsymbol{F}_{\mathrm{T}}}{\partial \delta_{\mathrm{N}}} & \dfrac{\partial \boldsymbol{F}_{\mathrm{T}}}{\partial \boldsymbol{\delta}_{\mathrm{T}}} \end{bmatrix}. \tag{4.7}$$

The contacts initiated by external normal loading leads to the initiation of both the normal and tangential contact. However, for the quasi-static normal loadings (typical example of bolted joints to fasten two bodies), the contact behaviour is dominated by large normal displacements in comparison to negligible tangential relative displacements. Hence for the normal contact problems, the normal contact stiffness prediction is of more importance than the tangential contact stiffness. The normal contact problem defines the relationship between the contact pressure and the interface deformation. The stiffness definition based on these two governing parameters is termed as Pressure Dependent Joint (PDJ) by BITTNER [13], which describes the state and contribution of the contact based on the existing pressure at the interface.

A Pressure Dependent Joint (PDJ) forms the basic building step for the dynamical simulation by providing the contact stiffness to the following modal superposition analysis. The random analysis is only possible (in present commercial software) through performing a modal superposition analysis. Hence, the linear system of equations must have diagonal symmetric dynamic stiffness matrix. The conventional contact models have unsymmetric stiffness matrix and a non-linear definition based on the constitutive friction laws. This is not possible to be solved by modal-superposition principles for structures undergoing random noise excitations. This can only be solved using full transient analysis, which are not feasible due to high computational time. The PDJ model for the normal contact problem transforms the contact stiffness matrix to a diagonal symmetric matrix by de-coupling the normal and tangential components, see equation below.

$$\boldsymbol{K} = \begin{bmatrix} \dfrac{\partial F_{\mathrm{N}}}{\partial \delta_{\mathrm{N}}} & 0 \\ 0 & \dfrac{\partial \boldsymbol{F}_{\mathrm{T}}}{\partial \boldsymbol{\delta}_{\mathrm{T}}} \end{bmatrix} = \begin{bmatrix} K_{\mathrm{N}} & 0 \\ 0 & \boldsymbol{K}_{\mathrm{T}} \end{bmatrix}. \tag{4.8}$$

The argument of decoupling is proposed by Pande and Sharma [80], Desai et.al [33] and Sharma and Desai [99] for modelling the joint interface with very thin layers, such that the admissible choice of zero poisson's ratio leads to zero in-plane stresses [68]. The following discussion in this section explains the creation of the PDJ element and derivation of the contact stiffness for the normal and tangential directions.

4.2.1 Element Creation

The creation of PDJ elements to accommodate the de-coupled contribution for the normal and tangential stiffness is discussed here. The PDJ element is implemented in Ansys v14 software [13]. The element has the possibilities of incorporating both the linear and non-linear constitutive normal contact laws. The conventional surface-to-surface contact elements in commercial software do not provide the possibility of performing a non-linear static analysis followed by modal superimposed steady state or random analysis. On contrary for the PDJ element, the use of discrete spring elements enables better controllability to modify the stiffness behaviour and to perform the modal superposition frequency analysis. The PDJ element creation is a four step process, as shown in figure 4.2.

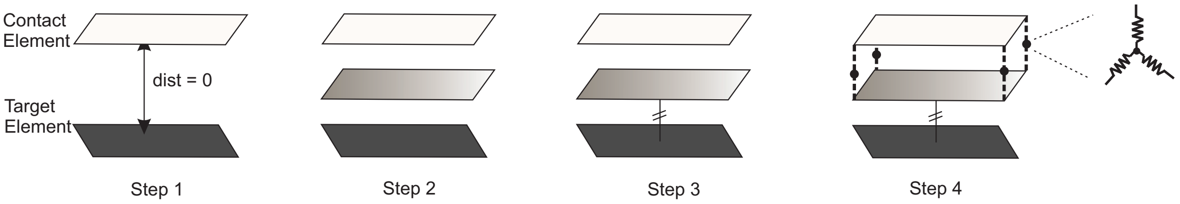

Figure 4.2: Steps in creation of Pressure Dependent Joint (PDJ) element between contact and target faces of surfaces in contact

In the first step, the two bodies in contact are meshed and the mating surfaces are discretized with regular contact and target finite elements. The conventional choice of the contact surface is the softer material with high mesh density. Due to different geometrical constraints on the individual structures of an assembled structure, the non-conforming meshes tend to be unavoidable. In the second step, the effect of non-conforming mesh is resolved by forming a new target element. The new target element is created between the contact and old target element, whose orientation is same as that of the contact element. This leads to a conformed mesh between the contact and target element. In third step, a constraint equation between new and old target elements is created. This enables a fixed bonded contact between the two elements. In other words, the displacement results of the new target element nodes will be transferred directly to the old target element nodes. In the final step, three dimensional Kelvin-Voigt spring elements are inserted between the nodes of the contact and new target elements.

Ansys v14 has been used, wherein the surface-to-surface based contact definition from software is replaced with PDJ elements. The first step of creating conventional contact and target elements refer to CONTA174 and TARGE170 elements in Ansys element library [6]. The constraints between the new and old target elements in the step 3 is performed using a Multi-Point-Constraint (MPC) contact algorithm, almost like a completely bonded joint. The Kelvin-Voigt elements are characterized by use of discrete spring elements-COMBIN14 and COMBIN39, where the former allows only linear behaviour and latter allows a non-linear behaviour of the spring stiffness [6]. These elements are used for the point to point coupling between the nodes of the contact and the new target element. Using these discrete spring elements, the de-coupled stiffness corresponding to the normal and tangential contact stiffness can be independently assigned. The derivation of the normal and tangential contact stiffness is explained in the following section.

4.2.2 Contact Stiffness

Normal Contact

The normal contact stiffness for a rough surface can be determined based on the constitutive laws of HERTZ - CEB model, GREENWOOD AND WILLIAMSON and others, as covered in the chapter 2. The GREENWOOD AND WILLIAMSON model based on the statistical fit of the surface roughness with choice of exponential distribution of peaks does give a constructive relation between the normal loading and the deformation of the surface at meso-scales. The modified exponential distribution (see equation (2.11)) which fits the Gaussian distribution much better, is used to formulate a relation between the contact pressure and the deformation in terms of penetration. The exponential pressure-penetration law is presented in below equation [13, 67].

$$P_{\mathrm{N}} = P_{\mathrm{N0}}\, e^{\lambda(\delta_{\mathrm{N}}-\delta_{\mathrm{N0}})}, \qquad \lambda \simeq \frac{1}{\sigma_{\mathrm{r}}}. \tag{4.9}$$

In above equation, the contact parameter λ governing the curvature of the exponential curve is idealized as the inverse of the standard deviation (σ_{r}) of the surface roughness. Each local nodal point in contact will be governed through this exponential pressure-penetration for the normal contact description. Also, the normal contact parameter λ is chosen as constant for all local points. The exponential pressure-penetration relation involves two constants P_{N0} and δ_{N0}, as shown in above equation (4.9). P_{N0} refers to the initial contact pressure, when the two surfaces in contact are experiencing no external loading. This initial pressure cannot be zero, as this leads to a non-physical description of zero pressure for any or every value of the normal penetration. δ_{N0} is the distance between the reference planes of two rough surfaces in contact or idealized as the maximum peak height from the reference plane of the rough surface. The initial penetration δ_{N0}, in general understanding can also be related to the penetration experienced at zero contact pressure. δ_{N0} is approximately calculated by extending the pressure-penetration curve backwards with unit slope to meet the negative penetration axis, see figure 4.3(b).

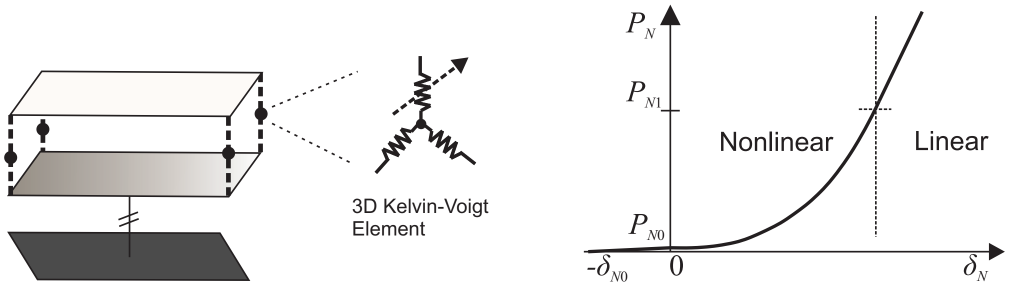

(a) PDJ element with non-linear normal and linear tangential springs elements.

(b) Exponential law between the contact pressure and penetration.

Figure 4.3: (a) Pictorial representation of PDJ element based on point-to-point coupling of contact and target surfaces using Kelvin-Voigt elements. (b) The governing normal contact law based on exponential relation between pressure-penetration.

A schematic representation of the use of the PDJ element with normal spring having the non-linear force-deflection behaviour based on the pressure-penetration law is shown in the figure 4.3. With use of pressure-penetration relation, the local contact stiffness can be defined for each contact pair using discrete PDJ elements. Due to the unbounded behaviour of the exponential function, very large magnitudes of pressure are required to produce very small deformation after certain saturation deformation limit. This leads to problems of numerical convergence. This problem is handled by performing a transition from non-linear to linear behaviour for higher pressure values. The pressure at the transition phase is referred to as saturation pressure P_{N1} and the pictorial representation of non-linear and linear regions is depicted in figure 4.3(b). The region before the saturation pressure uses the proposed exponential pressure-penetration formulation and the region after the saturation pressure uses a constant slope with a linear relation between pressure and penetration. This argument is supported by the CEB model, wherein the non-linear behaviour is transformed to linear behaviour for higher loading, see equation (2.8). The slope being equivalent to the normal contact stiffness here, is calculated based on the product of the curvature parameter and the saturation pressure. Figure 4.4(a) shows the two choices of the pressure-penetration and modified pressure-penetration curve.

The stiffness density K_{N} is calculated as the derivative of the pressure with respective to penetration. There exists a linear relation between the stiffness density and pressure with slope value equal to curvature parameter λ. However, as the pressure-penetration formulation is modified into regions of non-linear and linear, the stiffness density exhibits two states of linear and constant stiffness. The value of stiffness above and below the saturation pressure is obtained as,

$$K_{\mathrm{N}} = \frac{dP_{\mathrm{N}}}{d\delta_{\mathrm{N}}} = \begin{cases} \lambda P_{\mathrm{N}} & P_{\mathrm{N}} \leq P_{\mathrm{N1}}. \\ \\ \lambda P_{\mathrm{N1}} & P_{\mathrm{N}} > P_{\mathrm{N1}}. \end{cases} \tag{4.10}$$

Although the pressure-penetration relation is reduced to a formulation with non-linear and linear transition to accommodate better convergence, the calculation of stiffness leads to a switch function based on the pressure values. Hence, it leads to the discontinuity at transition point. This is similar to Coulomb law with stick-slip behaviour, based on the limiting friction value, which often leads to convergence issues due to an abrupt change in contact status. A Hyperbolic fit function can be used to have a smooth transition of the stiffness variation with respect to the pressure increments, as shown in equation (4.11). This particular fit function forms a good explicit single formulation, with a choice for the constant $c_\mathrm{k} = 0.85$ controlling the smooth transition.

$$K_\mathrm{N} = \lambda P_\mathrm{N1} \tanh\left(c_\mathrm{k} \frac{P_\mathrm{N}}{P_\mathrm{N1}} \right). \tag{4.11}$$

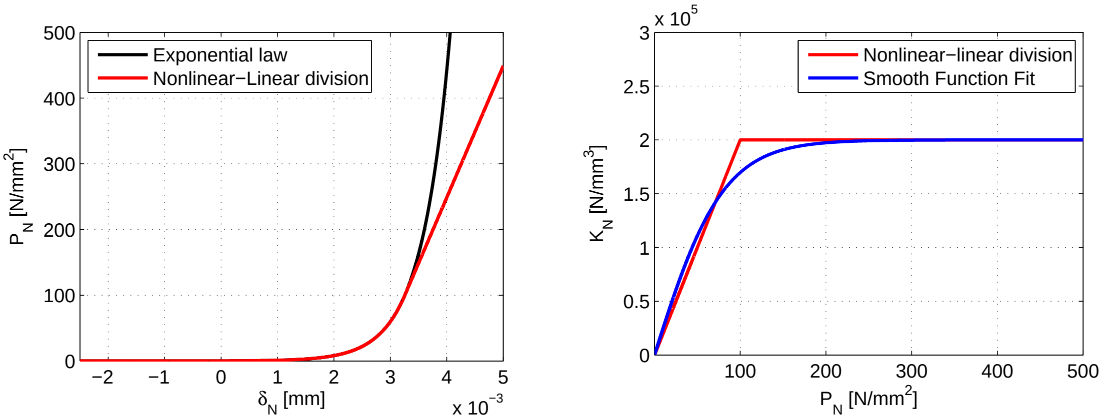

(a) Modified pressure-penetration relation. (b) Contact stiffness vs. Pressure.

Figure 4.4: Modification in exponential pressure-penetration with non-linear and linear division based on saturation pressure $P_\mathrm{N1} = 100\mathrm{N/mm^2}$ (left). The stiffness with discontinuity at saturation pressure for modified exponential pressure-penetration law and used hyperbolic fit function to smoothen the transition phase.

Figure 4.4(b) shows the smooth transition of stiffness at the saturation pressure. The stiffness density is directly related to the normal contact stiffness density. The contact stiffness density is hence dependent on the curvature parameter λ and saturation pressure parameter P_N1.

Tangential Contact

For the quasi-static loading in normal direction, the normal displacement is higher in magnitude in comparison to the tangential displacement. The previous section explaining the derivation of the normal contact stiffness based on the pressure distribution is sufficient to capture the non-linearity due to the normal loading. The tangential contact stiffness can then be directly calculated as the product of the coupling factor and the normal stiffness [13, 67], as previously discussed in the equation (2.23).

$$K_{\mathrm{T0}} = \beta_0 K_{\mathrm{N}}, \qquad \text{with} \quad \beta_0 = \frac{4G^*}{E^*}. \tag{4.12}$$

The coupling factor β_0 is based on the composite shear (G^*) and elastic modulus (E^*) of materials in contact, see equation (4.12). Equation (4.12) provides an easy way for calculating the tangential stiffness based on normal stiffness. For increase in amplitude of steady state tangential loading, equivalent reduction in tangential stiffness can be achieved by varying the coupling factor. For modal superposition transient analysis, the non-linear tangential behaviour can be accommodated by use of *Elasto-Gleit* model [70], with friction slider governing stick-slip states. For modal superposition random analysis, the initial contact stiffness is sufficient to define the steady state behaviour for the tangential contact. To extend the scope of PDJ in modelling contact interfaces with dissipative terms too, definition of contact damping is required. The following section will describe the formulation of the damping estimation based on some numerical investigations.

4.3 Dissipation Distribution over Interface

The previous section discussed about the normal and tangential contact stiffness definition based on the pressure distribution. The contact damping is required to be estimated in conjecture with contact stiffness, to have the complete contribution of contacts to describe the global vibrational behaviour of a structure. To have an understanding about the contact damping, this section tries to solve a full non-linear transient domain analysis-to study the trends and profiles of the dissipation loss occurring at different locations in the contact zone. The motivation to perform this analysis is to study shape of profile of the contact dissipation at contact interface and build an explicit formulation to describe the contact damping distribution. The section presents set of qualitative numerical investigations on few simplified examples of beam structure. The governing dynamic contact law used is the modified Dahl bristle model, as discussed in chapter 2.

4.3.1 Solid 3D Beam- Effect of contact pressure

For the first numerical investigation, an example of solid 3D continuum beam model with a bolted joint at one end is taken. Figure 4.5 shows the numerical model to be used for performing the transient non-linear contact analysis. The mass and stiffness matrices for the solid-tetra/hexa elements are shown in appendix A. At first, the static analysis of the bolt loading is done based on the formulations presented in previous section on Pressure Dependent Joint.

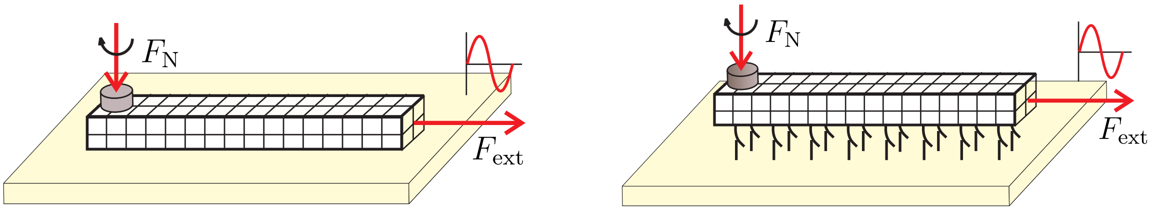

(a) 3D solid beam with bolted joint.

(b) Dahl brush element at contact interface.

Figure 4.5: Set-up of a bolted end 3D solid continuum beam model having contact with a rigid surface, wherein the contact interface is modelled using modified Dahl formulation. Harmonic excitation is applied at opposite end of bolted joint.

An equivalent axial force (F_bv) for the bolt twisting moment is calculated based on the twisting moment (M_b), dimensions of the bolt and coefficient of friction [10, 73] as,

$$F_\mathrm{bv} = \frac{M_\mathrm{b}}{(0.6\mu_\mathrm{bolt} d_\mathrm{nom}) + (0.5\mu_\mathrm{head} d_\mathrm{head})}. \tag{4.13}$$

Here, d_nom is the nominal diameter of the bolt shaft, d_head is the average diameter of the bolt head, μ_bolt is the friction coefficient for bolt shaft and μ_head is the friction coefficient under bolt head. Here value of $\mu_\mathrm{bolt}, \mu_\mathrm{head} = 0.3$ is used. The static analysis results gives the contact pressure over the contact interface, which is used to calculate the limiting friction force value for the tangential forces. The contact surface between the beam and the rigid surface is re-defined with modified Dahl spring elements, wherein the initial contact stiffness is calculated based on the gradient of the contact pressure, see section 4.2. A sinusoidal harmonic excitation is applied at the free end of the beam while the other end (bolt position) is modelled as fixed boundary condition. The excitation frequency is chosen as the modal frequency of the longitudinal mode, such that the maximum relative motion between the beam and rigid surface can be achieved.

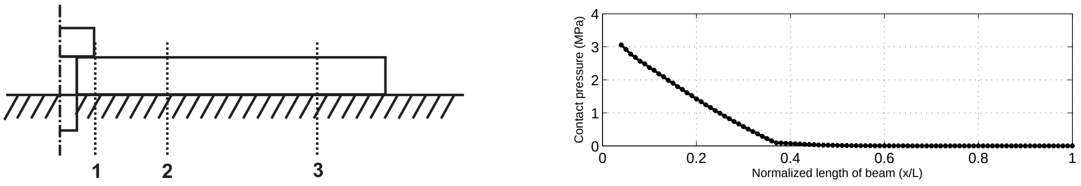

(a) Positions on beam.

(b) Contact pressure over beam length.

Figure 4.6: Different positions chosen over beam length based on the contact pressure distribution over beam length for bolting torque of 1 Nm.

The region near the bolt has the maximum normal contact force and the region near the excitation point has negligible normal contact force. Figure 4.6(a) shows selection of three points according to their distance from the bolt center. Figure 4.6(b) shows the

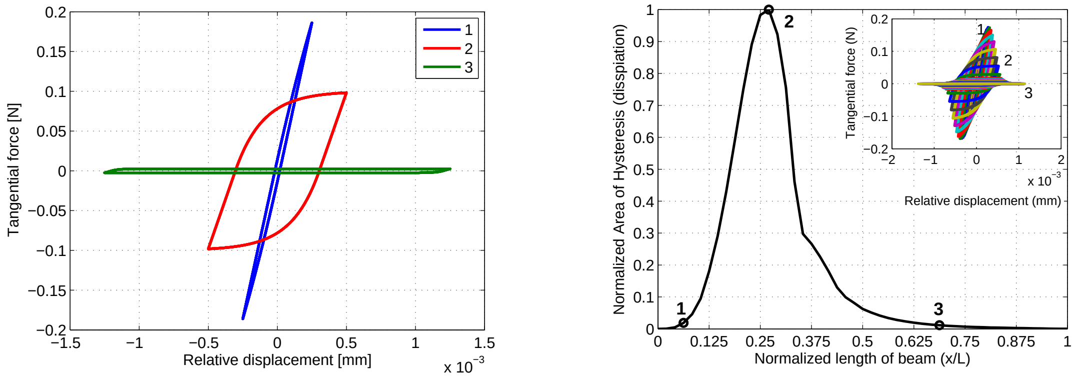

(a) Tangential force vs. relative displacement for various points at contact interface.

(b) Normalized dissipation vs. location at the contact interface over beam length.

Figure 4.7: Hysteresis shapes at the different local nodal points of the contact interface (left). The normalized dissipation loss due to contacts over the length of beam (right).

pressure distribution over the interface length. This leads to the maximum relative displacements at regions away from the bolt (near excitation point) and minimum relative displacements at regions near the bolt. The hysteresis shapes and the corresponding area of hysteresis at each local nodal point on the contact interface are shown in figure 4.7. The maximum dissipation is observed at the position 2 over the beam length . It is interesting to see that the area of the hysteresis is maximum at location which is neither very close to the bolt nor very far from the bolt. This observation is in conjecture with observations of Groper [46], wherein it is established that maximum energy is dissipated when magnitude of slip occurs at border of partial slip and full slip. The observations of this numerical investigation will be used later in defining the zones of the contact interface based on the contact dissipation value and hysteresis shape.

4.3.2 Euler Beam- Effect of bolt torque

Further example of the numerical investigations are extended with use of Euler beam theory modelled using 3-dof beam elements. The corresponding shape function and beam element mass-stiffness matrices are presented in Appendix A. A beam structure fastened to a rigid surface with a bolt at the middle of the beam length is used. The system has a symmetric pressure distribution with respect to the bolt center. Figure 4.8 shows the finite element model of the beam structure. Three choices of the bolting torque- 1 Nm, 3 Nm and 5 Nm are used. The corresponding normal forces calculated based on equation (4.13) are 800 N, 2400 N and 4000 N respectively.

Similar to the previous solid 3D element example, the PDJ model is used to obtain the contact pressure distribution based on individual choices of bolt loads. The Coulomb friction limit (friction coefficient $\mu = 0.3$) and the contact stiffness is calculated from the

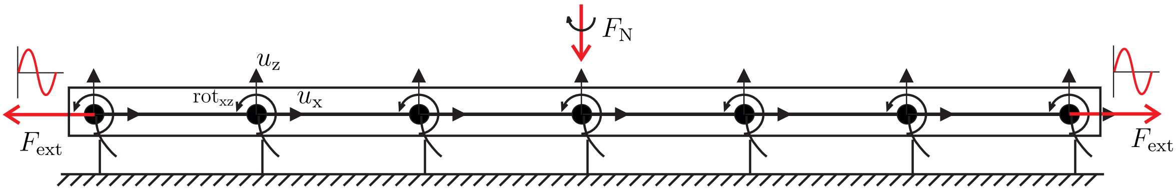

Figure 4.8: Euler beam element with 3-dof having bolt load at the middle of the beam and harmonic excitation applied at free ends in opposite directions.

pressure distribution. The rotational dof of the beam element is coupled to the contact spring element, with rotational stiffness calculated as the product of the normal stiffness and the half of the beam thickness [38]. The nodes associated to bolt center are fixed and the two ends of the beam are excited sinusoidally in the opposite direction.

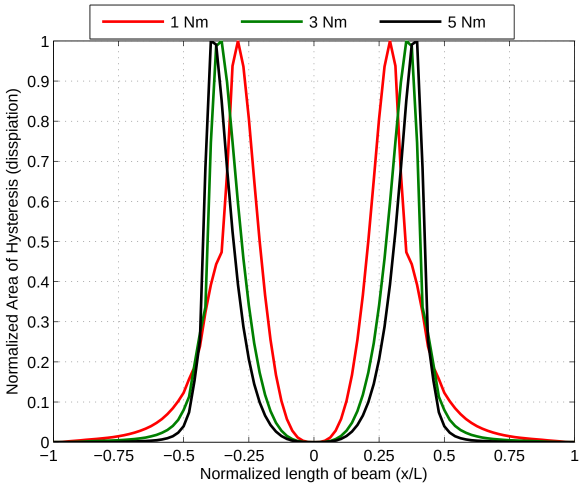

Figure 4.9: Effect of the bolt load on the dissipation profile over the contact interface length.

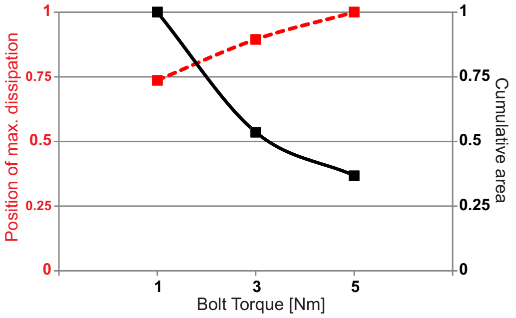

Figure 4.10: Effect of the bolt load on the position of the maximum dissipation and the cumulative dissipation.

Figure 4.9 shows the normalized area of hysteresis or dissipation over the normalized length of the beam for 1 Nm, 3 Nm and 5 Nm bolting torques. The important observation is to see the shifting of the maximum dissipation location with respect to increasing bolt load. As the bolt load increases, the position of the maximum dissipation over contact interface length shifts away from the bolt center. Also, with higher normal bolt loading (for 3 Nm and 5 Nm), the position of maximum dissipation is approximately the same and is assumed to stabilize with further higher loads. The effect of bolt load is summarized in figure 4.10. It is concluded that with increase in bolt load, the cumulative losses decreases and the position of maximum dissipation shifts away from bolt center.

4.3.3 Double Rod- Effect of excitation

The numerical investigations associated to the beam model had two important observations : the dissipation is maximum at some optimum intermediate location from the bolt center and the position of maximum dissipation shifts with respect to variation in the contact pressure distribution. These numerical investigations were done with a constant amplitude of the harmonic excitation. But as discussed in the previous chapter on structural dynamics, the increase in the excitation amplitudes leads to the increase in the non-linear behaviour of the systems having contact interface non-linearity [see non-linear FRF shapes in figures 3.13 and 3.17, chapter 3]. Hence, it is recommended to extended the numerical investigation for studying the influence on the dissipation trend due to the excitation amplitude. A double rod structure fastened at one end using a bolt is used for the numerical investigation, see figure 4.11. As the contact dissipation is essentially observed for two surface experiencing the in-plane relative motion between each other, the 1 dof rod element with translation dof is justified to be used for numerical modelling and investigation for dissipation trend.

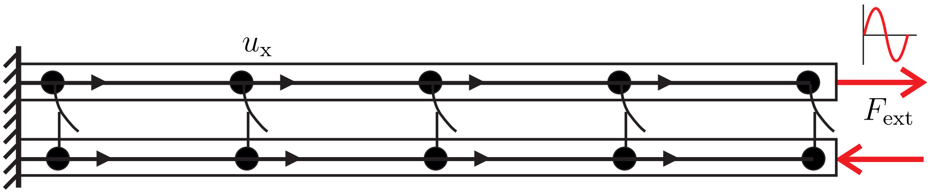

Figure 4.11: Double rod structure set-up with fixed ends. The harmonic excitations applied in opposite directions for each rod at the free end.

The pressure distribution obtained in the previous beam example for 1 Nm bolting torque (800 N) is used to calculate the coulomb limit of friction. Three choices of the harmonics excitation amplitude are taken : 1 N, 10 N and 100 N. The excitation is applied at the free end of the two rods in contact, but in the opposite directions as shown in figure 4.11. This results in the maximum possibility of relative displacement between the two rods. The bolt center is treated as the fixed end, depicting a model of cantilever double layered beam. It is clear from the set-up, that the maximum relative displacements will be near the excitation point and the maximum Coulomb limiting friction is at the fixed end.

Figure 4.12 shows the contact dissipation results associated with 1 N, 10 N and 100 N of excitation amplitudes. The figure show the dissipation trend and the corresponding hysteresis at the nodal points over the contact interface length. The hysteresis shapes and

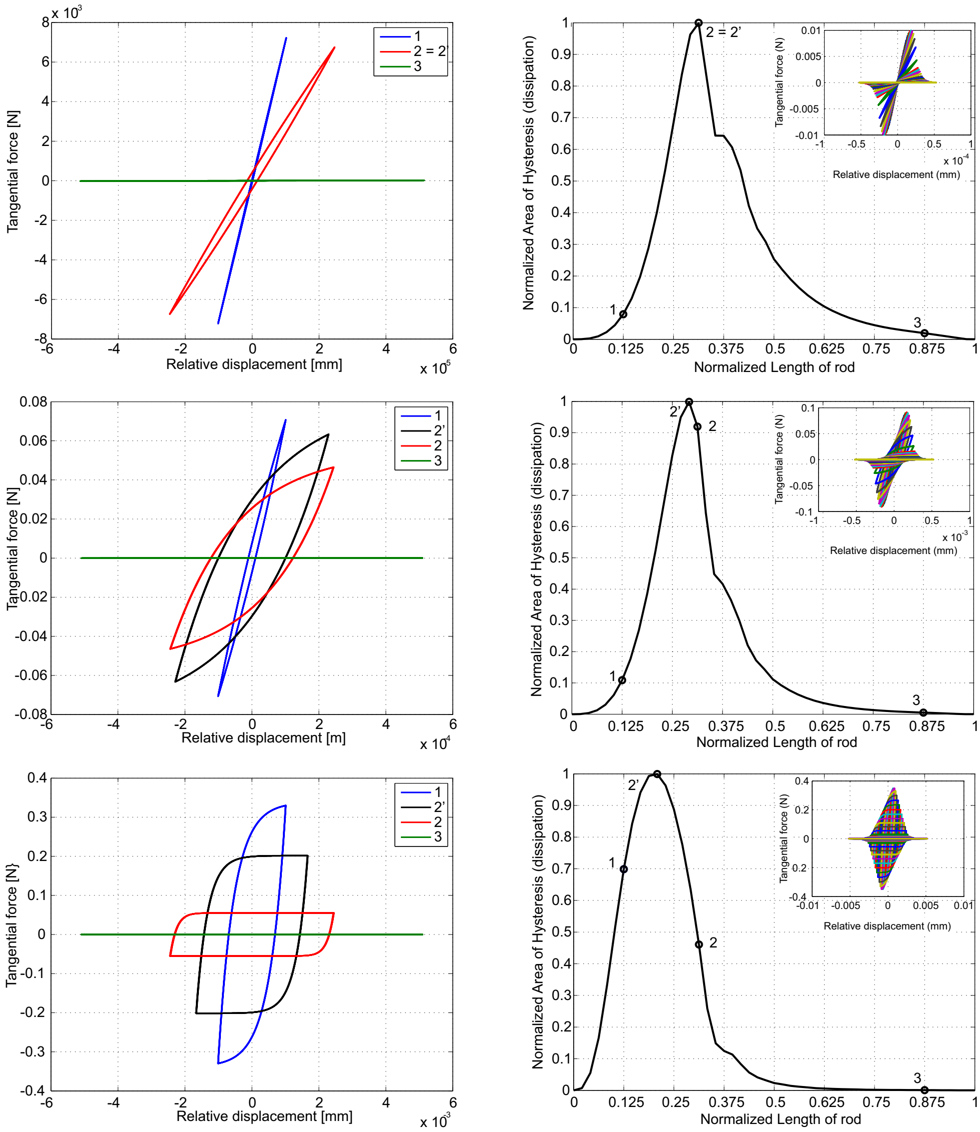

Figure 4.12: Hysteresis shapes at the different local points of the contact interface (left). The hysteresis loss over the interface length for 1 N, 10 N and 100 N of excitation amplitudes (right).

area for both upper and lower rods are equal. The main observation from the previous beam problem investigations, i.e. the maximum dissipation is at an intermediate location over contact interface length, is also obtained here (for all excitation amplitudes). Also, with increase in the excitation amplitude, the area of the hysteresis is also increased, similar to experimental observation by Gaul and Lenz [36, 64].

The hysteresis shape related to 1 N excitation amplitude associates to Mindlin shape, at almost all nodes of the contact interface. The 10 N excitation amplitude transforms the hysteresis such that the nodes near the bolt center resemble thin Mindlin shape, nodes away from bolt center resemble Coulomb hysteresis and intermediate nodes resemble combination of both Mindlin and Coulomb hysteresis shapes. With higher excitation amplitude of 100N, the large part of the contact interface experience Coulomb hysteresis,

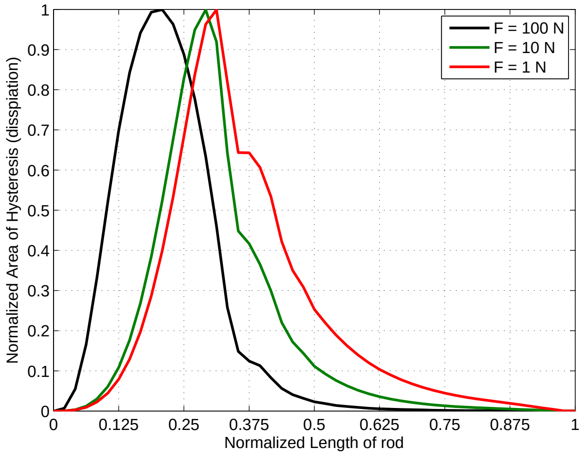

Figure 4.13: Effect on the dissipation profile over contact interface length with respect to the variation in the excitation amplitudes.

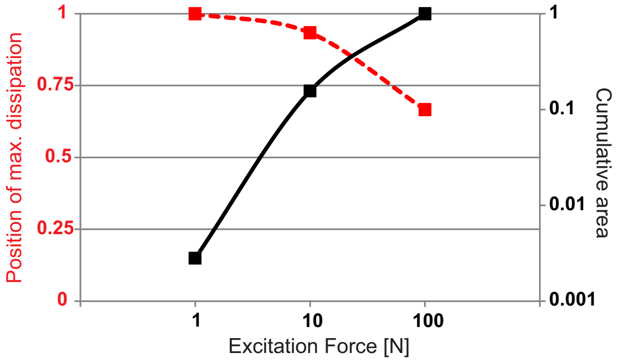

Figure 4.14: Effect of the excitation amplitude on the position of the maximum dissipation and the cumulative dissipation.

related to complete sliding. Figure 4.13 shows the dissipation trend over the normalized length of the beam for all three excitation amplitude in one plot. For large excitation amplitude of 100 N, the dissipation curve has large width (broad) in comparison to 1 N and 10 N excitation amplitudes. The other important observation is the shifting behaviour of the position of the maximum dissipation with respect to the variation in the excitation amplitude. With increasing excitation amplitude, the position of the maximum dissipation shifts towards the bolt center. This is also a valid result which is explained as follows. With increase in the excitation amplitude, every local contact pair experiences increase in the relative displacement. This leads to both increase in the hysteresis area and change in the hysteresis shape. This leads to a new local point near bolt center which has optimal pressure and relative displacement to give maximum dissipation. The influence of excitation amplitude on the shifting behaviour and cumulative area of hysteresis is summarized in the figure 4.14, wherein with increase in excitation amplitude- the cumulative dissipation increases and the position of maximum dissipation shifts near the bolt center.

A very important observation to be visualized is the shape of the dissipation curve over the contact interface length, for all cases of numerical investigations. The dissipation profile for all cases start from zero, attains maximum value and then tends to zero, see figures 4.7, 4.9 and 4.13. This suggests that the dissipation profile can be captured using classical statistical distribution functions. The shifting of maximum dissipation location can also be controlled using the statistical parameters like mean and standard deviation. The observations from the numerical investigation of dissipation trend and shape over the contact interface lays the foundation for the defining of damping, discussed in following section.

4.4 Damped Pressure Dependent Joint

From the results presented in the previous section- generalizations for the dissipations trend can be obtained for bolted joints. The dissipation losses are directly associated with the damping, and a similar trend of the damping over the contact area can be assumed. The contact stiffness based on the gradient of the pressure with respect to the penetration and the local damping based on the local dissipation trend over interface length together defines the model as Damped-Pressure Dependent Joint (D-PDJ). This is essentially the combination of PDJ and non-homogeneous continuous damping distribution. This section explains the formulations for the damping definition with the required parameters and modifications for the implementation of D-PDJ model in commercial software, like Ansys v14.

4.4.1 Contact Damping- Statistical distribution

The following conclusions are generalized from the numerical investigations for the beam structure, with non-uniform pressure distribution over the interface length.

- The maximum dissipation occurs at a region in between the high and low bonding pressure.
- The shape of the dissipation curve over the interface length resembles a continuous probability distribution formulation, like the Weibull distribution.
- With increase in the bonding pressure, the amount of dissipation reduces and the maximum dissipation location shifts away from the bolt center.
- With increase in the amplitude of excitation, the amount of dissipation increases and the maximum dissipation location shifts towards the bolt center.

The first observation is of prime interest in defining the zones of the contact region, with respect to the amount of dissipation existing at interface. Second conclusion is an important foundation in formulation of an explicit description of the damping. Third and fourth conclusions motivates the definition of the parameters in the formulation of the contact damping.

The region of contact interface is divided into three regions, based on the corresponding value of dissipation existing in the region. The example of beam structure with a bolted joint at center is recalled for defining the regions. The region near the bolt center experiences a high contact pressure and less magnitude of relative motion. The dissipation value in this region is low and is referred as the region of stick. The region significantly away from bolt center experiences low or zero contact pressure and high magnitude of the relative displacement. The dissipation value in this region too is low and is referred as the region of sliding. The region in between the stick and sliding, experiences intermediate magnitudes of contact pressure and relative displacement but exists large values of dissipation, is referred as region of micro-slip. The hysteresis shape in region of stick are either only linear or thin Mindlin shape, associated with purely elastic behaviour. The region of sliding has purely Coulomb hysteresis shape. The region of micro-slip is essentially the combinations of Mindlin and Coulomb hysteresis shape, associated to region experiencing the stick, transition and slip states. Figure 4.15 shows the division of the three regions of stick, micro-slip and slide in a pictorial form. Figure 4.15 depicts the contact pressure distribution and idealized damping profile, having less values of damping in region of stick and slide and large values of damping in region of micro-slip.

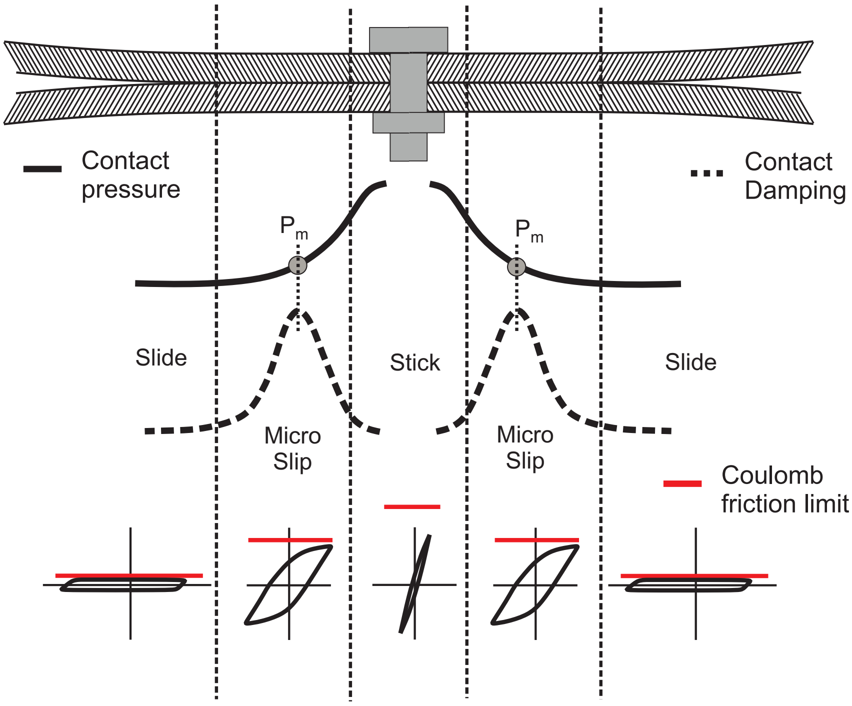

Figure 4.15: Representation of D-PDJ with division of regions based on the amount of the damping.

Although the regions are divided, however required is also the definition of the damping associated with these three regions. An initial approach that can be assumed is to have three different values of the damping for each corresponding region. For example micro-slip region having highest damping say d_{ms} and other two regions having damping d_{st} and d_{sl} for stick and slide regions respectively, with condition $d_{\mathrm{st}} < d_{\mathrm{ms}} > d_{\mathrm{sl}}$. Although the implementation of this approach is easy, but it does not comply with the physical phenomenon. At first, this type of definition leads to jump in values of damping while shifting from one region to other region, which is not physical. Secondly, the emphasis of this type of definition is based on the prior knowledge of the region boundaries, which is unknown before solving a dynamical problem. Thirdly, each region cannot have a constant damping values as there is a continuously varying pressure value which leads to distinct values of displacements and frictional force for each local point. The above explanation hence concludes that the definition of the damping must be spatially varying and continuous. This motivates to use the terminology of non-homogeneous description of the contact interface to define the proposed contact damping definition .

Referring back to the shapes of the dissipation curve obtained in the numerical investigation, a statistical fit using the conventional probability distribution functions can be used to predict the distribution of the continuous damping. As the contact stiffness has been defined as the function of pressure distribution, it is required to define the damping too as a function of pressure distribution. Mentioned below are some of the functions used for defining the distribution of the damping based on pressure distribution.

Inverse damping distribution as a function of the inverse absolute function of the pressure distribution,

$$d(x,y)=\frac{d_{loc}}{|P(x,y)-P_{\mathrm{m}}|}+d^{\infty}. \tag{4.14}$$

Rayleigh damping distribution as a function of the pressure distribution,

$$d(x,y)=\left(\frac{P(x,y)}{P_{\mathrm{m}}^2}\right)\exp\left(-\frac{1}{2}\left(\frac{P(x,y)}{P_{\mathrm{m}}}\right)^2\right)\chi_{\mathrm{r}}. \tag{4.15}$$

Normal damping distribution as a function of the pressure distribution,

$$d(x,y)=\frac{1}{\sigma_{\mathrm{m}}\sqrt{2\pi}}\exp\left(-\frac{1}{2}\left(\frac{P(x,y)-P_{\mathrm{m}}}{\sigma_{\mathrm{m}}}\right)^2\right)\chi_{\mathrm{n}}. \tag{4.16}$$

Log-normal damping distribution as a function of the pressure distribution,

$$d(x,y)=\frac{1}{P(x,y)\sigma_{\mathrm{m}}\sqrt{2\pi}}\exp\left(-\frac{1}{2}\left(\frac{\log(P(x,y))-P_{\mathrm{m}}}{\sigma_{\mathrm{m}}}\right)^2\right)\chi_{\mathrm{ln}}. \tag{4.17}$$

In all distribution functions, P_{m} refers to the corresponding pressure at which maximum dissipation is assumed to be occurring, χ is the scaling factor in the respective distribution functions and σ is the standard deviation of the contact pressure distribution. Among all possible choices, the Rayleigh damping distribution provides both the stable bounded definition for the damping with only two controlling parameters P_{m} and χ_{r}. The inverse damping distribution is not a stable function at $P(x,y) = P_{\mathrm{m}}$ and the other damping distribution require three controlling parameters. Among the two parameters used for Rayleigh damping distribution, P_{m} can be further reduced to a location parameter $P_{\mathrm{m}}^{\mathrm{loc}}$ as,

$$P_{\mathrm{m}} = \frac{\mathrm{mean}\big(P(x,y)\big)}{P_{\mathrm{m}}^{\mathrm{loc}}}. \tag{4.18}$$

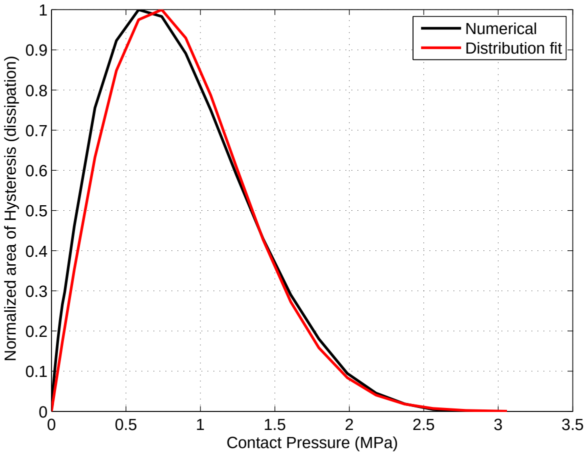

Figure 4.16: Normalized dissipation over the existing contact pressure at mating interface between 3D solid beam and rigid surface, see figure 4.7. Fit of the dissipation distribution using Rayleigh damping distribution with $P_{\mathrm{m}} = 0.7$.

The motivation behind defining the location parameter $P_{\mathrm{m}}^{\mathrm{loc}}$ is to normalize the parameter P_{m}. The location parameter $P_{\mathrm{m}}^{\mathrm{loc}}$ is a non-dimensional factor controlling the shifting of the P_{m} based on the mean of the pressure distribution at contact interface. For $P_{\mathrm{m}}^{\mathrm{loc}} = 1$ the maximum dissipation occurs at the mean of pressure distribution, for $P_{\mathrm{m}}^{\mathrm{loc}} > 1$ the maximum dissipation occurs below the mean of pressure distribution and for $P_{\mathrm{m}}^{\mathrm{loc}} < 1$ the maximum dissipation occurs above the mean of pressure distribution. Rayleigh distribution for the damping with location and scaling factor is used in this thesis for implementation of D-PDJ model. Figure 4.7 shows the normalized dissipation distribution with respect to local contact pressure for 3D solid beam example (see section 4.3.1). The Rayleigh damping distribution fits to the numerical results with choice of $P_{\mathrm{m}} = 0.7$, calculated based on equation (4.18) with $P_{\mathrm{m}}^{\mathrm{loc}} = 1.4$. Further discussions on the location and scaling parameters are studied in conjecture with experimental investigations of the test structures in the next chapter. The following section will discuss the implementation of damping definition in conjecture with conventional definitions of contact damping.

4.4.2 Implementation in FEM- Structural damping

After having formulations for defining the distribution of contact damping based on Rayleigh distribution, it is required to see the feasibility of its implementation in finite element codes for solving vibration problems. As discussed in chapter 3 too, the kind of damping obtained due to the dry frictional contacts is a form of structural or hysteretic damping [52, 83]. The structural damping often represented by loss factor is independent of the frequency of the excitation. Hence, the hysteresis area does not change with variation in excitation frequency for a constant amplitude of excitation. The loss factor is a dimensionless quantity and motivates the formulation of the Rayleigh distribution of damping to be modified in a way that it can be represented as the loss factor. The contact damping calculated based on the formulation in equation (4.15) has units of [mm^2/N] (inverse of pressure), which does not comply with units of viscous damping coefficient [N/(mm/sec)]. The Rayleigh distribution damping is converted to equivalent loss factor $\eta_{\mathrm{loc}}(x,y)$, as shown below in equation (4.19).

$$\eta_{\mathrm{loc}}(x,y) = P_{\mathrm{m}} d(x,y) = \left(\frac{P(x,y)}{P_{\mathrm{m}}}\right) \exp\left(-\frac{1}{2}\left(\frac{P(x,y)}{P_{\mathrm{m}}}\right)^2\right) \chi_{\mathrm{r}}. \tag{4.19}$$

The advantage of defining a dimensionless term for damping contribution (η_{loc}) is to avoid the emphasis on determining the physical relevance of the different parameters used in the formulation of the damping definition and also their specific values to be determined through various experimental investigations. The loss factor can be input directly in PDJ element and hence referred to as D-PDJ element, as shown in the figure 4.17 describing the element creation. The implementation of the structural damping as dry frictional contact damping in commercial software like Ansys v14 is accomplished by using a D-PDJ element. For performing modal analysis and obtaining the results of modal damping ratios, damped modal strain energy method is used [112]. The modal damping ratio (ξ^m) is defined as the ratio of the un-damped modal strain energy to damped modal strain energy, as shown below in equation (4.20),

$$\xi^{\mathrm{m}} = \frac{\sum\limits_{r=1}^{n} \phi_{\mathrm{m}} \eta_{\mathrm{loc}}^{r} K \phi_{\mathrm{m}}^{T}}{\sum\limits_{n=1}^{r} \phi_{\mathrm{m}} K \phi_{\mathrm{m}}^{T}}. \tag{4.20}$$

Figure 4.17 shows the implementation of the physical phenomenon of contacts as combination of the contact stiffness and damping using D-PDJ elements in conjecture with finite element modelling. Each D-PDJ element is characterized with a three dimensional spring element (PDJ element) accounting for the normal and tangential directions of stiffness contribution. In-plane (tangential direction) damper elements of D-PDJ element accounts for the contact damping. As the contact damping is associated with the

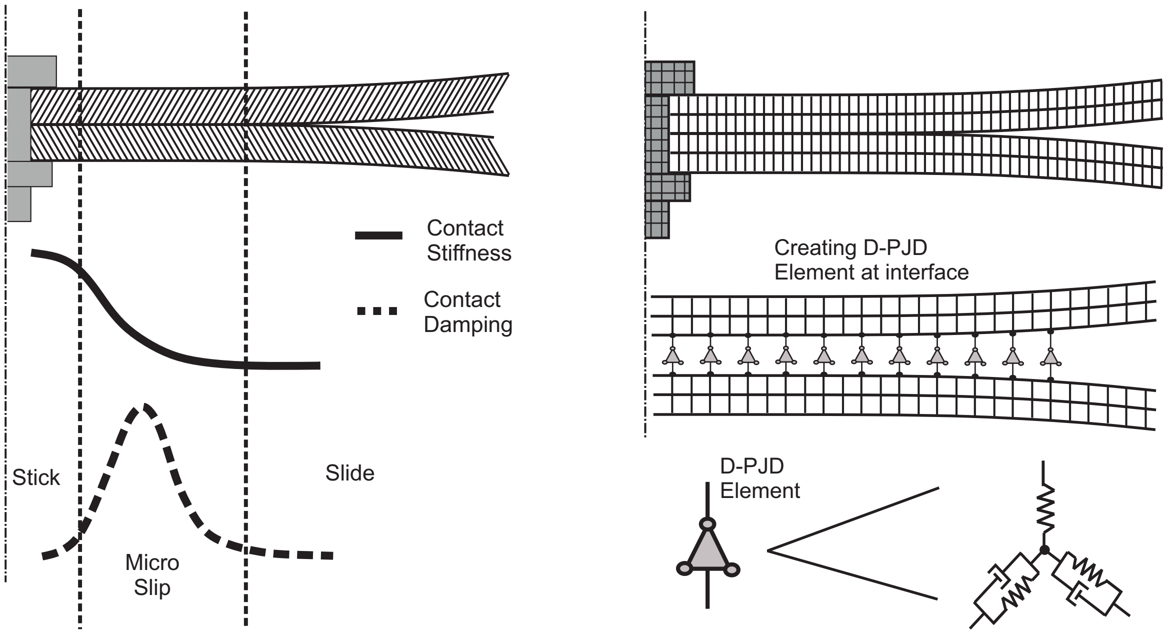

(a) Physical behaviour. (b) FE Implementation.

Figure 4.17: Division of regions with contact stiffness and damping distribution based on pressure distribution (left). Implementation of D-PDJ using finite elements (right).

relative motion between the two surfaces, the in-plane definition of the damping is sufficient to account for the assimilated behaviour of the dissipation through contacts. The normal direction of the damping for the normal contact problems is neglected here and the inherent material damping is then associated with the normal direction damping for the global structure.

4.4.3 Implementation in FEM- Contact Parameters

The proposed D-PDJ is derived based on the analytical and numerical model, which is dependent on various parameters to define the equivalent contact stiffness and damping. The contact parameters used in D-PDJ model are discussed here. The contact parameters governing the contact stiffness are curvature parameter (λ), saturation pressure (P_{N1}) and coupling factor (β_0). The contact stiffness has main influence on the modal frequency of a system, hence these parameters have influence on the modal frequency of a system. The contact parameters governing the contact damping are location parameter ($P_{\mathrm{m}}^{\mathrm{loc}}$) and scaling factor ($\chi_{\mathrm{r}}$). The damping has main influence on the magnitude of the system response, hence these parameters have influence on the resonance amplitude. This section discusses a possible way in which the values or range of values of these contact parameters can be obtained. The present discussion on the parameters is restricted to the room temperature conditions, as no investigation has been done to study the influence from environmental conditions.

Stiffness- Curvature Parameter (λ) : The curvature parameter defined in the exponential pressure-penetration curve is calculated as the inverse of the standard deviation of the surface roughness, see equation (4.9). The standard deviation of the surface roughness can be measured by approximating the distribution of the asperities with statistical distribution. The surface roughness varies according to the machining process, whose typical values for casting, fine machining, grinding and super-finishing are 10, 1-3, 0.25-0.8 and 0.02-0.4 μm respectively [100]. The corresponding curvature parameter for these values are 100, 1000-333, 4000-1250 and 50000-2500 mm^{-1}. Figure 4.18 shows the exponential pressure-penetration curves for different values of curvature parameter, corresponding to various machining process. As the surface roughness varies with respect to material, specimen's size and machining process, the values are approximately defined in some range, as mentioned above. Hence, it is not possible to calculate the exact value of curvature parameter. The exact value of curvature parameter can be obtained by model updating the simulation results of resonance frequency with respect to the experimental results.

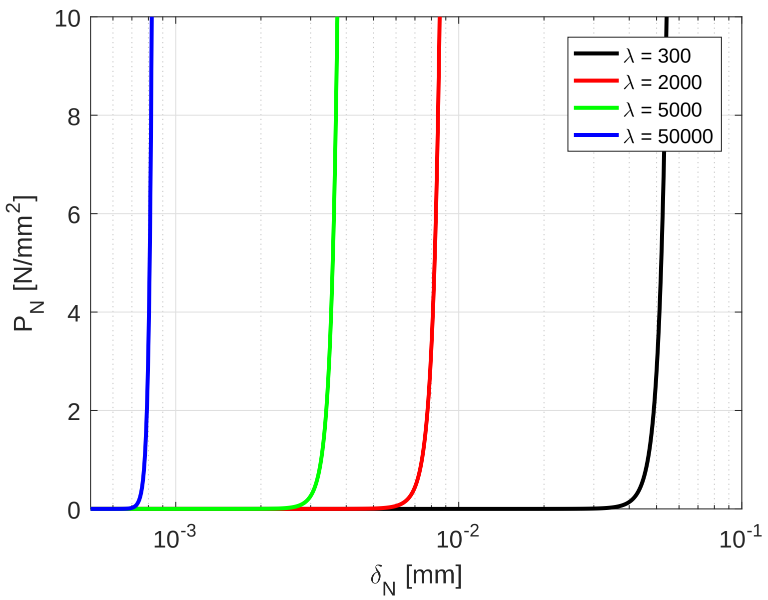

Figure 4.18: Exponential pressure-penetration curve for different values of the curvature parameter λ.

Stiffness- Saturation Pressure (P_{N1}) : The saturation pressure is a numerical parameter to enhance the numerical convergence of the exponential pressure-penetration curve, see equation (4.10). The product of curvature parameter and saturation pressure defines the maximum stiffness. This means a small variation in the saturation pressure has predominant influence on the stiffness. Figure 4.19 shows the normal stiffness variation with respect to normal pressure for set of different saturation pressure values. For simulation modelling, first the curvature parameter is calibrated with default value of $P_{\mathrm{N1}} = 1$ and then saturation pressure is optimized to match the resonance frequency from experiment.

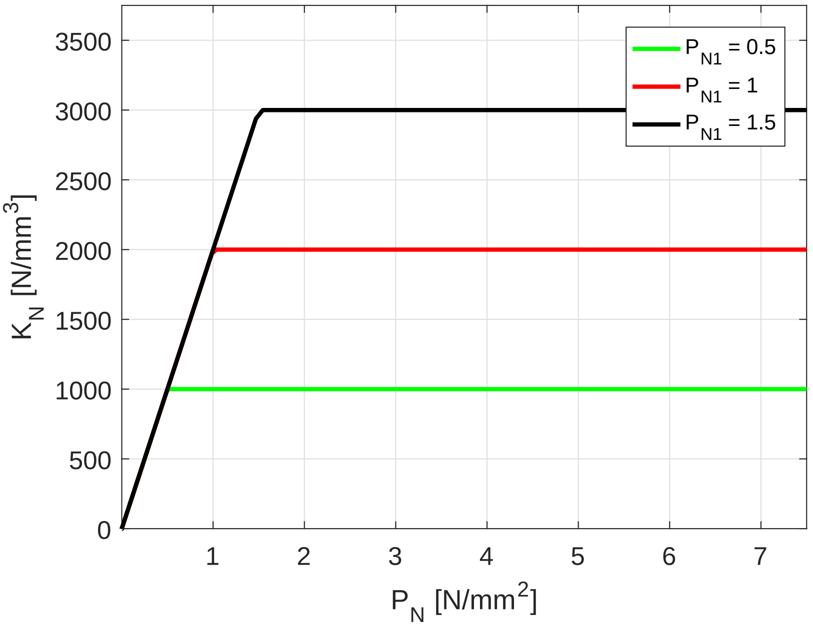

Figure 4.19: Contact stiffness density versus contact pressure for different values of saturation pressure parameter P_{N1}.

Stiffness- Coupling factor (β_0) : The coupling factor is used to calculate the tangential contact stiffness, see equation (4.12). The coupling factor is dependent on the elastic properties of the two materials in contact and is calculated as,

$$\beta_0 = \frac{4G^*}{E^*}, \tag{4.21}$$

where, $\frac{1}{E^*} = \frac{(1-\nu_1^2)}{E_1} + \frac{(1-\nu_2^2)}{E_2}$ and $\frac{1}{G^*} = \frac{(2-\nu_1)}{G_1} + \frac{(2-\nu_2)}{G_2}$.

For same materials in contact i.e. $G_1 = G_2$ and $E_1 = E_2$, the coupling factor reduces to a function of poisson's ratio.

$$\beta_0 = \frac{2(1-\nu)}{2-\nu}. \tag{4.22}$$

Table 4.1 shows values of coupling factor based on the elastic properties of materials in contact. For Steel-Aluminium contact pair the coupling factor is greater than 1 i.e. the tangential stiffness is larger than normal stiffness for sticking contact status.

Contact Pair	Elastic Constants	Coupling constant (β_0)
Steel-Steel	$E_1 = E_2 = 210$ GPa, $\nu_1 = \nu_2 = 0.3$	0.82
Aluminium-Aluminium	$E_1 = E_2 = 70$ GPa, $\nu_1 = \nu_2 = 0.28$	0.84
Steel-Aluminium	$E_1 = 210$ GPa, $\nu_1 = 0.3$ $E_2 = 70$ GPa, $\nu_2 = 0.28$	1.65

Table 4.1: Coupling constant for different pair of materials in contact.

Damping- Location Parameter ($P_{\mathrm{m}}^{\mathrm{loc}}$) : The damping location parameter defines the pressure at which maximum damping at the contact interface exists, see equation (4.18). This parameter is obtained by performing numerical investigation on simplified sub-model of the structure, as discussed in different examples of section 4.3. The choice of $P_{\mathrm{m}}^{\mathrm{loc}} = 1$ is ideal for most of the cases, where the pressure distribution has minimum value of zero. Figure 4.20 shows Rayleigh damping distribution curve based on equation (4.19), for different values of the damping location parameter.

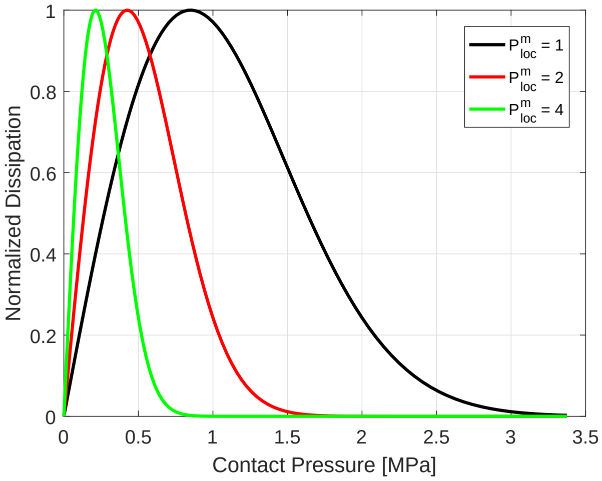

Figure 4.20: Contact stiffness density versus contact pressure for different values of saturation pressure parameter P_{N1}.

Damping- Scaling Parameter (χ_{r}) : The contact damping definition is derived based on numerical investigations of simplified beam models for set of bolting loads and excitation amplitudes, see section 4.3. However, to control the limits of damping for large and complex structures experiencing different levels of dynamic excitation, it is required to scale the damping distribution to have correct estimation of modal damping. The scaling factor is updated to match the experiment results of modal damping ratio of the global assembled structure. From numerical and experimental results of test structures studied in this thesis, the scaling factor tends to lie in the range of 0.01-10, whose exact value mainly depends on the bolting load and excitation amplitude.

Model validation of D-PDJ model on set of test structures is discussed in the following chapter, wherein the values of contact parameters are updated in simulation model to match the experimental results. The values of contact parameters used for a structure can be used for other structures, provided they have the same surface roughness and material coupling interface. For difference in the surface roughness and material pair coupling, corresponding contact parameters need to be calibrated to match experimental results. Also, the contact parameters are only applicable for metallic bodies in contact. Further discussion on the applicability of contact parameter values for different bolt loads are experimentally investigated in the following chapter 5.

Summary

This chapter explains the building process and implementation of the new proposed contact model. The notion used to build the proposed model is that the homogeneous non-linear definition of contact interfaces can be modelled with an equivalent local linearization and global non-homogeneous definition of contact interfaces. Development of model is accomplished under four parts. The first part describes the discretization of the contact interfaces using 3D Kelvin-Voigt elements. The equivalent stiffness and damping definition is required for the characterization of these discrete elements. The second part describes the derivation of the equivalent contact stiffness for both normal and tangential directions. A smoothing function is proposed for the definition of normal contact stiffness to enhance the numerical convergence. Third part describes the derivation of equivalent contact damping to describe the dissipation at contact interfaces under dynamic excitations. Modified Dahl model is used to obtain the dissipation profile over contact interface of double layered beam fasten with a bolted joint. The important observation is that maximum dissipation occurs at a region in between the high (near bolt) and low bonding pressure (far from bolt), wherein the dissipation profile resembles a statistical distribution function. A Rayleigh distribution as a function of contact pressure is proposed to define the contact damping distribution, with parameters controlling the position at which maximum damping occurs and magnitude of damping. As both the equivalent stiffness and damping definitions are based on the contact pressure, the model is referred as the Damped Pressure Dependent Joint model (D-PDJ). In last part, discussion on the implementation of the proposed D-PDJ in commercial software for modal superposition analysis is described. Due to use of local linear elements in the D-DPJ model, it is computationally efficient. With use of non-homogeneous definition of stiffness and damping in D-PDJ model, the predominant effects of contacts can be captured. The various contact parameters used in D-PDJ model for defining the equivalent contact stiffness and damping are listed below.

Contact stiffness	Curvature parameter (λ) Saturation pressure (P_{N1}) Coupling factor (β_0)
Contact damping	Location parameter ($P_{\mathrm{m}}^{\mathrm{loc}}$) Scaling parameter ($\chi$)

Chapter 5

Model Validation : Parametric Study

In the previous chapter, the mathematical background and implementation of D-PDJ model was explained. As the proposed D-PDJ model is a novel approach of modelling the contact interfaces, it is required to validate the model's capability in capturing the influences of contacts on the global dynamical behaviour. This motivates to perform an extensive parametric study of the influencing factors on dynamical behaviour of assembled structure and test the capability of D-PDJ model in capturing the influence of those factors in the simulation. This chapter discusses the parametric study on the set of test structures used for the model validation.

Test Structure

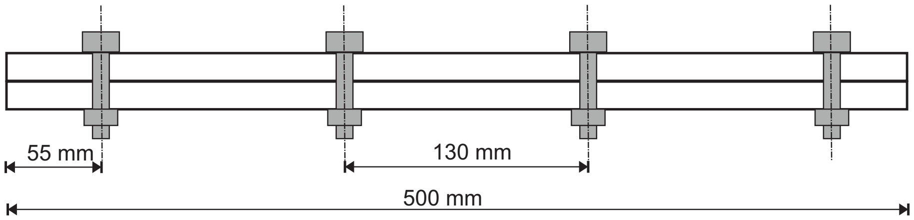

Figure 5.1: Test structure: A double layered beam fastened with 4 bolts of M6 size.

The test structure used is a double layered beam which is fastened using four bolted joints, similar to the structure used by GEISLER [39]. The two beams are identical in dimensions and are made of stainless steel. The beams are fastened using four M6 bolts. The dimension of an individual beam is 500 mm x 20 mm x 10 mm. Figure 5.1 shows a pictorial representation of the double layered beam test structure with its dimensions. The beam test structure is studied distinctly with three operational parameters, which influences the contact status and hence the dynamical behaviour of the test structure. These operational parameters are : bolting torque, excitation load and contact pairing materials. The proposed D-PDJ model is validated for the choice of each operational parameter, requiring different experimental set-up of the test structure. The output parameters used for the model validation are modal-frequencies and modal damping ratios.

The comparison of the Frequency Response Function (FRF) between the experiment and simulation is also performed. The optimized material properties of the beam structure are obtained from model updating the simulation results with Experimental Modal Analysis (EMA) results of a single beam. The resulting elastic properties of the stainless steel material used for the beam structure are shown in table 5.1.

Elastic Properties		Damping	
Young's modulus (E)	192 GPa	Mass factor (α_{r})	0.3
Poisons ratio (ν)	0.3	Stiffness factor (β_{r})	4.85e-08
Mass density (ρ)	7875 kg/m^3		

Table 5.1: Model updated elastic properties of the stainless steel beam used in Double beam test structure.

5.1 Effect of Bolting Torque : Contact Pressure

The first quantitative validation of D-PDJ model is done by studying the influence of the variation in the contact pressure on the dynamical behaviour of the test structure. The variation in the contact pressure is controlled by varying the bolting torque. With increase in the bolt torque, the contact pressure is also increased. However, the parabolic pressure distribution profile remains constant irrespective of the bolting torque magnitude. These observations were studied experimentally by GOULD AND MIKIC(1972) [41], ZIADA AND ABD(1980) [129]. The influence of the contact pressure on modal frequency and modal damping is studied by isolating the other influencing factors. This section is divided into three parts. The first part discusses the experimental set-up and its results, second part discusses the D-PDJ model's simulation work-flow and its initial results and in the final part the comparison between the experimental and simulation results are done.

5.1.1 Experimental Set-up

To obtain the influence from the bolt load, an Experimental Modal Analysis (EMA) of the test structure with bolting torque of 1 Nm, 3 Nm and 5 Nm is performed. The test structure is hanged freely using soft springs. The experimental set-up of the test structure is shown in figure 5.2. The structure is excited with an impulse modal hammer at a fixed location and roving measurements along the length of the beam are done using a 3D laser vibrometer (see figure 5.2). To avoid the variation of excitation amplitude, auto-magnetic controlled modal hammer is used. The auto controlled modal hammer excites the structure with approximately same amplitude for all measurement points. This ensures that the experiment investigations have been performed with no influence from the excitation amplitude and the results of the test structure are solely dependent on the variation of bolting torque.

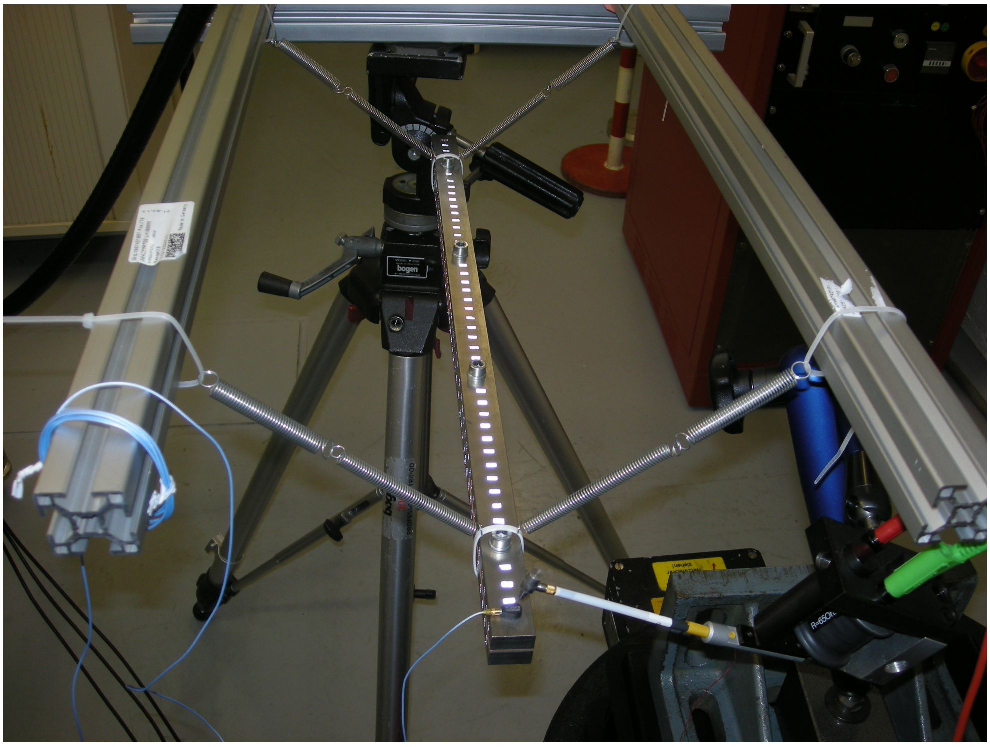

Figure 5.2: Set-up of freely hanging double layered beam test structure for experimental modal analysis and impulse excitation from modal hammer.

To have sufficiently tight contact while using M6 bolts, the general choice of bolting torque is around 8 Nm for fastening structural members. Higher bolting torques lead to damaging of screw threads and the lower bolting torques lead to loose contacts. The choices of 1 Nm, 3 Nm and 5 Nm bolting torque are taken to depict the cases of non-linear, moderate non-linear and slightly non-linear systems respectively.

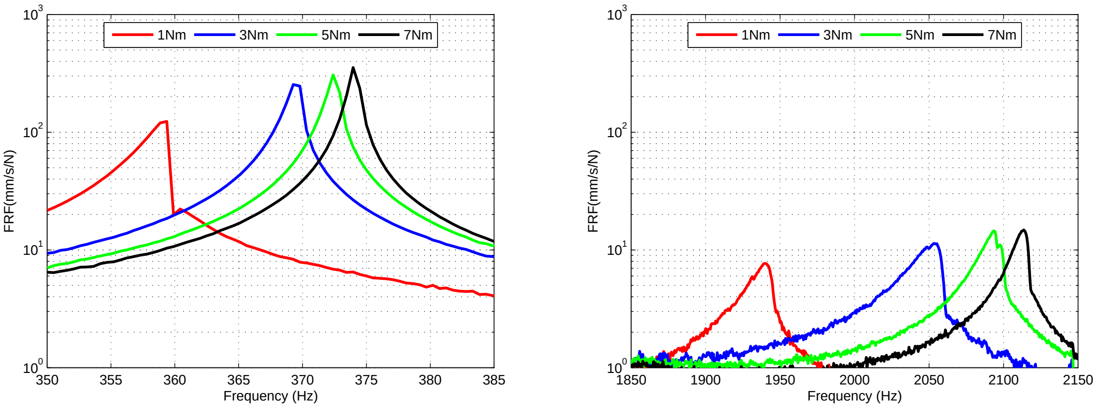

(a) Mode 1.

(b) Mode 7.

Figure 5.3: Effect of the bolting torque on the shape of mobility-FRF of the double layered beam test structure observed in experimental modal analysis.

Figure 5.3 shows the mobility-FRF's for modes 1 and 7 with different bolting torques. For linear system the FRF are symmetric in the resonance region and for non-linear system the FRF are un-symmetric in the resonance region, as described in section discussing non-linear vibration in chapter 3. It can be observed that the shape of mobility-FRF is sharp and symmetric for the choices of 5 Nm and 7 Nm bolt torques in both modes of vibration. Thus, the choice of 5 Nm defines the test structure to be a slightly non-linear structure. The choice of 1 Nm bolt torque clearly shows an un-symmetric and broad mobility-FRF shape and thus can be regarded as non-linear system in comparison to 5 Nm bolt torque case. The 3 Nm bolt torque is then regarded as moderately non-linear system. The modal frequencies and modal damping ratios for each case of the bolting torque are presented in tables 5.2 and 5.3 respectively.

Mode	Modal frequency [Hz]		
	1 Nm	3 Nm	5 Nm
1	361.85	371.13	373.07
2	405.28	405.33	405.35
3	826.69	899.01	910.16
4	1106.17	1106.34	1106.42
5	1559.85	1720.03	1770.14
6	1738.85	1785.56	1808.14
7	1980.01	2080.21	2120.37
8	2145.97	2146.42	2146.52
9	2820.21	2980.15	3040.01

Table 5.2: EMA results of the modal frequencies for double layered beam test structure for different choices of the bolting torque. In-plane modes are highlighted in grey colour.

Mode	Modal damping ratio (%)		
	1 Nm	3 Nm	5 Nm
1	0.295	0.151	0.127
2	0.035	0.031	0.032
3	0.425	0.245	0.161
4	0.026	0.025	0.026
5	0.650	0.345	0.172
6	0.095	0.173	0.092
7	0.261	0.239	0.176
8	0.031	0.028	0.027
9	0.281	0.226	0.158

Table 5.3: EMA results of the modal damping ratios for double layered beam test structure for different choices of the bolting torque. In-plane modes are highlighted in grey colour.

The initial observation shows that with increase in the bolt torque, the modal frequency also increases. This is an obvious phenomenon as with increase in the bolting torque, the contact pressure increases and hence leads to a substantial increase in the contact stiffness. A higher stiffness leads to higher modal frequency. On contrary, the modal damping ratio decreases with increase in the bolting torque. This result is also according to the expected behaviour, as increased bonding pressure results in the reduction of the relative displacement and hence reduces the damping. An interesting observation is for modes 2, 4 and 8 (highlighted in grey, see tables 5.2 and 5.3). There is no influence of the bolt load on both modal frequency and modal damping of these modes. The modal frequency and modal damping remain almost constant for all choices of the bolting torque and the value of modal damping ratios are very small. Modes 1, 3, 5, 6, 7 and 9 are the out-of-plane modes where as the rest of the modes are the in-plane modes. The difference in the behaviour of in-plane and out-of-plane modes is discussed in the following sections.

5.1.2 D-PDJ Simulation

The double layered beam test structure EMA results are to be validated with the simulation results. A pre-stress modal analysis is performed, wherein the pre-stress effects are accounted for the bolting loads in the static analysis step. The contact interfaces are modelled using D-PDJ elements, as described in the section 4.4.2, figure 4.17. The required material properties for the beam are taken from the table 5.1. The D-PDJ model is divided into three stages for performing a pre-stress modal analysis.

Step 1: The first stage is to perform the quasi-static loading of bolting torque and obtain the contact pressure distribution at the interface. The normal force for each bolt torque is calculated based on the equation (4.13) for a M6 bolt. The standard contact interface elements of Ansys v14 are replaced with D-PDJ elements with normal contact behaviour defined based on the pressure-penetration relation, see equation (4.4). The contact parameters required for this stage are the curvature parameter (λ), the saturation pressure (P_{N1}) and the coupling factor (β_0). The initial value of $\lambda = 2000$, $P_{\mathrm{N1}} = 1$ and $\beta_0 = 0.83$ are taken and later optimized to match the modal frequency results from EMA. Discussion on the values of contact parameters is done in the following section of comparison between the experiment and simulation results.

Step 2: The contact pressure result from the static analysis is used to calculate the updated contact stiffness density and the contact damping distribution. The contact stiffness density distribution is calculated based on the continuous fit formulation used in the equation (4.11). The contact damping as the structural damping loss factor is calculated based on Rayleigh distribution of contact pressure as shown in the equation (4.19). Figure 5.4 shows the calculated contact stiffness density and contact damping distribution for the double beam test structure. The localized damping distribution parameters $P_{\mathrm{m}}^{\mathrm{loc}}$ defining the location of maximum damping and the scaling factor χ_{r} are chosen as 1 for the initial calculations and later optimized to match the modal damping ratio results from EMA.

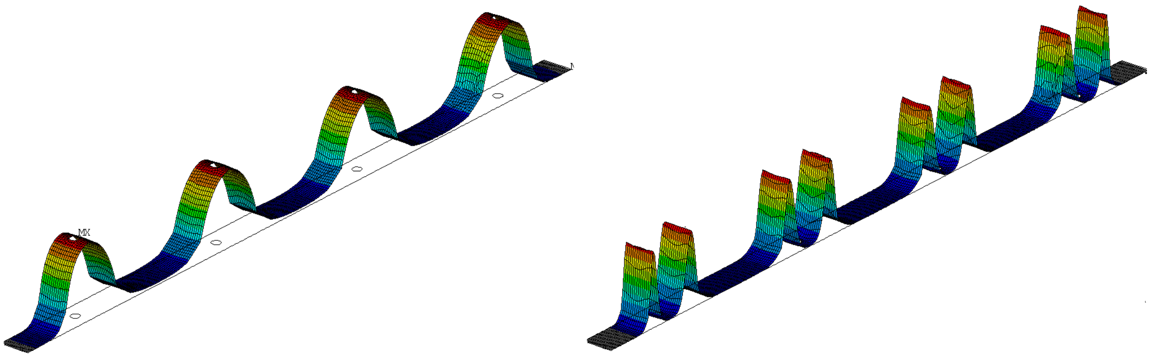

(a) Contact stiffness density.

(b) Contact damping distrubtion.

Figure 5.4: Use of D-PDJ model to estimate the corresponding contact stiffness and damping based on contact pressure.

Step 3: The D-PDJ element is revised to define the updated stiffness and damping with linear Kelvin-Voigt spring element to have a linear basis for the future modal superposition analysis. Modal analysis is performed with no boundary conditions (similar to experimental set-up), to get modal frequencies and mode shapes of the test structure. The modal damping ratios are calculated based on equation (4.20).

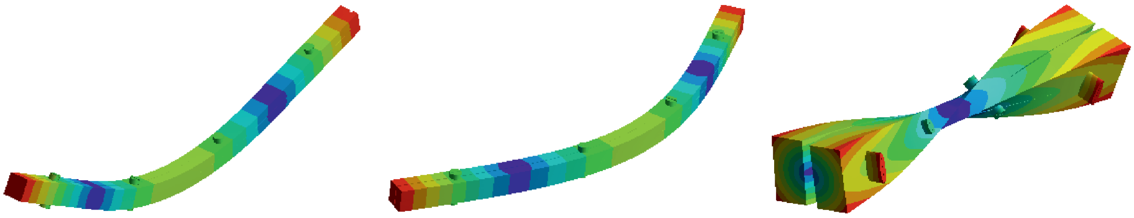

(a) Out-of-Plane bending
D-PDJ 1 Nm: 362 Hz / 0.3 %
D-PDJ 3 Nm: 372 Hz / 0.2 %
D-PDJ 5 Nm: 374 Hz / 0.1 %

(b) In-Plane bending
D-PDJ 1 Nm: 403 Hz / 0.06 %
D-PDJ 3 Nm: 403 Hz / 0.06 %
D-PDJ 5 Nm: 403 Hz / 0.06 %

(c) Torsion -
D-PDJ 1 Nm: 1770 Hz / 0.15 %
D-PDJ 3 Nm: 1798 Hz / 0.1 %
D-PDJ 5 Nm: 1835 Hz / 0.1 %

Figure 5.5: Mode shapes and corresponding modal frequency and modal damping ratio from D-PDJ simulation for 1 Nm, 3 Nm and 5 Nm cases of bolting torque of the double layered beam test structure.

The first three primary mode shapes for each case of 1 Nm, 3 Nm and 5 Nm are shown in figure 5.5. For all of the primary modes, the modal frequency increases and the modal damping ratio decreases with increase in bolting torque. It can also seen in D-PDJ simulation results too, that the in-plane bending mode has lower damping value in comparison to the damping values of out-of-plane modes. An elaborate discussion on the results obtained from D-PDJ simulations are presented in the following section of comparison between the experimental and simulation results.

Model Updating- Contact Parameters : The results shown in figure 5.5 based on steps 1, 2 and 3 of simulation model are obtained for some default choice of contact parameters. The simulation model is iterated to calibrate values of contact parameters to ensure a good match between the experiment and simulation results. The iterations are done in three steps. The first two iterations are required to calibrate contact stiffness parameters to match experiment modal frequency results. The third iteration step is required to calibrate the damping parameters to match experiment modal damping ratio results.

Iteration - I : In this step, the optimal value of curvature parameter in range $\lambda \in [1000, 4000]$ is to be estimated (with initial value of contact stiffness parameters: $\lambda = 2000, P_{\mathrm{N1}} = 1$ and $\beta_0 = 0.83$), such that error in modal frequency ($\varepsilon_{\mathrm{freq}}$) is minimum. The error in modal frequency for N_{m} modes is defined as,

$$\varepsilon_{\mathrm{freq}} = \frac{1}{N_{\mathrm{m}}} \sum_{\mathrm{n}=1}^{N_{\mathrm{m}}} \left(\left| \frac{f_{\mathrm{sim}}^{\mathrm{n}} - f_{\mathrm{exp}}^{\mathrm{n}}}{f_{\mathrm{exp}}^{\mathrm{n}}} \right| \right), \tag{5.1}$$

where, f_{exp} and f_{sim} are the modal frequency from experiment and simulation respectively. As the grinding machining process is used for the beam structure, the curvature parameter value is in range of 1000-4000, as discussed in the chapter 4- section 4.4.3. The coupling factor (β_0) value of 0.83 is calculated for steel-steel coupling pair based on the equation (4.22), for elastic constants of beam material available from table 5.1.

Iteration- II : After having optimal value of λ from iteration- I, value of $P_{\mathrm{N1}} \in [0.1, 10]$ is calibrated such that error in modal frequency ($\varepsilon_{\mathrm{freq}}$) of equation (5.1) can be further minimized. With this step the match can be improved to greater accuracy.

Iteration- III : After finding optimal choice of parameters influencing the modal frequency, the final step is to find optimal value of damping parameters such that error in modal damping ($\varepsilon_{\mathrm{freq}}$) is minimum. The error in modal damping for N_{m} modes is defined as,

$$\varepsilon_{\mathrm{damp}} = \frac{1}{N_{\mathrm{m}}} \sum_{\mathrm{n}=1}^{N_{\mathrm{m}}} \left(\left| \frac{\xi_{\mathrm{sim}}^{\mathrm{n}} - \xi_{\mathrm{exp}}^{\mathrm{n}}}{\xi_{\mathrm{exp}}^{\mathrm{n}}} \right| \right), \tag{5.2}$$

where, ξ_{exp} and ξ_{sim} are the modal damping from experiment and simulation respectively. The location parameter $P_{\mathrm{m}}^{\mathrm{loc}}$ value is approximately 1, obtained from numerical investigation of simplified beam model examples in chapter 4. This value is kept constant and iterations are done to calibrate the scaling parameter χ_{r}. From table 5.3, it can be seen that the range of modal damping is between 0.1 - 0.65 %, which is not large amount of damping for assembled structures. Hence, the scaling parameter will be smaller in values and the range selected for model updating is $[0.01, 1]$.

Based on the three steps of iterations, the optimized choice of contact parameters are obtained to match the experiment results of modal frequency and damping in Optislang software. The optimal choice of contact parameters for all three bolting torques of 1 Nm, 3 nm and 5 Nm are presented in table 5.7, in the following section.

5.1.3 Comparison

This section discusses the influence of the variation of bolting torque on system dynamical behaviour. A comparison between the D-PDJ simulation and the EMA results for the modal frequency and the modal damping ratio of the double layered beam test structure is done.

Influence on modes: It has been observed both in the simulation and experiment results that the in-plane bending modes have no influence of the variation in bolting torque on the modal frequencies and modal damping ratio. Whereas, for the out-of-plane bending modes, there is considerable increase in modal frequency and a reduction in the modal damping values with increase in the bolting torque. This observation can be explained by looking at the primary mode shapes shown in figure 5.5. For the out of plane bending mode, the two beams are experiencing the relative motion between each other at the contact interface. This is similar to phenomenon of beam bending theory, where the part of a beam above and below the neutral axis goes under compression and tension respectively. The interface can be thought as the neutral axis and relative motion at contact interface is accounted for the variation due to tension and compression. Where as for the in-plane bending modes, there is ideally no relative motion due to the same deflection of the upper and lower beams. The neutral axis for each beam in this motion does not intersect with the contact interface and hence does not change the contact status. The damping obtained for in-plane modes are hence associated to the inherent material damping of the beams. As it is required to study the influence of contacts, it is sufficient to compare the results of simulation and experiment only for the out-of-plane modes.

Mode	Modal frequency (Hz)			Modal damping ratio (%)		
	Exp.	Sim.	Error (%)	Exp.	Sim.	Error(*) (%)
1	362	360	0.6	0.30	0.32	6.7
3	827	824	0.4	0.42	0.44	4.8
5	1560	1540	1.3	0.65	0.57	10.8
7	1980	2026	2.3	0.26	0.25	3.8
9	2820	2909	3.2	0.28	0.22	21.4

Table 5.4: Comparison between EMA and simulation results of double beam test structure with 1 Nm bolt torque for the out-of-plane bending modes.

Modal frequency and damping: The comparison for the out-of-plane bending modes between EMA and D-PDJ simulation for case of 1 Nm, 3 Nm and 5 Nm bolt twisting moment are given in tables 5.4, 5.5 and 5.6 respectively. The maximum error in the modal frequency for 1 Nm bolt twisting moment is 3.1%, which is quite a good match for a system experiencing strong non-linearity, as seen in figure 5.3. A good estimation of modal damping ratio is also obtained. Maximum modal frequency error of 2.4% and 2.2% are obtained for 3 Nm and 5 Nm bolt twisting case respectively, which are in acceptable range. The damping values show much better match with experimental results for 3

Mode	Modal frequency (Hz)			Modal damping ratio (%)		
	Exp.	Sim.	Error (%)	Exp.	Sim.	Error(*) (%)
1	371	372	0.6	0.15	0.16	6.7
3	899	883	1.8	0.25	0.27	8.0
5	1720	1721	0.1	0.35	0.33	5.7
7	2080	2130	2.4	0.24	0.24	0.0
9	2980	3028	1.6	0.23	0.22	4.3

Table 5.5: Comparison between EMA and simulation results of double beam test structure with 3 Nm bolt torque for the out-of-plane bending modes.

Mode	Modal frequency (Hz)			Modal damping ratio (%)		
	Exp.	Sim.	Error (%)	Exp.	Sim.	Error (%)
1	373	374	0.3	0.13	0.12	7.7
3	910	890	2.2	0.16	0.15	6.25
5	1770	1743	1.5	0.17	0.20	17.6
7	2120	2148	1.3	0.18	0.15	16.6
9	3040	3050	0.3	0.16	0.15	6.25

Table 5.6: Comparison between EMA and simulation results of double beam test structure with 5 Nm bolt torque for the out-of-plane bending modes.

Nm and 5 Nm case in comparison to the case of 1 Nm. The optimized contact parameters used for cases of 1 Nm, 3 Nm and 5 Nm are shown in table 5.7.

Contact parameter	Bolting torque		
	1 Nm	3 Nm	5 Nm
Curvature λ	1450	2100	2200
Saturation pressure P_{N1}	0.5	0.8	0.8
Max. damping location $P_{\mathrm{m}}^{\mathrm{loc}}$	1	1	1
Scaling damping χ_{r}	0.1	0.06	0.05

Table 5.7: Used contact parameters for the D-PDJ simulation of the double beam test structure.

Contact parameters: The optimized contact parameters governing the contact stiffness (λ, P_{N1}) are approximately same for the choices of 3 Nm and 5 Nm bolting torque, but large deviation in comparison to the values used for 1 Nm bolting torque is seen. This suggests that the contact parameters governing the modal frequency stabilizes with higher bolting loads. The contact parameters governing the modal damping ratios are the maximum dissipation locating parameter $P_{\mathrm{m}}^{\mathrm{loc}}$ and scaling factor χ_{r}. The easiest choice of $P_{\mathrm{m}}^{\mathrm{loc}}$ is 1, which means that the maximum dissipation occurs at the contact pressure equal to the mean of contact pressure distribution, see equation (4.18). With increasing bolting load, the mean pressure too increases and hence automatically shifts the position of the maximum dissipation location. The scaling factor to control the modal damping values is high for the case of 1 Nm compared to values used for 3 Nm and 5 Nm bolting torque. Also, with higher bolting torque, the damping values also stabilizes with almost same damping values for the all modes. The choice of contact parameters used for both modal frequency and modal damping ratio control are similar for 3 Nm and 5 Nm bolting torque in comparison to 1 Nm bolting. This particular conclusion was also observed in the previous chapter, wherein the dissipation profile was almost similar for 3 Nm and 5 Nm bolt load in comparison to 1 Nm bolt torque, see figure 4.9. This suggests that the contact parameters governing the damping stabilizes with higher bolting loads. For both modal frequency and damping, the contact parameters stabilizes for higher bolt loads and hence it is concluded that the D-PDJ model can be used for moderately non-linear or linear systems with good accuracy in comparison to full non-linear systems.

The concluding remarks for the study of effect of the contact pressure on the dynamical behaviour are :

- The out-of-plane modes of the test structure are influenced due to the of contact interface non-linearity and the in-plane modes are influenced due to the inherent material properties.
- With increase in the bolting load- the modal frequency increases and the damping reduces. These observations have been captured with good accuracy using D-PDJ model.
- The choice of parameters used in D-PDJ model stabilizes with increase in bolting torque and hence the same parameters can be used for the higher bolting torques.
- The structure possessing moderate non-linearity are better captured by the D-PDJ simulation than structures possessing strong non-linearity.

5.2 Effect of Excitation : Relative displacement

As discussed in chapters 3 and 4, there is significant influence of the excitation amplitude on the dynamic behaviour of system having frictional contact interfaces. The influence of excitation amplitude on the shifting behaviour and cumulative area of local hysteresis can be seen in figures 4.12 and 4.14, wherein with increase in excitation amplitude, the cumulative dissipation increases and the position of maximum dissipation shifts near the bolt center. It is proposed to study and validate the influence of the excitation amplitude on the dynamical characteristics of the test structure with D-PDJ model. The comparison between the experimental and simulation results of mobility-FRF for the first four out-of-plane bending modes is done.

5.2.1 Test structure : Shaker Stinger Excitation

The experimental set-up is similar to the test structure used in previous section with the change in the excitation type as random Force Power Spectral Density (F-PSD). A stinger is used to transfer the point excitation load from an electrodynamic shaker to the test structure. The excitation is provided at one end of test structure and the velocity measurement with a laser vibrometer is done at the other end. The experimental set-up diagram is shown in figure 5.6. As observed from previous section, the bolting torque of 3 Nm is used, which accounts for the case of moderate non-linearity. The forced controlled PSD point excitation is done in the normal direction to excite the out-of plane modes. The frequency range for the excitation is 100-3000 Hz and root mean square (rms) value of 1 N, 2 N, 3 N and 4 N force are used. The shaker stinger experiment induces undesirable peaks due to the resonances of the stinger and other coupled effects on the FRF [8, 25, 69]. With use of least square complex exponential modal fit algorithms, the result of mobility-FRF from measurements are obtained with good accuracy, especially at the resonance regions. The comparison is then done with the modal fit synthesized mobility-FRF.

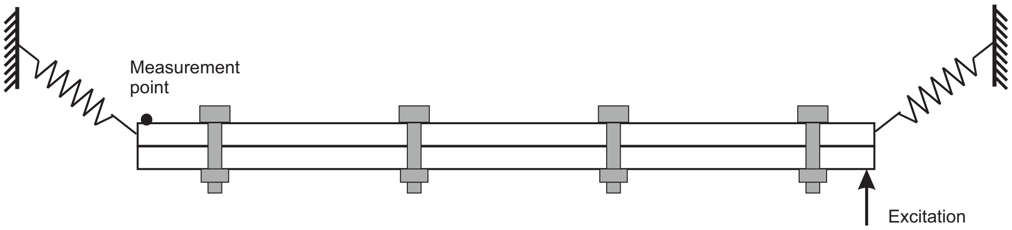

Figure 5.6: Set-up of shaker stinger excitation for the test structure with force controlled PSD at one end and measurement of velocity at other end.

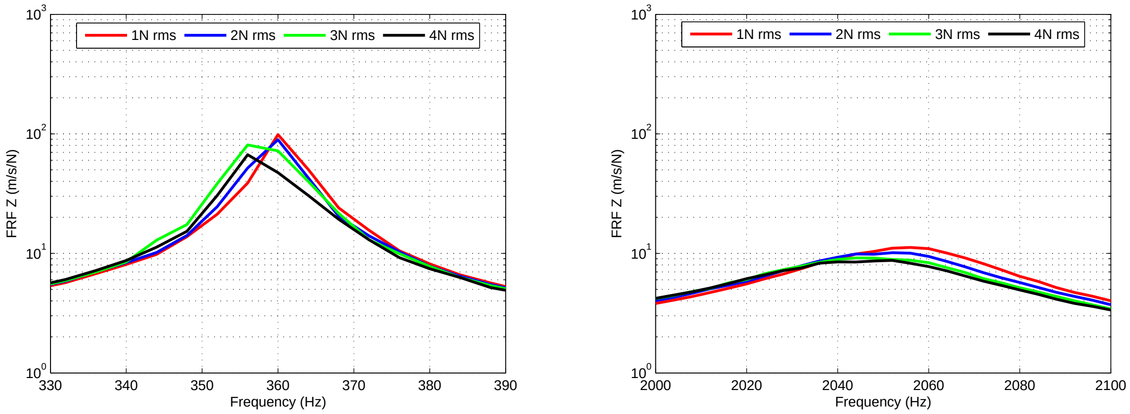

(a) Mode 1 (b) Mode 4

Figure 5.7: Effect of rms Force-PSD excitation amplitudes on the mobility-FRF of test structure with 3 Nm of bolting torque.

Figure 5.7 shows the effect on the mobility-FRF of the test structure with varying excitation amplitudes for 3 Nm bolting torque. It can be seen that with increase in the excitation amplitude, the resonance frequency decreases and the damping increases. The numerical investigation section in chapter 4 described the effect of increase in excitation amplitude on the contact dissipation, see figure 4.13. There is a slight difference between the resonance frequency from EMA (section 5.1- table 5.5) and shaker excitation result for the test structure. The reason for this difference is due to the added stiffness and mass from the stinger and force sensor, which are attached on the test structure for the shaker excitation set-up.

5.2.2 D-PDJ Simulation: PSD Analysis

In the D-PDJ simulation, the pre-stress modal analysis is extended to the random PSD analysis. A rigid mass of 30 gms is added at the point of the excitation on the double layered beam test structure. This accounts for the added weight to structure from force sensor. From the experiment observation, due to increase in the excitation amplitude the resonance frequency is decreased while the damping is increased. The decrease in resonance frequency is due to the decrease in the tangential contact stiffness. Also, with increase in the excitation amplitude, the dissipation area too increases leading to increase in the damping. The influence on the contact stiffness and damping is depicted in the figure 5.8.

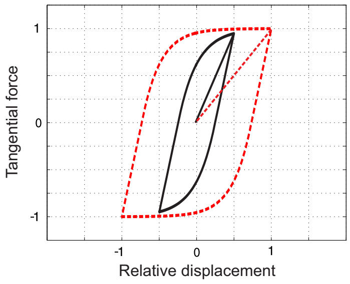

Figure 5.8: Increase in the hysteresis area and decrease in the slope with increase in the excitation amplitudes.

To accommodate the effect of the excitation amplitude, an equivalent reduction in the contact stiffness and an equivalent amplification in the damping is required. The contact stiffness can be modified with calibrating the value of the coupling factor β_0. The equivalent increase in the damping can be obtained through the use of scaling factor χ_r. These parameters are initially optimized for the reference case with the lowest loading amplitude, here 1N rms excitation amplitude. Later the cases for the higher excitation amplitude can be modelled with a slight variation in the excitation factor used in reference 1 N rms case. The other contact parameters for D-PDJ model are taken from the previous section 5.1. The comparison between the experimental and simulation results are shown in the following section.

5.2.3 Comparison

The comparison between the experimental results and simulation results of the mobility-FRF are of prime importance, especially in the resonance regions. The mobility-FRF shapes for random excitations are symmetric and hence a comparison with modal superposition frequency analysis is possible. Figure 5.9 shows a good match between the simulation and experimental results of double layered beam test structure for different excitation amplitudes, when fastened using 3 Nm bolting torque.

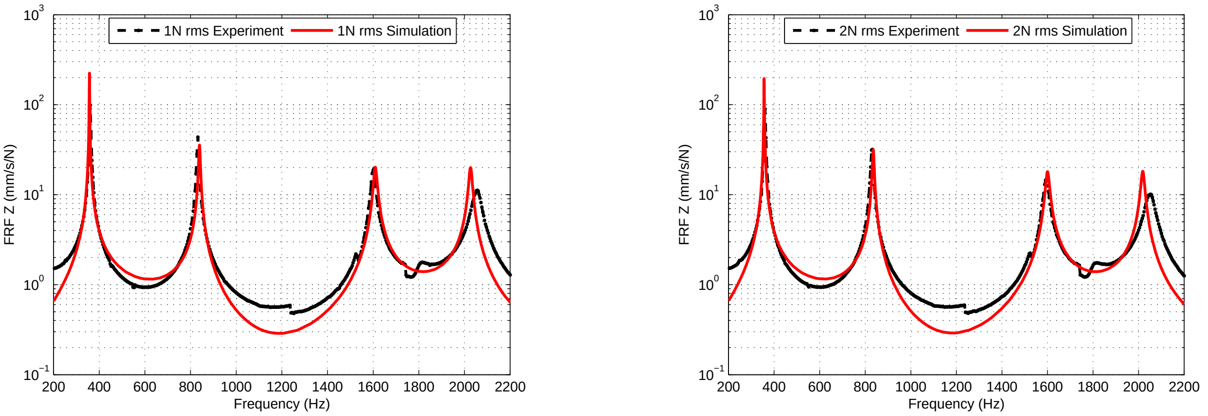

(a) 1N rms Excitation
Coupling factor $\beta_0 = 0.45$, Scaling factor χ_r=0.05.

(b) 2N rms Excitation
Coupling factor $\beta_0 = 0.425$, Scaling factor χ_r=0.075.

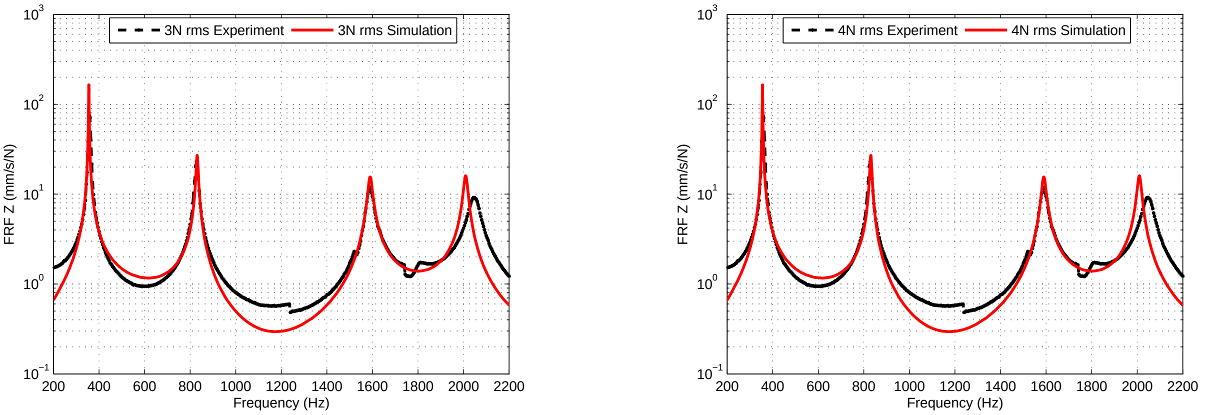

(c) 3N rms Excitation
Coupling factor $\beta_0 = 0.4$, Scaling factor χ_r=0.1.

(d) 4N rms Excitation
Coupling factor $\beta_0 = 0.375$, Scaling factor χ_r=0.125.

Figure 5.9: Comparison between shaker stinger experiment and D-PDJ simulation results of mobility-FRF of the double layered beam test structure with 3 Nm bolting torque.

The initial value of the coupling factor and the scaling factor for 3 Nm bolting torque are taken from the EMA results of the double beam test structure, see table 5.7. These parameters are optimized for 1N rms excitation and later for each of the excitation amplitudes the parameters are slightly updated. The optimized coupling factor and the scaling factor are presented in figure 5.9, for each amplitude of excitation. The coupling factor for 1N rms excitation is decreased approximately by a factor of half in comparison to the value used in EMA testing of double beam test structure. With use of both the coupling factor and scaling factor, there has been good match achieved with experiment, having maximum deviation for only higher frequency region.

5.3 Effect of Contact pair : Coupling parameter

The D-PDJ model has been validated for the pairing of identical materials in contact. However, it is also important to study the effect on the dynamical behaviour due to the change in contact pairing materials [31, 115]. For many industrial products, there exists contact between various different materials, ranging from assembling different isotropic materials to orthotropic/anisotropic materials. One of the very common application that can be seen is the use of laminated structures. The visco-elastic layered laminate not only reduces the weight of structure but also adds considerable damping to the structure. Many theoretical, numerical and experimental study related to the dynamical behaviour of composite structures is covered in wide range by authors like ROSS AND KERWIN [97], UNGAR [114], NI AND ADAMS [77], RAO ET.AL [94], QATU [91] etc. As the aim of this thesis is more concentrated towards the non-linear behaviour from contacts, the detailed modelling of the materials is not covered for dynamical behaviour. However, it is still required to study the vibration behaviour of the assembled structures involving laminate plates, wherein the laminates are fastened between the structures with non-uniform pressure distribution (not perfectly bonded). This defines the global damping as cumulation of material damping due to material deformation of laminate and contact damping due to the susceptibility of relative motion from contact pressure distribution. This section will use both forms of excitation mentioned in the previous sections, Impulse hammer excitation and shaker stinger excitation to compare the results for modal and random PSD analysis. The experimental set-up of test structure and the corresponding discussion for material and contact modelling is discussed in following subsections.

5.3.1 Experimental Setup

The test structure used in this section is an extension of the double layered beam test structure used in previous sections. The test structure is modified by fastening the laminate plates in-between two beams using the bolt joints. The bolted joints are used to control the contact pressure distribution, to study the influence of the bolt load on the dynamical output for dissimilar contact pairs. The laminate structure used is a copper-prepreg-copper plate. This enables the contact pair as a pair of the non-identical materials

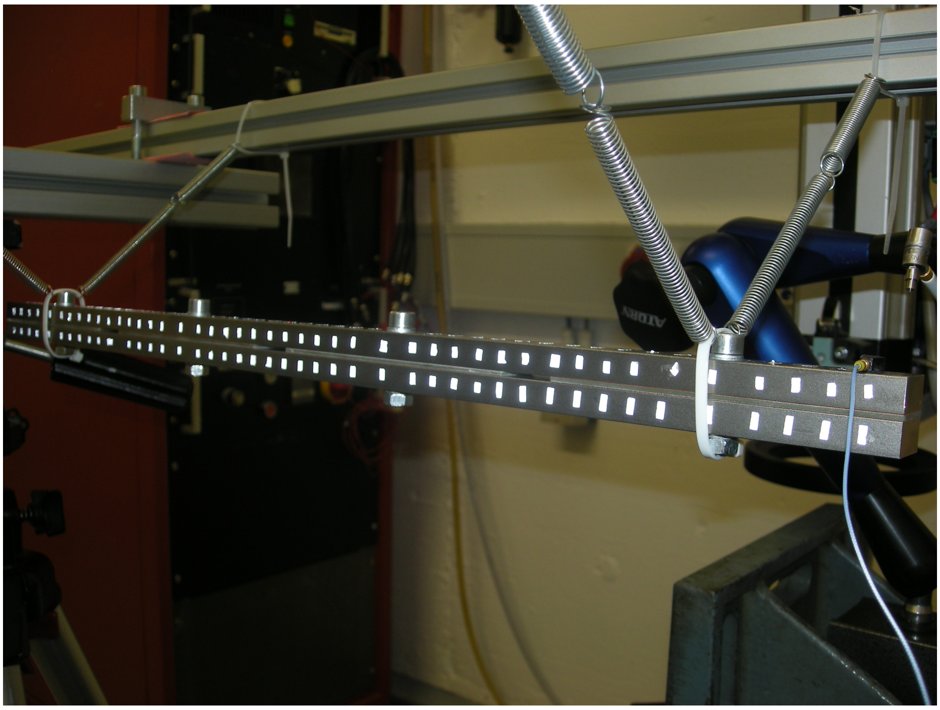

Figure 5.10: Experimental set-up of freely hanging laminate beam structure for EMA with laminate plates fastened between the two beams.

and also this is a combination of isotropic (steel beams) and ortho-tropic (laminate) materials. The built-up diagram of the laminate beam test structure is shown in figures 5.10 and 5.11.

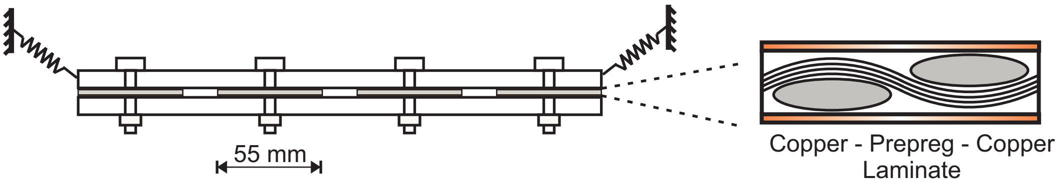

Figure 5.11: Setup of Shaker Stinger Excitation for laminate beam test structure.

The copper-prepreg-copper plate is a laminate structure made by coating thin copper sheets over the prepreg composite layer. A prepreg layer is 8 layers stacked laminate of single prepreg layer. Each prepreg layer is a plain woven structure of glass-fibre and epoxy-matrix. The dimension of the copper-prepreg-copper laminate plate is : 110 mm x 20 mm x 1.6 mm, with copper layer thickness of 0.055 mm and prepreg layer thickness of 1.49 mm. The length of the laminate is sufficiently long to accommodate the influence of bolt load. GOULD AND MIKIC(1972) [41], ZIADA AND ABD(1980) [129] established that the circular influence zone of the contact pressure is 3.5 times the diameter of the connecting bolt. Here, 3.5 times the diameter of M6 is sufficient to obtain a continuous varying pressure distribution over the contact interfaces between the beam and copper-prepreg-copper laminate plate.

The simulation requires material properties of all the different materials used in the laminate beam test structure, here required are the material properties for the copper-prepreg-copper laminate plate. A detailed modelling of prepreg requires to cover the multi-scale modelling of woven patterns and further extensions on the description for visco-elastic orthotropic material modelling. However, such detailed model increases the complexity of the model with very large computational time. The different modelling techniques of copper-prepreg-copper laminate structure with estimation of equivalent elastic constant is shown in the next section. EMA of a free hanging copper-prepreg-copper laminate is done as the reference for the model updating, to estimate optimized material properties of the copper-prepreg-copper laminate plate. The comparison between the experimental and simulation results for modal frequency of copper-prepreg-copper laminate is shown in the part of the modelling of laminate.

The experimental validation of the laminate beam test structure is done in two phases. In the first phase, the laminate beam test structure is excited with impulse hammer to obtain the modal frequency for comparison with D-PDJ model simulation results. The quantitative validations are performed with variation in bolt twisting moments of 1 Nm, 3 Nm and 5 Nm. In second phase, the laminate beam test structure is excited with shaker stinger forced controlled PSD and comparison of the FRF between experiment and D-PDJ model simulation results are done. This is to validate the combined stiffness and damping effect on the dynamical behaviour for different bolt twisting load for broad band excitation. As concluded in the section 5.1 that only out of plane bending modes are influenced due to contacts, therefore the comparison between the experiment and simulation results are done only for out of plane bending modes.

5.3.2 Modelling of laminate

Three approaches are used in modelling copper-prepreg-copper laminate, which are used to predict the equivalent elastic constant. The first method is an approach of estimating the equivalent elastic constants for the complete laminate plate based on the homogenization methods, such that equivalent elastic constant for complete copper-prepreg-copper plate are obtained. The other two methods concentrate on modelling the copper-prepreg-copper plate as the combination of three layered structure, wherein the prepreg layer is modelled as an orthotropic material and copper layer as isotropic material. The following section discusses the three methods and their comparison with EMA results.

The first method (M-I) is based on the homogenization method of estimating the equivalent elastic constants of the laminate, presented by SUN 2002 [109] . A reduction in the number of components of the compliance tensor is made by assumption of the transverse isotropy for the copper-prepreg-copper laminate. This is based on the approximation of same volume fraction and dimensions of the fill and warp fibre in prepreg layer. The optimized values of transverse isotropic elastic constants for copper-prepreg-copper laminate are presented in table 5.8. The second approach is to establish mesh connectivity

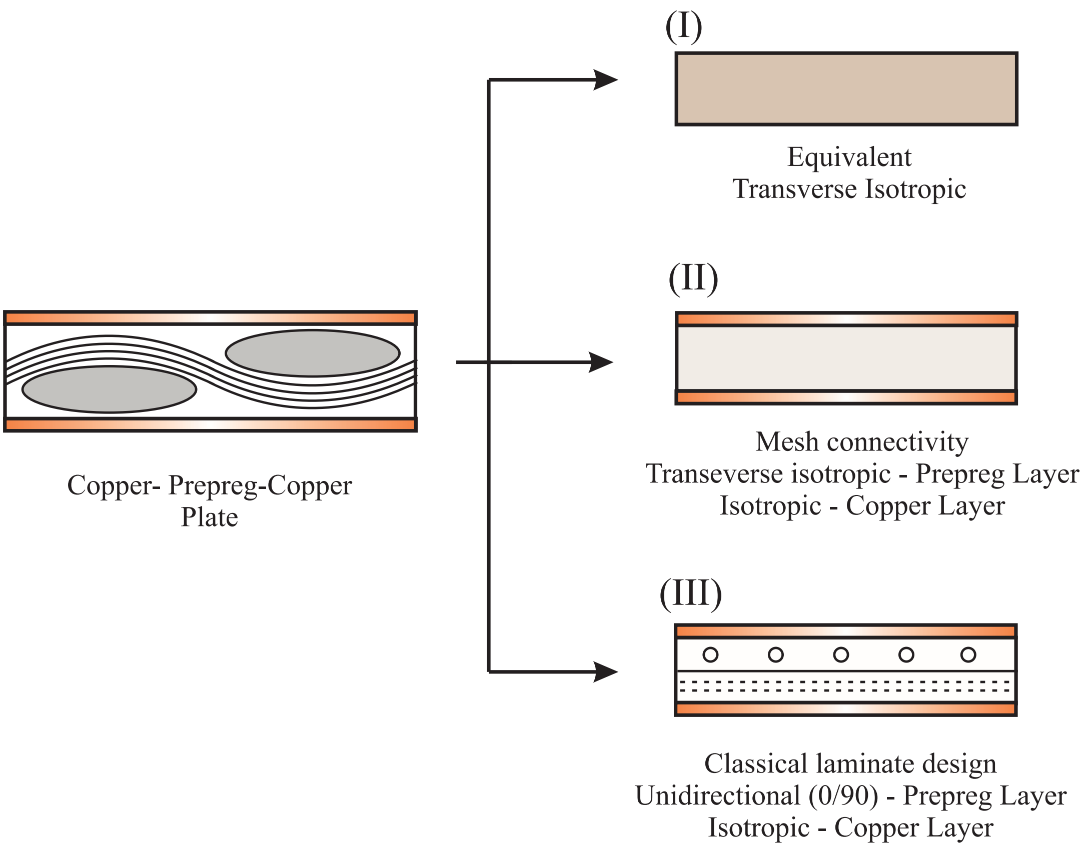

Figure 5.12: Three Modelling approaches of copper-prepreg-copper plate.

(M-II) between copper and prepreg layers to model a perfectly bonded structure with two different materials. The transverse isotropic elastic constants for the prepreg layer are obtained using Halpin-Tsai equations [47]. The material properties for the copper layer are kept constant and choice for the optimal values for the prepreg layer are optimized based on the EMA results. The third method (M-III) is based on the classical laminate theory to model the copper-prepreg-copper plate as a laminate structure with isotropic (copper layer) and transverse isotropic layers (prepreg layer) of different thickness respectively. The woven configuration of prepreg layer is modelled as a cross ply laminate, where 0° oriented ply represents the fill fibre direction and 90° oriented ply represents the warp fibre direction. Each unidirectional laminate has been modelled using classical rule of mixtures and then stacked up to form the complete equivalent cross-ply prepreg layer [105]. The initial values of elastic constants are taken from Hanselka (1999) [48] and then updated to match the EMA results. A pictorial representation of three modelling approaches of copper-prepreg-copper plate has been presented in figure 5.12. The elastic constants used for each approach are presented in table 5.8.

The comparison of modal frequency between EMA and simulation of copper-prepreg-copper plate using three modelling techniques is shown in table 5.9. All three methods show good match with experimental results, with methods M-II and M-III showing much better results than method M-I. The homogenization method (M-I) is also not proposed

Method I	Method II	Method III
Equivalent Cu-PCB Transverse Isotropic $E_x = E_y = 38$ GPa $G_{xy} = 11$ GPa $\nu_{xy} = 0.13$ $\rho = 2285$ kg/m^3	Pre-preg Transverse Isotropic $E_x = E_y = 25$ GPa $G_{xy} = 5.5$ GPa $\nu_{xy} = 0.128$ $\rho_{preg} = 1809$ kg/m^3 copper Layer $E = 85$ GPa $\nu = 0.34$ $\rho_{cu} = 8850$ kg/m^3	Unidirectional Ply Transverse Isotropic $E_x = 35$ GPa, $E_y = 15$ GPa $G_{xy} = 4.9$ GPa $\nu_{xy} = 0.25$ $\rho_{preg} = 1809$ kg/m^3 copper Layer $E = 85$ GPa $\nu = 0.34$ $\rho_{cu} = 8850$ kg/m^3
Damping Mass factor : $\alpha_r = 20$ Stiffness factor : $\beta_r = 2e-7$		

Table 5.8: Optimized elastic constants used in the modelling approaches of copper-prepreg-copper plate with dimensions of 163 mm x 113 mm x 1.6 mm.

Mode	EMA [Hz]	Simulation models [Hz]					
		M-I	Error (%)	M-II	Error (%)	M-III	Error (%)
1	196	199	1.8	197	0.4	195	-0.6
2	248	254	2.6	253	1.9	252	1.8
3	474	478	0.8	474	0.1	472	-0.5
4	548	532	-2.9	537	-2.0	539	-1.6
5	636	655	2.9	640	0.7	637	0.2
6	739	714	-3.4	732	-0.9	737	-0.3
7	917	923	0.7	920	0.4	919	0.2
8	1010	1000	-1.1	1000	-1.1	998	-1.2
9	1380	1376	-0.3	1386	0.5	1394	0.9
10	1470	1455	-1.1	1454	-1.1	1458	-0.8
11	1520	1497	-1.6	1501	-1.2	1502	-1.2
12	1600	1578	-1.4	1586	-0.9	1592	-0.5
13	1610	1585	-1.5	1595	-0.9	1601	-0.5
14	1960	1910	-2.6	1928	-1.6	1937	-1.2
15	2190	2167	-1.1	2178	-0.5	2186	-0.2

Table 5.9: Modal frequency comparison between EMA and simulation models of copper-Prepreg-copper plate.

to be used with contact modelling, as it would lead to modelling of a contact between isotropic and orthotropic material and increasing complex formulations to describe the mechanics. Whereas with other two methods, M-II and M-III, the copper layer being isotropic preserves the isotropic-isotropic contact law's assumptions and formulations.

For M-II the difficulty is to have the numerical convergence for the assembled structures due to the use of very thin layer of copper layer (here 55μm). Hence, M-III based on the classical laminate principle is proposed for the modelling of copper-prepreg-copper plate.

Other result of the experimental modal analysis is the modal damping ratio. As the prepreg material is visco-elastic in nature, the damping behaviour of copper-prepreg-copper plate is frequency dependent. Also, the directional dependent damping definition for prepreg layer is required for detailed modelling [12, 48, 77]. The present modelling techniques of directional dependent definition for materials is not possible in Ansys v14 software but a frequency dependent material damping can be defined for solving full harmonic analysis. However, the maximum modal damping obtained from EMA is approximately 0.2 % and it is approximated with proportional material damping parameters. The chosen material damping parameters are shown in table 5.8.

5.3.3 Comparison : Modal Analysis

This section discusses the comparison between the experimental results and the D-PDJ simulation results of modal frequency for the laminate beam test structure.

Contact Parameters : The copper layer of copper-prepreg-copper plate in contact with stainless steel defines the contact between two different isotropic bodies. The coupling factor is calculated based on the equivalent Young's and shear modulus for a pairing of copper and stainless steel as,

$$\beta_0 = \frac{4G^*}{E^*} = 1.12. \tag{5.3}$$

The elastic constants of the copper and steel materials of laminate and beam structure are available from tables 5.1 and 5.8 respectively. As the surface roughness of steel and copper constitute to another standard deviation of the surface roughness, values of curvature and saturation pressure parameter will be different from the values used in previous study. However, old values are used as initial values to start the first iteration and calibrated to match the experimental results. Here, only 3 Nm case is used as the reference case to calibrate the contact parameters. The same values will be used for 1 Nm and 5 Nm bolting torque, to check the parameter's applicability for other bolting torques.

The optimized contact parameters governing the pressure distribution for normal loading, i.e λ and P_{N1} are obtained after model updating as 1850 and 1.5 respectively. Comparison of the modal frequencies of the EMA and D-PDJ model simulation for the bolting torques of 1 Nm, 3 Nm and 5 Nm is given in table 5.10, 5.11 and 5.12 respectively. This enables to extend the validation study based on the influence of contact pairs for non-linear (1 Nm), moderate non-linear (3 Nm) and slightly non-linear (5 Nm) structures.

Mode Number	Modal frequency (Hz)		
	Experiment	Simulation	Error (%)
1	390	398	1.9
2	402	400	-0.4
3	896	901	0.6
4	1098	1094	0.4
5	1606	1679	-4.5
6	1655	1676	1.3
7	2070	2093	1.1
8	2132	2122	-0.5

Table 5.10: Comparison between EMA and PDJ simulation of laminate beam structure (see figure 5.10) having 1 Nm bolt twisting moment with parameters $\lambda = 1850$ and $P_{\mathrm{N1}} = 1.5$.

Mode Number	Eigenfrequency (Hz)		
	Experiment	Simulation	Error (%)
1	402	400	-0.5
2	403	406	0.7
3	955	942	-1.4
4	1098	1094	-0.4
5	1696	1712	0.9
6	1784	1808	1.3
7	2132	2121	-0.5
8	2186	2190	0.2

Table 5.11: Comparison between EMA and PDJ simulation of laminate beam structure (see figure 5.10) having 3 Nm bolt twisting moment with parameters $\lambda = 1850$ and $P_{\mathrm{N1}} = 1.5$.

D-PDJ Simulation results show a good match with the EMA results for the laminate beam test structure. The maximum error in the modal frequency for 1 Nm, 3 Nm and 5 Nm bolt twisting moments are 4.5%, 1.4% and 2.1% respectively. The mean of the absolute error in the modal frequency for 1 Nm, 3 Nm and 5 Nm bolt twisting moments are 1.34%, 0.74% and 0.54% respectively. From both the maximum error and the mean absolute error, it is clear that the D-PDJ model has good match with the EMA results for 3 Nm and 5 Nm bolting torques than 1 Nm bolting torque case. This observation was also seen in previous section 5.1, i.e. the D-PDJ has good prediction for moderately non-linear system (3 Nm and 5 Nm) than highly non-linear systems (1 Nm). For the case of 1 Nm also, the maximum variations have been only for two modes (modes 5 and 10) with rest all modes showing good convergence. In the previous section 5.1, choice of contact parameters - curvature parameter λ and saturation pressure P_{N1}, were optimized for each bolting torque case. However, the results presented in this section are based on the same values

Mode Number	Eigenfrequency (Hz)		
	Experiment	Simulation	Error (%)
1	402	400	-0.5
2	407	408	0.2
3	975	955	-2.1
4	1098	1093	-0.5
5	1719	1724	0.3
6	1850	1849	0.0
7	2132	2121	0.5
8	2230	2226	-0.2

Table 5.12: Comparison between EMA and PDJ simulation of laminate beam structure (see figure 5.10) having 5 Nm bolt twisting moment with parameters $\lambda = 1850$ and $P_{\mathrm{N1}} = 1.5$.

of contact parameters used for all 1 Nm, 3 Nm and 5 Nm bolting torque cases. This is motivated to study the variation in the quality of the match between the experiment and D-PDJ simulation results with use of the generalized values of the contact parameters. It is clear from the good match between EMA and D-PDJ results that the same values of contact parameters can be used for different bolting torques for the test structure. The curvature parameter and saturation pressure were chosen as trial choice based on the mean of the values used for the double beam test structure, see table 5.7. Hence, it can be concluded that D-PDJ model predicts the modal frequency to good accuracy for configurations involving contacts between different materials for moderately non-linear systems.

5.3.4 Comparison : Random Analysis

The second experiment performed on laminate beam test structure is to study the influence on the Frequency Response Function (FRF) for dynamic excitations. Two cases of bolt torques- 3 Nm and 5 Nm are chosen. The choices have been to study the effect of contact pair in dynamical domain for moderately non-linear and slightly non-linear cases. The mobility-FRF will show the influence on the resonance frequency and damping due to contact non-linearity through combination of bolt load and excitation effect. Experiment setup is similar to previous study for the excitation parameter study of double beam test structure. The laminate beam test structure is excited with an amplitude of 1N rms using force controlled PSD in frequency range of 100-2500 Hz. As some modifications were done in the previous study for the excitation parameter study of double beam test structure, similar modifications to simulation model are also done here to accommodate the effects of the added mass through force sensor and stingers. The mobility-FRF results comparison between experiment and D-PDJ simulation for 3 Nm and 5 Nm bolt twisting moment are shown in figures 5.13 and 5.14 respectively.

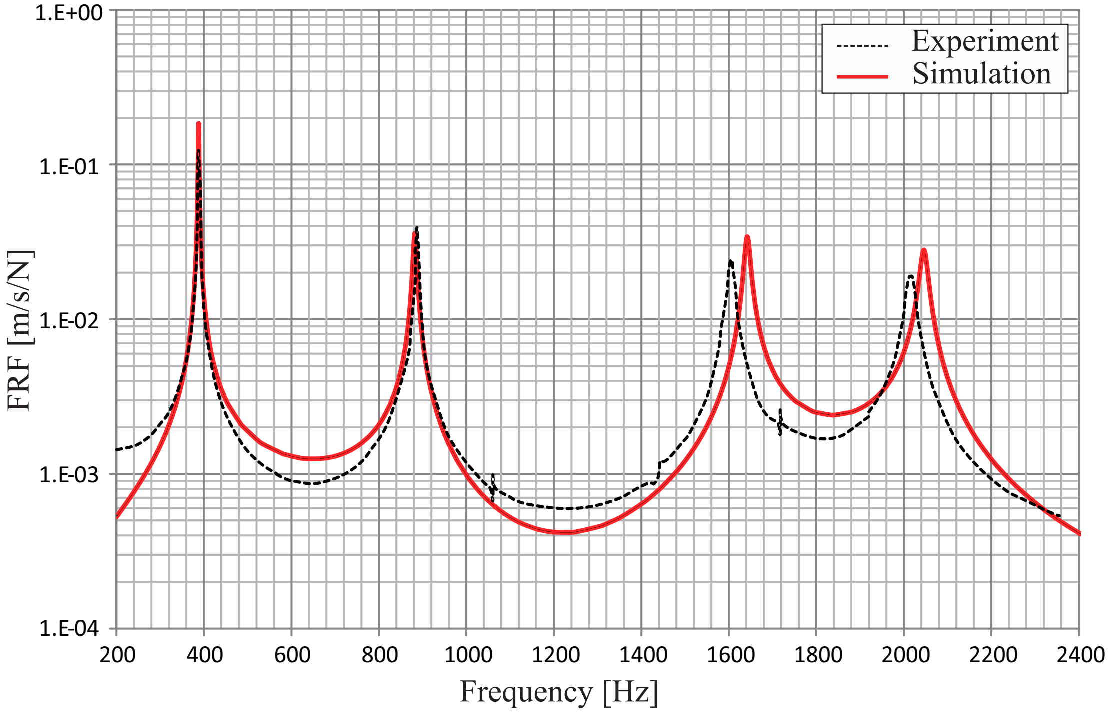

Figure 5.13: Mobility-FRF comparison between experiment and D-PDJ simulation of laminate beam test structure with 3 Nm bolt twisting moment using shaker excitation.

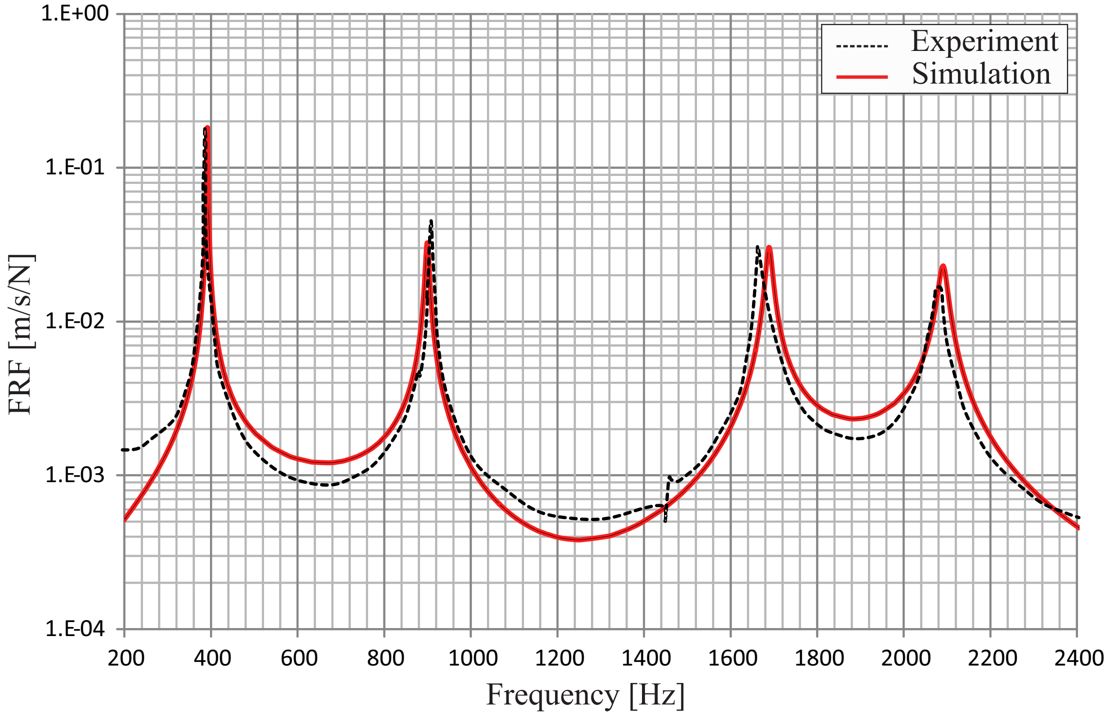

Figure 5.14: Mobility-FRF comparison between experiment and D-PDJ simulation of laminate beam test structure with 5 Nm bolt twisting moment using shaker excitation.

The choices for contact parameters governing the contact stiffness are same as the used in the previous comparisons of modal frequency EMA results, see tables 5.11 and 5.12. The coupling factor $\beta_0 = 0.56$ is taken, equal to the half of the initial value taken for EMA comparison, as shown in equation (5.3). This decreased value in the coupling factor is motivated from the value taken in the previous section 5.2 discussing the study of excitation effect on dynamic behaviour of test structure. The locating parameter $P_{\mathrm{m}}^{\mathrm{loc}}$ is chosen as 1, similar to values used in the EMA comparison for the laminate double beam structure. This suggests that the maximum damping is at the mean of the pressure distribution. Also, the scaling factor χ_r used in the definition of local damping is chosen as 0.1, similar to values used in the EMA comparison for the laminate double beam structure. A good convergence between the experiment and simulation in the regions of resonances on the mobility-FRF curves is obtained for both cases for 3 Nm and 5 Nm, with 5 Nm cases better than 3 Nm. This confirms the observation that with systems tending towards linearity, the D-PDJ model predicts the dynamical behaviour with good accuracy.

Summary

This chapter discussed the parametric study of the influencing factors like bolting torque, excitation amplitude and contact pair on the dynamic characteristics of structures having bolted joints. A test structure of double layered beam with 4 bolted joints is taken for studying the three influencing factors. The effects of bolting torque is studied by making three choices of bolting torque i.e. 1 Nm, 3 Nm and 5 Nm bolting torque to resemble non-linear, moderate non-linear and slightly non-linear structures respectively. The test structure is excited with a constant amplitude using an auto controlled modal hammer, to eliminate influence from variation and location of excitation. A good match between the experiment and D-PDJ simulation is obtained for cases of 3 Nm and 5 Nm bolting torques in comparison to 1 Nm bolting torque. The optimized contact parameters used for 3 Nm and 5 Nm are almost of same values, but for 1 Nm the contact parameters are largely different. These observations suggest that D-PDJ model is suitable for moderate non-linear systems (3 Nm and 5 Nm bolting torque) than non-linear systems (1 Nm bolting torque). The effect of excitation amplitude is studied with exciting the test structure with a random white noise excitation using an electrodynamic shaker. Good match is obtained for the FRF-mobility between the experiment and D-PDJ simulation for different excitation amplitudes. The contact pair effect is studied by fastening in-between the two structural beams a copper-prepreg-copper laminate plate. Two sets of experiments are performed with laminate double layered beam structure - first EMA in conjecture with varying bolting torque and second random excitation experiment. Same contact parameters were used for 1 Nm, 3 Nm and 5 Nm bolting torque for laminate double beam structure. Although the results show good match for 3 Nm and 5 Nm bolting torque in comparison to 1 Nm, the bolting torque of 1 Nm (for M6 bolt) is not relevant for practical cases. This reconfirms that the D-PDJ model predicts dynamic behaviour of structures experiencing moderate non-linearity to good accuracy, also with identical choice of parameters being used for all bolting loads.

Chapter 6

Model Verification - Prototype Structure

The previous chapter studied the cases that have predominant influence on the dynamical output of the test structures having contact interfaces. Comparison between experiment and D-PDJ model have shown good match for moderate non-linear systems with optimized choice of contact parameters. Practical applications need a precise and accurate prediction of the dynamical output, especially in the region of resonance. Two prototype structures are used in this section for model verification, which resemble a real automotive industrial product of Electronic Control Unit (ECU). The two ECU prototype structures I and II used for model verification are based on Engine control ECU and Airbag control ECU respectively. The motivation is to study the proposed D-PDJ model capability in predicting the dynamical characteristics of the complex structures resembling practical cases with significant accuracy and computational efficiency. Also, to identify the advantages of using D-PDJ model with respect to the conventional approaches used in commercial softwares. Figure 6.1 shows the conventional Engine ECU and Airbag ECU used in auto-mobiles.

(a) Engine ECU.

(b) Airbag ECU.

Figure 6.1: Two types of ECU's used in Industry, used in thesis for the prototype structure. References - www.bosch-mobility-solutions.us and de.bosch-automotive.com.

6.1 Prototype Structure I

Prototype structure I is a built up prototype of an Engine Electronic Control Unit (ECU), with an emphasis on modelling the ECU's having ideally large contact area and its influence on the dynamical characteristics. The large contact area in itself does not account for the complexity, but the contact pressure distribution over the contact area. As studied in previous chapter section 5.1, the contact pressure controlled through bolt loads has predominant influence on the structural resonance frequency. For a large contact area with contact pressure predominantly existing near the bolt region, a large part of the contact interface away from bolt centre experience very less magnitudes of contact pressure due to bolt loads. These negligible contact pressure value leads to the reduced contact stiffness and hence has influence on the resonance frequency. Also, the damping behaviour for such assembled structures is very difficult to be modelled accurately, as the local region experiences opening and closing of contacts with respect to time. A true behaviour can be modelled using transient simulations, wherein the change in the state of the contact can be captured with respect to time. However, an assumption of steady state behaviour for such excited modes motivates to identify the equivalent contact stiffness and damping, to evaluate approximately the resonance frequency and damping.

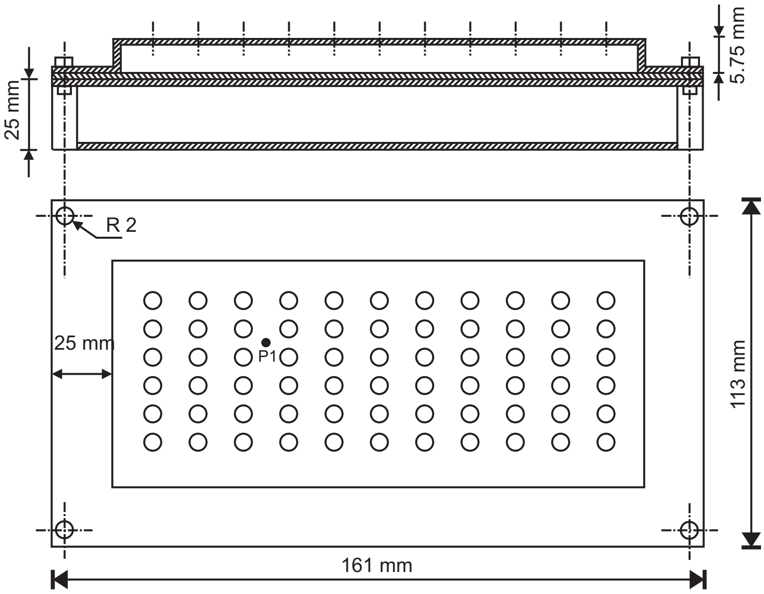

Figure 6.2: Assembled top and bottom view of the Engine ECU prototype structure with dimensions.

The Prototype structure I is an assembly of three parts, namely base-plate, plate and housing-cover. All the parts are made of Aluminium and are bolted together with M4 bolts, using 2 Nm bolting torque. The thickness of plate bolted between the base-plate and housing-cover is 1.6 mm. Once the individual parts are assembled together, only the top surfaces of the Baseplate and housing-cover can be measured. To establish an accurate experimental model for complete structure's measurement, it is proposed to drill holes on the baseplate to allow measurements on plate too. This allows a better and correct evaluation of damping, as the primary vibration modes of plate are also included. The prototype structure I with its dimension is shown in figure 6.2.

EMA of each individual part is performed and material properties in simulation are optimized to match the experimental results. Comparison for the modal frequency between EMA and simulation are shown for each individual part in tables 6.1, 6.2 and 6.3. It can be seen that the modal frequency results show good match for plate and base-plate with maximum error of 1.9 % and 2.2 % respectively. The modal frequency results of the housing-cover do not show good match, with maximum error related to torsion modes. The probable reason for the large deviation can be accounted for the non-uniform thickness due to the production process leading to unsymmetric model, while simulation models have a symmetric and uniform thickness structure. However, the important primary bending modes of the housing-cover show good match (modes 2 and 4, see table 6.3). It is also important to look at the modal damping ratio's obtained for each individual part, which shows almost constant values of 0.2-0.1 % .

Exp.	257	291	604	639	754	900	1140	1270	1650	1720	1920
Sim.	261	290	610	630	759	886	1140	1277	1632	1707	1902
Error (%)	1.9	0.5	0.9	1.4	0.7	1.6	0.0	0.6	1.1	0.8	0.9
ξ_{m}(%)	0.4	0.5	0.2	0.1	0.1	0.2	0.2	0.1	0.1	0.1	0.1

Table 6.1: Modal frequencies comparison between EMA and simulation for the plate structure with optimized values of Young's modulus E = 69 GPa, Poisons ratio $\nu = 0.31$ and mass density $\rho = 2740$ kg/m^3.

Exp.	368	902	1221	1329	1660	2158
Sim.	373	883	1211	1324	1662	2157
Error (%)	1.3	2.2	0.9	0.4	0.1	0.1
ξ_{m}(%)	0.3	0.1	0.2	0.1	0.1	0.1

Table 6.2: Modal frequencies comparison between EMA and simulation for base-plate structure with optimized values of Young's modulus $E = 72.5$ GPa, Poisons ratio $\nu = 0.31$ and mass density $\rho = 2740$ kg/m^3.

Exp.	310	993	1670	1823	2020
Sim.	373	1007	1728	1800	2011
Error (%)	2.9	1.4	3.5	1.1	0.4
ξ_{m}(%)	0.4	0.5	0.2	0.1	0.1

Table 6.3: Modal frequencies comparison between EMA and simulation for housing-cover structure with optimized values of Young's modulus $E = 60$ GPa, Poisons ratio $\nu = 0.31$ and mass density $\rho = 2740$ kg/m^3.

6.1.1 Modal Analysis : Prototype Structure I

There exists two main contact interfaces for Engine ECU prototype structure i.e. first contact between base-plate and plate and second contact between the plate, and housing-cover. The contact area of prior is larger than the latter, hence expected to have strong coupling between the plate and base-plate modes. Due to the large contact area interface, the modes related to this interface will have predominant contribution to system damping. The distribution of the contact stiffness density and the contact damping is shown in figure 6.3. The equivalent bolt force for M4 bolt is calculated based on equation (4.13). Large area of the contact zone leads to very less magnitudes of the stiffness, with localization of high stiffness near the bolt region. The damping distribution shows the predominance in region of micro-slip. Figure 6.4 shows the mode shapes of the prototype structure I with its modal frequency and damping from both simulation and experiment.

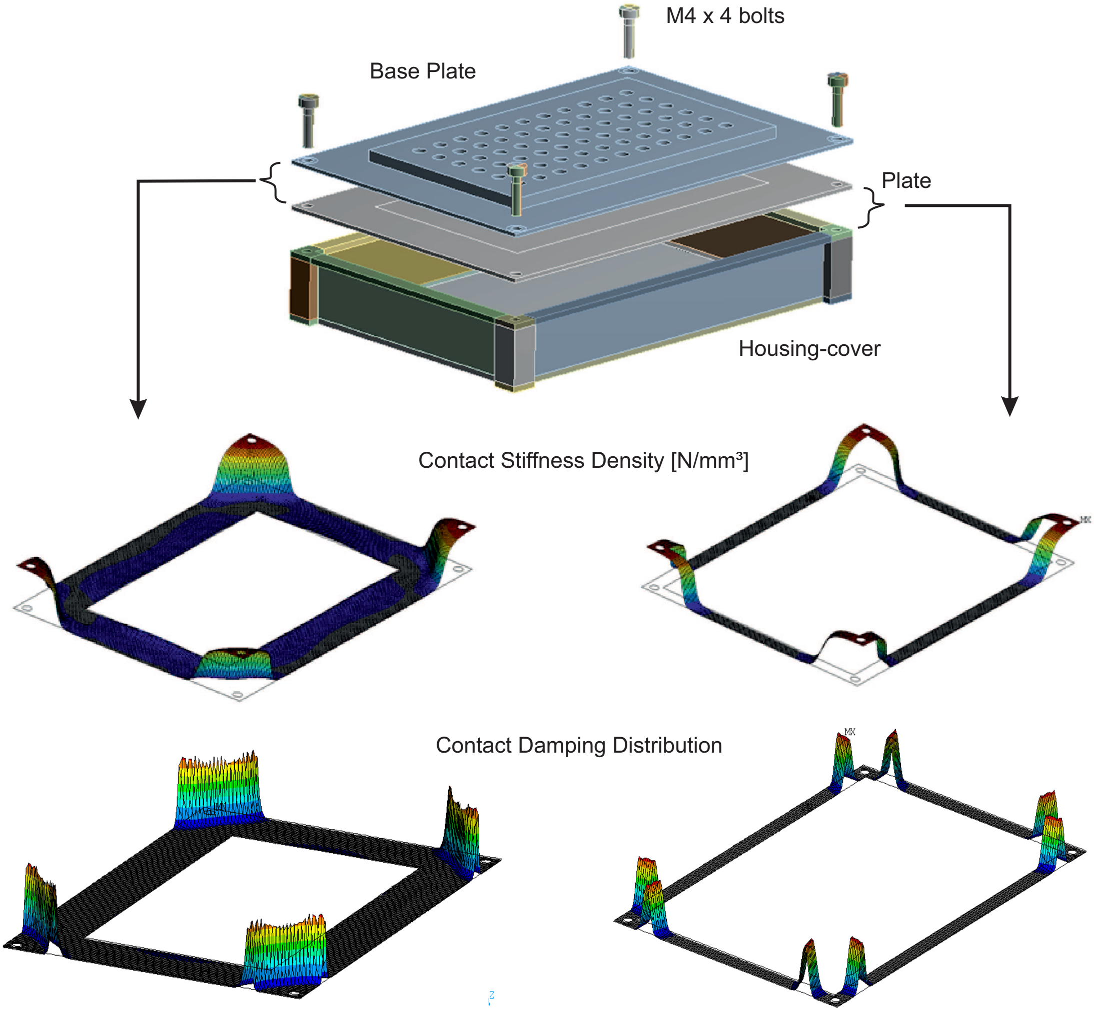

Figure 6.3: Contact stiffness density and damping distribution between the mating parts of an ECU prototype model with all parts made from Aluminium.

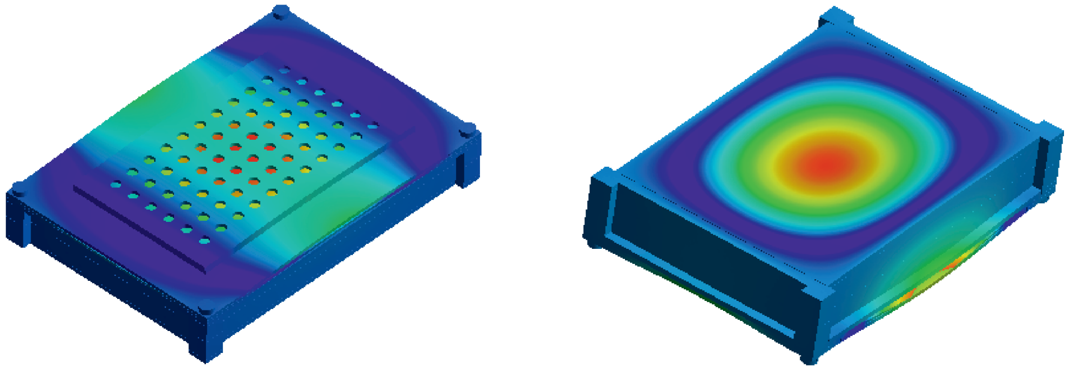

(a) Mode 1 - 1st Plate bending
Experiment : 640 Hz / 6.5 %
D-PDJ : 655 Hz / 5.5 %.

(b) Mode 2 - 1st Topcover bending
Experiment : 1070 Hz / 1.5 %
D-PDJ : 1082 Hz / 1.2 %.

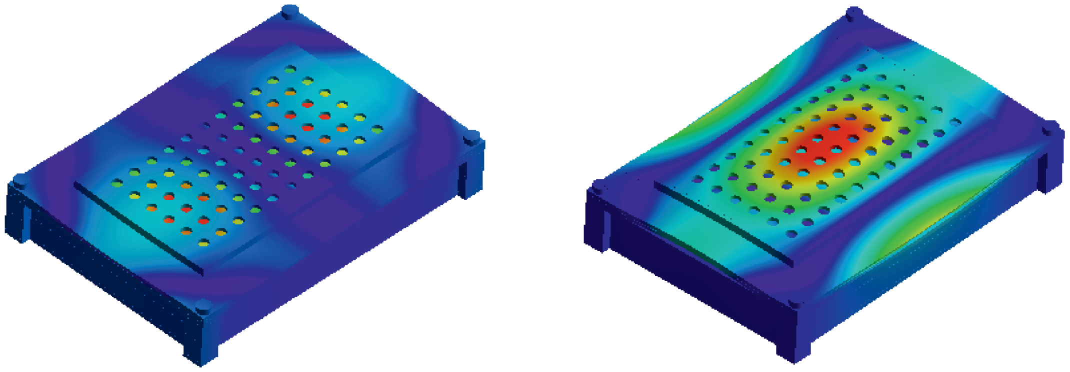

(c) Mode 3 - 2nd Plate bending
Experiment : 1236 Hz / 3.5 %
D-PDJ : 1229 Hz / 3.0 %.

(d) Mode 4 - 1st Baseplate bending
Experiment : 1410 Hz / 4.0 %
D-PDJ : 1392 Hz / 4.1 %.

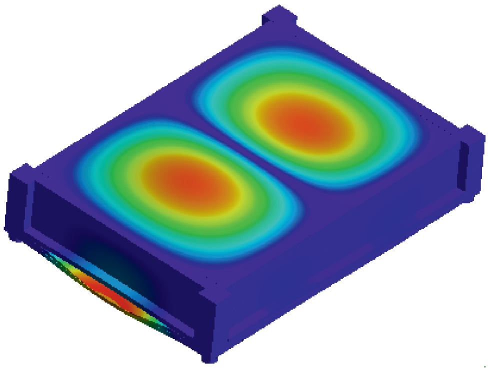

(e) Mode 5 - 2nd Topcover bending
Experiment : 1700 Hz / 0.8 %
D-PDJ : 1705 Hz / 0.9 %.

Figure 6.4: Comparison between EMA and D-PDJ simulation results for ECU prototype structure with respective mode shapes.
Contact parameters : $\lambda = 450$, $P_{\mathrm{N1}} = 1$, $\beta_0 = 0.83$, $P_{\mathrm{m}}^{\mathrm{loc}} = 1$, $\chi_{\mathrm{r}} = 5{,}0.1$.

A very good match between EMA and D-PDJ simulation for both modal frequency and modal damping ratio is obtained, as shown in figure 6.4 with their respective mode shapes of prototype structure I. The used contact parameters for D-PDJ simulation are mentioned in figure 6.4. Due to the milling-finishing process used to generate flat surfaces of individual part, the curvature parameter lies in range of 333 - 1000 , as discussed in section 4.4.3. The optimized values of the contact parameters governing the contact stiffness of the prototype structure I, curvature parameter $\lambda = 450$ and saturation pressure parameter $P_{\mathrm{N1}} = 1$ are obtained from iterations of the simulation model to match experiment modal frequency. The coupling factor $\beta_0 = 0.82$ is calculated for same materials (Aluminium) in contact based on equation (4.22). The values of these parameters are taken as same for both the contact interfaces i.e. the contact interface between the base-plate and plate, and the contact interface between the plate and the housing-cover.

The minimum damping value obtained for prototype structure I is 0.8 % for the fifth mode, which is quiet large in comparison to the material damping values obtained from EMA of each individual part (see tables 6.1, 6.2 and 6.3). This clearly shows that the predominance of the damping is due to contact than inherent material damping, justifying the very first assumption taken at initial steps of contact modelling for vibration problems. The large modal damping ratio's are obtained for the modes associated with plate and base-plate bending modes, while the modal damping ratio associated with the bending modes of the housing-cover are significantly low. The damping parameters are different for the two contact interfaces due variation in the pressure distribution at the two contact interfaces. As the experiment damping values are in range of 0.8 - 6.5 %, these large damping values in comparison to doubled layered beam structure indicate that the damping scaling factor will have larger value than the value used for double layered beam. Based on iterations of simulation model, the damping-scaling factor χ_{r} of 5 is optimal value for the contact interface with large contact area i.e. for the contact interface between the base-plate and the plate structure. The damping scaling factor χ_{r} of 0.1 is used for smaller contact interface i.e the contact interface between the plate and the cover, to have significant match between the experiment and simulation results. This proves the predominant influence on the damping due to the large contact areas.

Mode	Eigenfrequency [Hz]			
	EMA	D-PDJ	Bonded	Frictional
Mode 1	640	655	928	674
Mode 3	1236	1229	1522	1220

Table 6.4: Eigenfrequency comparison between EMA and different simulation models of plate first and secondary modes of the Engine ECU prototype.

The primary bending modes of the plate structure (modes 1 and 3) are of most importance in the design of Engine ECU's, as many important electronic components for operations of ECU are located on the PCB plate. All these electronic components get excited with the plate modes and require accurate estimation of the resonance frequency and modal damping ratio for the fatigue calculations. The present modelling approach in the commercial software like Ansys v14 is to perform a pre-stress modal analysis with modelling of contacts as bonded or frictional contact. The bonded contact refers ideally to fixed contact between the surfaces, while frictional contact is the Coulomb friction model. Comparisons between the D-PDJ and conventional methods are performed with respect to the accuracy in predicting the modal frequencies and the computational time efficiency. Table 6.4 shows the comparisons of simulation models with respect to EMA results of plate bending modes of the prototype structure I. It is clearly evident that the D-PDJ shows better results in terms of predicting the modal frequencies. Also, the conventional models can give the modal frequency and damping values only for the cases involving material damping, while D-PDJ gives output of global modal damping ratio as the combination of both material and contact damping. Table 6.5 shows that the use of D-PDJ even improves the computational time efficiency, which comes due to local-linearity in comparison to full non-linear frictional analysis.

Test Structure	Conventional Model	D-PDJ Model
Double beam	4500 sec*	3000 sec
ECU Prototype	8000 sec	5500 sec

Table 6.5: Comparison of computational time between commercial FEM and D-PDJ. (*Random analysis not possible with frictional contacts in Ansys).

6.2 Prototype Structure II

Prototype structure II is motivated towards depicting an Airbag ECU structure. The Airbag ECU's have sensors fixed on Printed Circuit Board (PCB) to detect the situations of crash and accordingly operate the functionality of deploying Airbags. Hence, required is a precise and accurate evaluation of damping, so as to estimate whether the threshold values are reached or not. Used in prototype structure II is an assembly for PCB plate and base-plate, but the housing cover is not taken. The housing-cover of an Airbag ECU is made of plastics and hence requires non-linear material models for simulations, which is out of scope of present work. The Airbag ECU is tested in vibrations using electrodynamic shakers with harmonic sweep or random excitation according to field test profiles. Similarly here, the prototype structure is fastened to shaker using an large mass support structure and is excited with the equivalent excitation profile of the field conditions. The pictorial representation of the prototype structure II and its lab testing set-up is shown in figure 6.9. This section is divided into two phases. The first phase deals with modelling of individual assembly i.e. assembled structure of PCB - baseplate and assembled structure of baseplate - support structure. The second phase deals with modelling the complete assembled prototype structure for harmonic sweep excitation in vibration lab testing environment.

6.2.1 Part Assembled Structures

This sub-section deals with the modelling of part assemblies to independently study the influence from contacts and material on global dynamic behaviour. The first part assembly is the assembly of base-plate and PCB plate structure having less contact area of contact interface, hence concentrating on material modelling. The second part assembly is the assembly between the base-plate and the support structure with considerable contact area, hence concentrating on contact modelling.

PCB Plate Structure

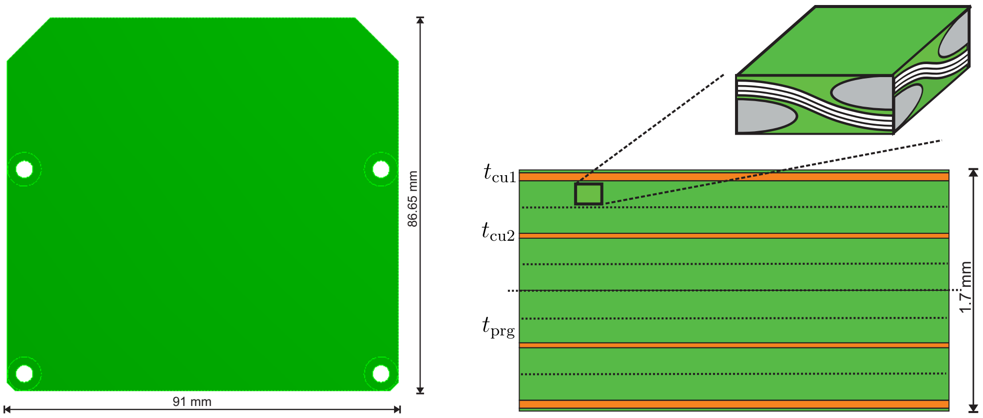

(a) Prototype of PCB plate. (b) PCB plate stack-up.

Figure 6.5: Dimensions and stack-up layout of an equivalent Airbag ECU's PCB plate having 8 layers of prepreg and 4 layers of copper. Thickness : $t_{\mathrm{cu1}} = 55$ μm, $t_{\mathrm{cu2}} = 35$ μm and $t_{\mathrm{preg}} = 185$ μm.

The PCB plate (like copper-prepreg-copper plate, see section 5.3) is laminate plate of copper and prepreg layers. PCB's used in ECU's have a non-homogeneous distribution of copper content for each of the copper layer stacked in the PCB plate. A simplified model of PCB with assumption of homogeneous distribution of copper trace is taken for simulation. Also, the PCB plate has many minute sized holes to solder various electronic components, but in the simulation model these holes are eliminated to avoid efforts on volume meshing. Figure 6.5 shows the stack-up layout cross-section of PCB plate having 4 layers of copper sheet and 8 layers of prepreg. The PCB plate is modelled using classical laminate theory, similar to the approach used for modelling copper-prepreg-copper plate in previous chapter section 5.3. The elastic material constants for both prepreg and copper layers are obtained by model updating the PCB structure with respect to the modal frequency from experiment modal analysis. The comparison of EMA and simulation results for modal frequencies of PCB plate with optimized material-elastic properties are shown in table 6.6.

Exp.	435	701	866	1170	1200	2100	2130
Sim.	436	687	892	1163	1196	2085	2112
Error (%)	0.1	2.0	2.9	0.6	0.3	0.7	0.8
ξ_m (%)	0.3	0.2	0.5	0.4	0.4	0.4	0.3

Table 6.6: Modal frequencies comparison between EMA and simulation for the PCB plate structure.
Prepreg : $E_x/E_y/G_{xy} = 12.5/14.5/2.5$ GPa, $\nu_{xy} = 0.15$ and $\rho_{preg} = 1650\,\text{kg/m}^3$;
Copper layer : $E = 85$ GPa, $\nu = 0.34$, $\rho_{cu} = 8850$ kg/m^3.

A good match of modal frequencies between the simulation and EMA is obtained with maximum error of 2.9 % and mean error of 1 %. The modal damping ratios measured from the EMA are approximately constant value with a mean value of 0.35 %.

Part Assembly - Baseplate and PCB Plate

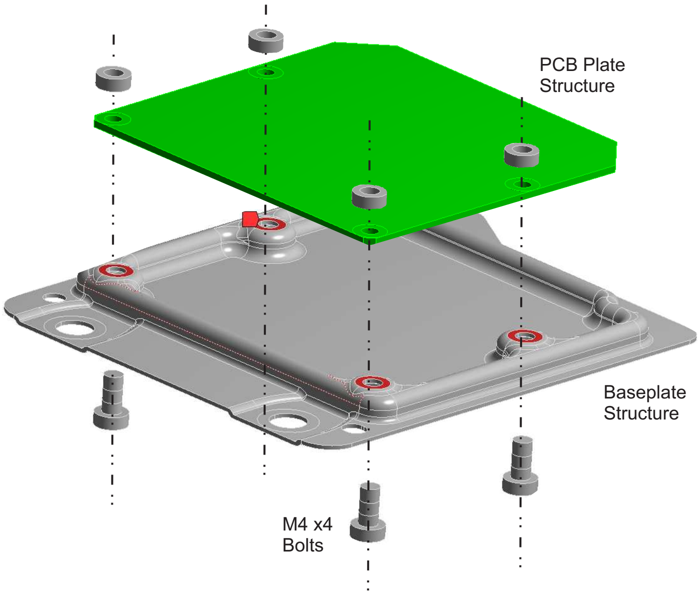

Figure 6.6: Exploded view - assembly of baseplate and PCB plate with the contact interface area shown with highlighted region.

The first part assembly of the prototype structure II is the assembled structure of baseplate and PCB plate. The baseplate is a thin sheet metal structure having thickness of 1 mm. The elastic properties of baseplate taken for the simulation are : Young's modulus $E = 210$ GPa, poisson's ratio $\nu = 0.31$ and mass density $\rho = 7850$ kg/m^3. With known PCB plate material properties from previous section, the built-up assembled structure of PCB plate and baseplate can be simulated and compared with results of EMA. The fastening of baseplate with PCB is accomplished using M4 bolts with 2 Nm bolting torque. Figure 6.6 shows both the exploded view of the baseplate and PCB plate assembly. The contact area between the baseplate and PCB plate is small, with large magnitude of bolting loads.

This suggests no predominant effects of damping from the contacts. The comparison of modal frequencies between EMA and the D-PDJ simulation are presented in table 6.7. A very good match is observed till 2 kHz, with maximum error of 3.5 % for second mode and approximate mean error of 1.2 %. The second mode is a torsion mode, which is not a critical mode as it does not get excited for the prototype structure when fastened on shaker table or for the case of direct mounting in auto-mobiles. The modal damping ratios obtained for the assembly is almost similar to the values of modal damping obtained for the PCB plate itself. Thus, confirms no significant predominance of contacts on global damping due to very less contact area and large magnitude of bolting load.

Exp.	533	729	826	1090	1180	1330	1540	1670	1770	1990	2040
Sim.	533	704	830	1084	1194	1348	1521	1681	1798	2010	2075
Error (%)	0.0	3.5	0.6	0.5	1.2	0.7	1.4	0.6	1.6	1.0	1.9
ξ_m (%)	0.5	0.3	0.6	0.4	0.3	0.3	0.3	0.3	0.4	0.2	0.3

Table 6.7: Modal frequencies comparison between EMA and simulation for the assembly of baseplate-PCB plate structure.

Part Assembly - Baseplate and Adapter Plate

The second assembly structure of the prototype structure II is the fastening of the baseplate on the top surface of support structure. The base excitation is given to the bottom of the support structure using an electrodynamic shaker. The baseplate is fastened to support structure using M8 bolts with 8 Nm bolting torque. The exploded view of the part assembly can be seen in the figure 6.7. The contact area is considerable large than previous part assembly and hence the contact modelling plays significant role here. However, with use of very high bolt load, the non-linear effects are minimal but still required is the estimation of contact stiffness and damping to a considerable accuracy. D-PDJ model is used for performing a modal super-position harmonic analysis for base excitation. The experiment is performed with sine sweep excitation in frequency range of 100-2100 Hz, using constant amplitude of 1 m/s^2. The comparison between experiment and D-PDJ simulation results are done for measured transmissiblity at the corner point on the baseplate, see figure 6.7. The measurement point has the maximum amplitudes of vibration and captures all modes in required frequency range of interest.

A good match of transmissiblity is achieved between the experiment and D-PDJ simulation for the assembled structure of baseplate and support structure, see figure 6.8. The contact parameters used for the D-PDJ simulation are listed in figure 6.8. The contact parameters are obtained by iterations of the simulation model to match the results of experiment, as discussed in chapter 5- section 5.1.2. The coupling factor (β_0) value of 1.6 is calculated for the contact pairing of stainless steel (baseplate) and aluminium (support structure) materials, see equation (4.21). As mentioned before, due to high bolt loads of 8 Nm, the contact pressure too is very high with almost uniform pressure distribution.

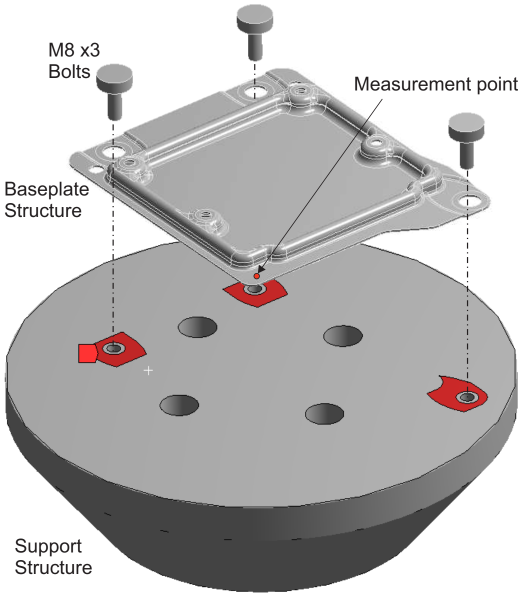

Figure 6.7: Exploded view - assembly of baseplate and support structure with region of contact interface shown as highlighted region. The measurement point is used for comparing results between experiment and simulation.

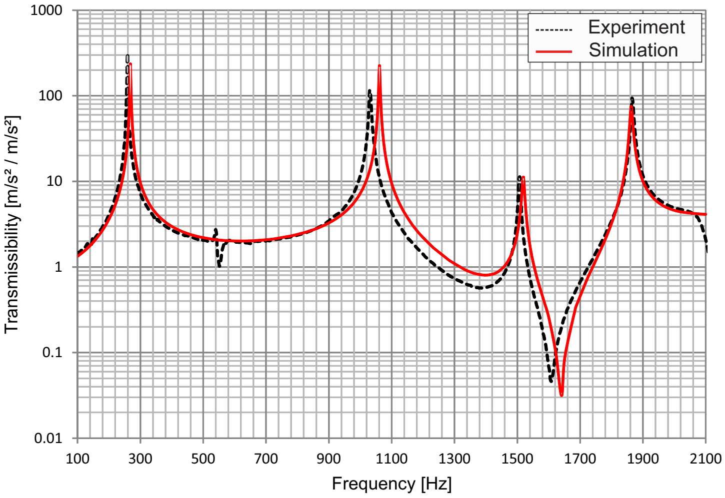

Figure 6.8: Comparison of transmissibilty between experiment and D-PDJ simulation for baseplate-support structure assembly in base excitation set-up. Contact parameter used : $\lambda = 4000$, $P_{\mathrm{N1}} = 2$, $\beta_0 = 1.6$, $\chi_r = 2$, $P_{\mathrm{m}}^{\mathrm{loc}} = 10$.

The uniform large contact pressure leads to shifting of the location of the maximum dissipation away from regions near the bolt center (having very high pressure) to regions far away from bolt centre (having very low pressure). Optimized value of $P_{\mathrm{m}}^{\mathrm{loc}} = 10$ is used, which means that the maximum contact damping occurs at a pressure equal to 0.1 times the mean of the contact pressure over interface. The material properties and contact parameters used for the two sub-assembly units will be directly used in the following section to model the complete assembly of assembled prototype structure II.

6.2.2 Harmonic Analysis - Prototype Structure II

The study on part assemblies provided the required material and contact parameters for the complete assembled prototype structure II, such that the dynamical effects are modelled by assimilating the effects from material and contact modelling. The experimental set-up and the assembled model for simulation are shown in figure 6.9. The electrodynamic shaker is used to excite at the bottom of the support structure with a sine-sweep profile of constant amplitude of 1 m/s^2 in frequency range of 100-2100 Hz.

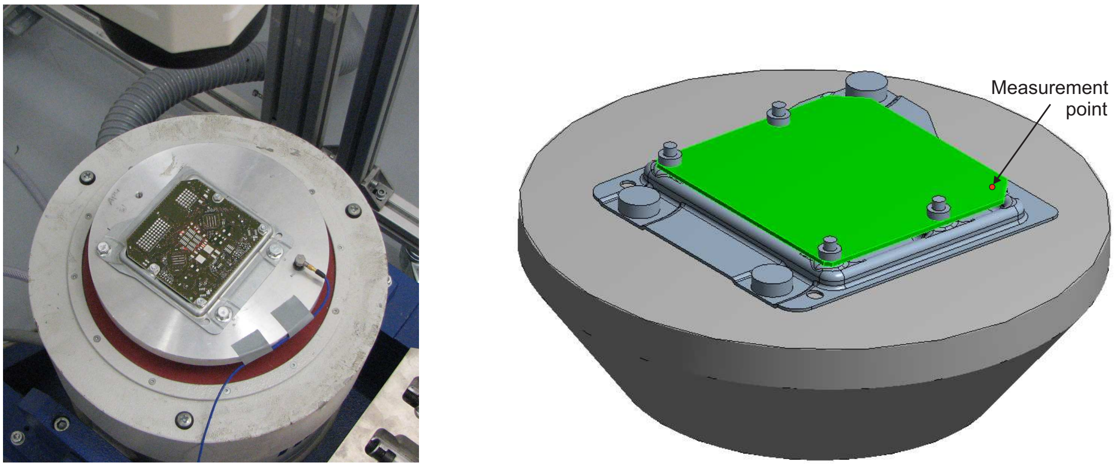

(a) Experimental set-up (b) Simulation model

Figure 6.9: Prototype structure II set-up for the verification of dynamical behaviour under sine-sweep base excitation. A point on PCB plate is used for comparison between experiment and D-PDJ simulation results.

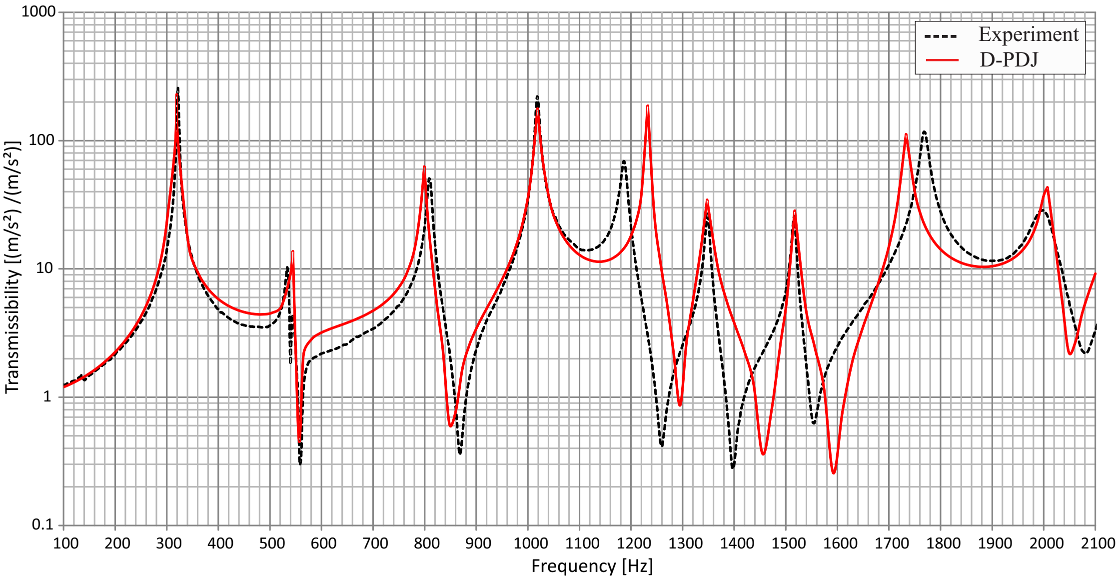

Figure 6.10: Comparison of experiment and D-PDJ simulation transmissibility for sine sweep excitation amplitude of 1 m/s^2.

Figure 6.10 shows the comparison between the experiment and simulation results for the transmissibility frequency spectrum for a measurement point on the PCB plate. Very good match between the experiment and D-PDJ model is obtained, especially until 1 kHz. The maximum deviation for both resonance frequency and amplitude of transmissbility is observed near 1200 Hz. Leaving this particular deviation, all other resonance conservatively show significantly good match. The desired signal frequency range for sensors operations are conventionally under 1 kHz and hence, it is concluded for prototype structure modelled using D-PDJ model fulfils the required conditions to be used for the industrial applications.

Summary

This chapter shows the capability of the proposed D-PDJ model in predicting the vibrational behaviour of large models. Two prototypes of Electronic Control Units were used - Engine ECU and Airbag ECU. The first prototype structure concentrates on study of a system having large contact area while the second prototype describes a system having the assembly of different materials. Both the prototype models show good match between the simulation and experimental results. It is observed that not only the accuracy of the results but even the computational time is enhanced with use of the D-PDJ model in comparison to conventional techniques used in commercial software. Hence, D-PDJ model can be used in early and successive stages of designing industrial products, with considerable accuracy in predicting dynamical behaviour and simultaneously being computationally efficient in comparison to conventional numerical models.

Chapter 7

Conclusion and Outlook

Built-up structures use various joints to assemble different parts, which induce the local non-linearities at the joints. The local non-linearities have influence on the global dynamical characteristics - resonance frequency and amplitude of vibration. The dynamical modelling and design of structure requires better predictions for the influence of local non-linearities on global dynamical behaviour. Although the increasing computational capabilities and developments in numerical models have brought in significant advantages, emphasis is still required to have models applicable for large and complex structures with improved computational time efficiency. The proposed model in this thesis encounters these requirements with quantitative experimental validations.

Conclusion

Numerical implementation of non-linear contact laws is conventionally done in time domain representation, which gives good approximate solutions for non-liner behaviour. But the time domain representation is not feasible for large and complex structures due to large computational time and difficulties in numerical convergence. Alternate approaches of frequency domain representation based on the family of Harmonic Balance Method (HBM) improves computational time but their implementation has broadly been restricted to narrow band periodic excitations. Thus, required is a model which not only captures the non-linear effects but also posses the qualities of ease in implementation, computational efficiency and is feasible for large systems under broad band excitations.

The new modelling approach is based on the modelling of contact interfaces as the combination of many peak to peak asperity contact spots. The equivalent contact stiffness and damping - varying at each local point defines a non-homogeneous description while preserving the linear definition at local level. This enables the global system to capture the non-linear behaviour based on non-homogeneity, while the local linear definition retains the advantageous of linear system. The model is divided into two phases- quasi-static loading step for non-linear normal contact definition and dynamic loading step to characterize equivalent contact stiffness and damping.

To model the non-linear behaviour of normal contacts, an exponential-pressure penetration law based on the modified Greenwood and Williamson model is used. Modification relates to the division of regions into non-linear and linear based on saturation pressure limit, to enable convergence for large loadings. The two important parameters used in the formulation are- the curvature parameter governing the non-linear exponential behaviour and the saturation pressure governing the switching of non-linear behaviour to linear behaviour. The contact interface is discretized using discrete 3D Kelvin-Voigt elements. The equivalent normal contact stiffness is calculated as the gradient of the contact pressure. The tangential contact stiffness is calculated by scaling the normal contact stiffness with a coupling factor. The coupling factor is dependent on the composite shear and elastic modulus of materials in contact.

The equivalent contact damping definition is based on numerical investigation to study the dissipation profile at contact interfaces. Modified Dahl friction model is used to obtain the dissipation profile over contact interface of a beam fasten with a bolted joint. The important conclusions drawn from numerical investigations are:

- the dissipation is maximum in-between the regions experiencing high pressure (stick region) and low pressure (slip region) , i.e in the icro-slip region
- the shape of the dissipation curve over contact interface length can be approximated using statistical distribution functions, and
- the position of maximum dissipation shifts with variations in bolting loads or excitation amplitudes.

The dissipation profile motivates the use of a Rayleigh distribution function to define the damping distribution at the interface. The parameters used in this formulation are - damping location parameter governing the position of maximum dissipation and the scaling parameter governing the magnitudes of dissipation. The model now possessing both the definition of the local contact stiffness and damping, is referred as Damped Pressure Dependent Joint (D-PDJ) model. Quantitative experimental validations are required to study the influencing factors and test the D-PDJ's model capability in predicting the dynamical behaviour.

The base test structure used is a double layered stainless-steel beam fastened with 4 M6 bolts. The parametric study is performed for three influencing factors - effect of bolting torque, effect of excitation and effect of coupling pair. The bolting torques influences the contact pressure distribution, the excitation amplitude influences the relative displacement and the coupling pair influences of the coupling between normal and tangential tractions. The effect of bolting torques is studied with variation in bolting torques of 1 Nm, 3 Nm and 5 Nm, defining the system to be non-linear, moderate non-linear and slight non-linear respectively. The important findings are - with increase in bolting torques the modal frequency increases and the modal damping decreases. However, these observations are associated to only out of plane modes while the in-plane modes do not show any influence due to bolting loads. This concludes that the effect of contact local non-linearity influences only certain modes of vibration and not all global modes of vibration. The optimized contact parameters used for the 3 Nm and 5 Nm cases are almost similar than the ones used for 1 Nm case. The D-PDJ model showed good match for 3 Nm and 5 Nm than 1 Nm bolting torques. Thus concluding that the proposed model is suitable for the moderate non-linear systems than highly non-linear systems. The effect of excitation amplitude for varying Force controlled PSD (FPSD) inputs from electro-dynamic shaker is validated for 3 Nm bolting torque. It is observed here, that with increase in the excitation amplitudes, the resonance frequency decreases while the damping ratio increases. The D-PDJ showed good comparisons with experimental results and confirms the applicability of proposed D-PDJ model for cases of random excitation. The effect of coupling pair is investigated by fastening a copper-prepreg-copper plate between the two beams of base test structure. The EMA results comparison with D-PDJ model is performed with use of same contact parameters for all three cases of bolting loads (1 Nm, 3 Nm and 5 Nm). A good match between experiment and simulation results for all cases is obtained, with the moderate non-linear systems (3 Nm and 5 Nm) having better accuracy than the non-linear system (1 Nm). Bolting torque of 1 Nm for M6 bolts is not applicable for practical purposes, as this does not provide sufficient tightening under dynamic excitation. Further on, the laminate beam test structure showed good match between experimental and simulation results for force controlled PSD excitations too. All above validations with base test structure concludes that the D-PDJ predicts the system behaviour with good accuracy for the systems possessing moderate non-linearity and can be also be used to predict results for the systems excited with random inputs.

The prototype structures are used to verify the proposed D-PDJ model's capability to capture the dynamical behaviour of large and complex structures like ECU's. The first prototype was examined for resembling an Engine ECU having large contact area with localized pressure distribution neat bolt regions. The EMA results when compared to D-PDJ model showed very good results till 2 kHz, with the results of the modal damping highly appreciable. The result's accuracy and computational time efficiency have proved to be significantly better than the commercial software results. The second prototype structure verifies the use of model having combination of material and contact non-linearities for prototype structure resembling Airbag ECU. The result when compared for the transmissibility plot showed good match between the base excited structure in experiments to the D-PDJ simulation.

Hence, D-PDJ model can be used in early and successive stages of designing industrial products, with considerable accuracy in predicting dynamical behaviour and simultaneously being computationally efficient in comparison to conventional numerical models. Although the investigations are done for structures having bolted joints, the D-PDJ model can be used for other joints too wherein considerable contact pressure distribution exists.

Outlook

The present D-PDJ model has been developed for modal-superposition analysis, which can be further extended to full transient domain analysis for cases involving shock and drop tests. This will also extend the scope of redefining the formulations of contact stiffness and damping with inclusion of time varying excitation amplitudes. To achieve stability for large relative displacements in transient simulation, a hybrid discretization can be used by switching from point-to-point coupling definition to surface-to-surface coupling. A possible solution can be use of zero-thickness elements.

There exists the vibration modes, which are influenced through material non-linearity or through contact non-linearity or through combined material-contact non-linearities. The other extension that can be included is a detailed material modelling of the ortho-tropic materials with orientation and directional based damping definition in conjecture with the contact damping. The complexity will be increased while depicting the dynamical behaviour of system under superimposed temperature loading for such systems.

The experimental investigations need to be more comprehensive in estimation of the local and global non-linearities. An experimental set-up needs to be designed such that the varying dissipation profile over contact interface can be visualized with change in operational parameters like contact pressure, excitation amplitude, coupling material and temperature. The stress relaxation for long durations of loading can be measured experimentally and corresponding effects can be incorporated in simulations.

Appendix A

Rod - 1D Element

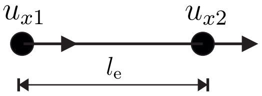

$$\boldsymbol{M}_\mathrm{e} = \begin{bmatrix} 2M_\mathrm{r} & M_\mathrm{r} \\ M_\mathrm{r} & 2M_\mathrm{r} \end{bmatrix} \qquad \boldsymbol{K}_\mathrm{e} = \begin{bmatrix} K_\mathrm{r} & -K_\mathrm{r} \\ -K_\mathrm{r} & K_\mathrm{r} \end{bmatrix} \tag{A.1}$$

wherein, $M_\mathrm{r} = \dfrac{\rho A_\mathrm{e} l_\mathrm{e}}{6}$ and $K_\mathrm{r} = \dfrac{EA_\mathrm{e}}{l_\mathrm{e}}$. Here ρ, E, A_e and l_e are the density, Young's modulus, area of cross-section and length of the element respectively.

Euler Beam - 3D Element

$$\boldsymbol{M}_\mathrm{e} = \begin{bmatrix} 2M_\mathrm{r} & 0 & 0 & M_\mathrm{r} & 0 & 0 \\ 0 & 156M_\mathrm{b} & 22l_\mathrm{e}M_\mathrm{b} & 0 & 54M_\mathrm{b} & -13l_\mathrm{e}M_\mathrm{b} \\ 0 & 22l_\mathrm{e}M_\mathrm{b} & 4l_\mathrm{e}^2M_\mathrm{b} & 0 & 13l_\mathrm{e}M_\mathrm{b} & -3l_\mathrm{e}^2M_\mathrm{b} \\ M_\mathrm{r} & 0 & 0 & 2M_\mathrm{r} & 0 & 0 \\ 0 & 54M_\mathrm{b} & 13l_\mathrm{e}M_\mathrm{b} & 0 & 156M_\mathrm{b} & -22l_\mathrm{e}M_\mathrm{b} \\ 0 & -13l_\mathrm{e}M_\mathrm{b} & -3l_\mathrm{e}^2M_\mathrm{b} & 0 & -22l_\mathrm{e}M_\mathrm{b} & 4l_\mathrm{e}^2M_\mathrm{b} \end{bmatrix}; \tag{A.2}$$

$$\boldsymbol{K}_\mathrm{e} = \begin{bmatrix} K_\mathrm{r} & 0 & 0 & -K_\mathrm{r} & 0 & 0 \\ 0 & 12K_\mathrm{b} & 6l_\mathrm{e}K_\mathrm{b} & 0 & -12K_\mathrm{b} & 6l_\mathrm{e}K_\mathrm{b} \\ 0 & 6l_\mathrm{e}K_\mathrm{b} & 4l_\mathrm{e}^2K_\mathrm{b} & 0 & -6l_\mathrm{e}K_\mathrm{b} & 2l_\mathrm{e}^2K_\mathrm{b} \\ -K_\mathrm{r} & 0 & 0 & K_\mathrm{r} & 0 & 0 \\ 0 & -12K_\mathrm{b} & -6l_\mathrm{e}K_\mathrm{b} & 0 & 12K_\mathrm{b} & -6l_\mathrm{e}K_\mathrm{b} \\ 0 & 6l_\mathrm{e}K_\mathrm{b} & 2l_\mathrm{e}^2K_\mathrm{b} & 0 & -6l_\mathrm{e}K_\mathrm{b} & 4l_\mathrm{e}^2K_\mathrm{b} \end{bmatrix} \tag{A.3}$$

wherein, $M_\mathrm{b} = \dfrac{\rho A_\mathrm{e} l_\mathrm{e}}{420}$ and $K_\mathrm{b} = \dfrac{EI_\mathrm{e}}{l_\mathrm{e}^3}$, with I_e is the area moment of inertia.

Solid hexa - 3D Element

Iso-paramteric shape functions

$$
\begin{aligned}
N_1^{(e)} &= \frac{1}{8}(1-\xi_1)(1-\xi_2)(1-\xi_3) & N_2^{(e)} &= \frac{1}{8}(1+\xi_1)(1-\xi_2)(1-\xi_3) \\
N_3^{(e)} &= \frac{1}{8}(1+\xi_1)(1+\xi_2)(1-\xi_3) & N_4^{(e)} &= \frac{1}{8}(1-\xi_1)(1+\xi_2)(1-\xi_3) \\
N_5^{(e)} &= \frac{1}{8}(1-\xi_1)(1-\xi_2)(1+\xi_3) & N_6^{(e)} &= \frac{1}{8}(1+\xi_1)(1-\xi_2)(1+\xi_3) \\
N_7^{(e)} &= \frac{1}{8}(1+\xi_1)(1+\xi_2)(1+\xi_3) & N_8^{(e)} &= \frac{1}{8}(1-\xi_!)(1+\xi_2)(1+\xi_3)
\end{aligned}
\tag{A.4}
$$

where, ξ_1, ξ_2 and ξ_3 are the iso-parametric co-ordinates defined in limits [-1,1].

$$
\boldsymbol{M}_{\mathrm{e}} = \int_{\Omega^{(e)}} \boldsymbol{N} \rho \boldsymbol{N}^T \partial \Omega \tag{A.5}
$$

$$
\boldsymbol{K}_{\mathrm{e}} = \int_{\Omega^{(e)}} \boldsymbol{B}^T \boldsymbol{C} \boldsymbol{B} \partial \Omega \tag{A.6}
$$

where,

$$
\boldsymbol{B} = \begin{bmatrix}
\frac{\partial}{\partial x} & 0 & 0 \\
0 & \frac{\partial}{\partial y} & 0 \\
0 & 0 & \frac{\partial}{\partial y} \\
\frac{\partial}{\partial y} & \frac{\partial}{\partial x} & 0 \\
0 & \frac{\partial}{\partial z} & \frac{\partial}{\partial y} \\
\frac{\partial}{\partial z} & 0 & \frac{\partial}{\partial x}
\end{bmatrix}
\begin{bmatrix}
\boldsymbol{N} & 0 & 0 \\
0 & \boldsymbol{N} & 0 \\
0 & 0 & \boldsymbol{N}
\end{bmatrix}
=
\begin{bmatrix}
\boldsymbol{N}_x & 0 & 0 \\
0 & \boldsymbol{N}_y & 0 \\
0 & 0 & \boldsymbol{N}_z \\
\boldsymbol{N}_y & \boldsymbol{N}_x & 0 \\
0 & \boldsymbol{N}_z & \boldsymbol{N}_y \\
\boldsymbol{N}_z & 0 & \boldsymbol{N}_x
\end{bmatrix}
\tag{A.7}
$$

such that

$$
\boldsymbol{N} = \begin{bmatrix} N_1^{(e)} & \dots & N_8^{(e)} \end{bmatrix} \qquad
\boldsymbol{N}_x = \begin{bmatrix} \frac{\partial N_1^{(e)}}{\partial x^{(e)}} & \dots & \frac{\partial N_8^{(e)}}{\partial x^{(e)}} \end{bmatrix}
\tag{A.8}
$$

$$
\boldsymbol{N}_y = \begin{bmatrix} \frac{\partial N_1^{(e)}}{\partial y^{(e)}} & \dots & \frac{\partial N_8^{(e)}}{\partial y^{(e)}} \end{bmatrix} \qquad
\boldsymbol{N}_z = \begin{bmatrix} \frac{\partial N_1^{(e)}}{\partial z^{(e)}} & \dots & \frac{\partial N_8^{(e)}}{\partial z^{(e)}} \end{bmatrix}
$$

Contact dissipation - 3D Solid beam

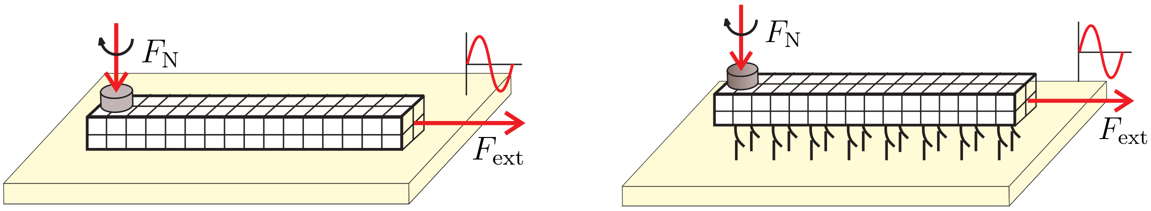

(a) 3D solid beam with bolted joint.

(b) Dahl brush element at contact interface.

Figure A.1: Set-up of a bolted end 3D solid continuum beam model having contact with a rigid surface, wherein the contact interface is modelled using modified Dahl formulation. Harmonic excitation is applied at opposite end of bolted joint.

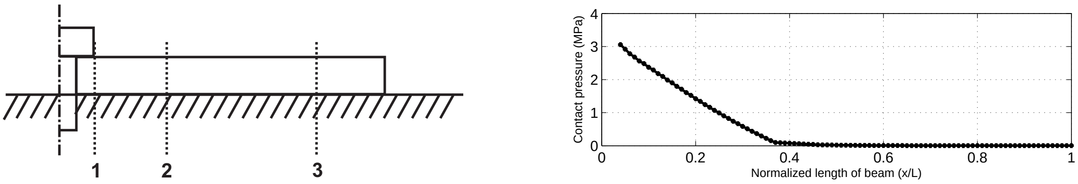

(a) Positions on beam.

(b) Contact pressure over beam length.

Figure A.2: Different positions chosen over beam length based on the contact pressure distribution over beam length.

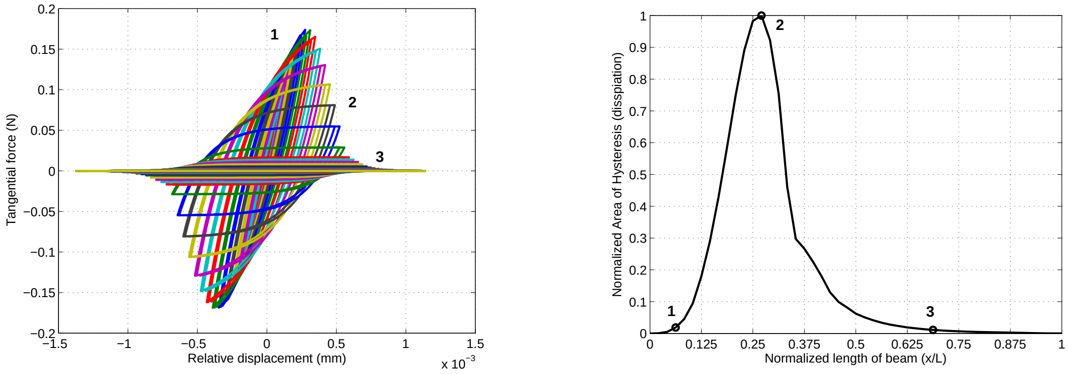

(a) Tangential force vs. relative displacement for various points at the contact interface

(b) Normalized Dissipation vs. location at the contact interface over the beam length

Figure A.3: Hysteresis shapes at the different local nodal points of the contact interface (left). The normalized dissipation loss due to contacts over the length of beam (right).

Contact dissipation - Double layered rod

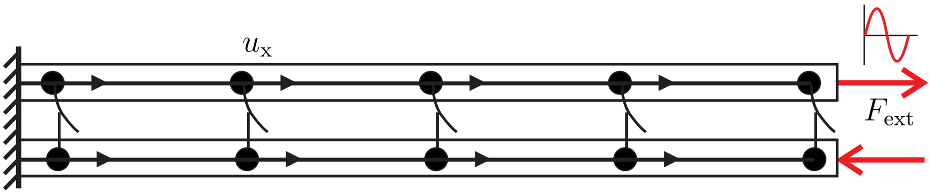

Figure A.4: Double layered rod structure set-up with fixed ends. The harmonic excitations applied in opposite directions for each rod at the free end.

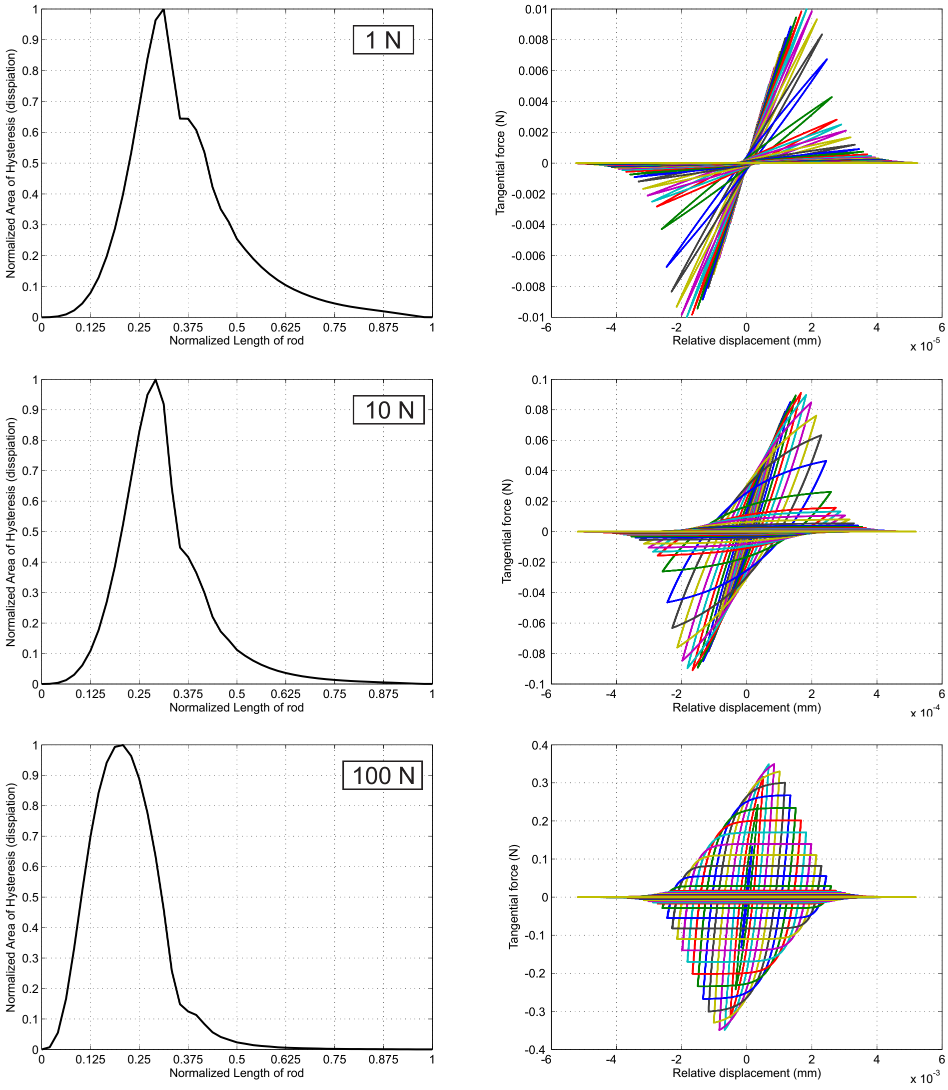

Figure A.5: The hysteresis loss over the interface length for 1 N, 10 N and 100 N of excitation amplitudes (left). Hysteresis shapes at the different local points of the contact interface (right).

Appendix B

Mode Shapes - Double layered beam test Structure (1Nm)

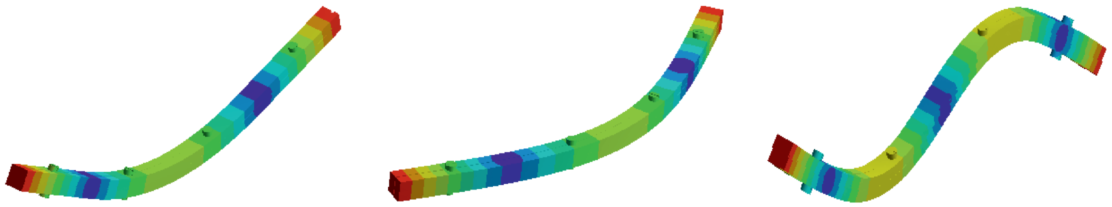

(a) Mode 1 -
Experiment: 362 Hz / 0.3 %
D-PDJ: 360 Hz / 0.3 %

(b) Mode 2 -
Experiment: 405 Hz / 0.04 %
D-PDJ: 403 Hz / 0.06 %

(c) Mode 3 -
Experiment: 827 Hz / 0.4 %
D-PDJ: 824 Hz / 0.4 %

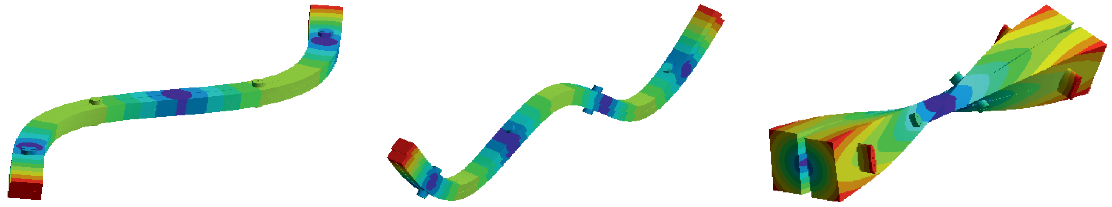

(d) Mode 4 -
Experiment: 1106 Hz / 0.03 %
D-PDJ: 1102 Hz / 0.04 %

(e) Mode 5 -
Experiment: 1560 Hz / 0.7 %
D-PDJ: 1540 Hz / 0.6 %

(f) Mode 6 -
Experiment: 1740 Hz / 0.1 %
D-PDJ: 1773 Hz / 0.15 %

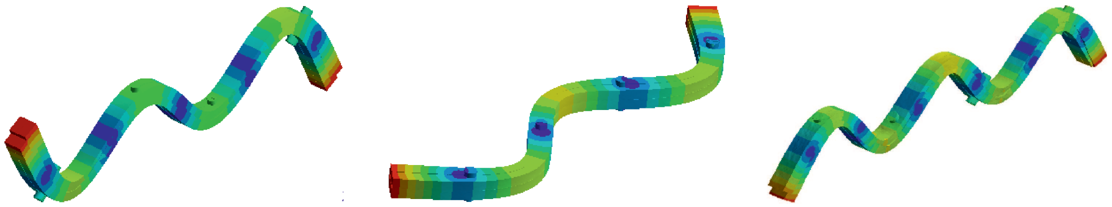

(g) Mode 7 -
Experiment: 1980 Hz / 0.3 %
D-PDJ: 2026 Hz / 0.3 %

(h) Mode 8 -
Experiment: 2145 Hz / 0.03 %
D-PDJ: 2136 Hz / 0.04 %

(i) Mode 9 -
Experiment: 2820 Hz / 0.3 %
D-PDJ: 2909 Hz / 0.2 %

Figure B.1: Mode shapes of double layered beam test structure fastened with 1Nm bolting torques. It is important to see that in-plane modes having less damping in comparison to out-of-plane modes.

Mode Shapes - Prototype Structure of Airbag ECU

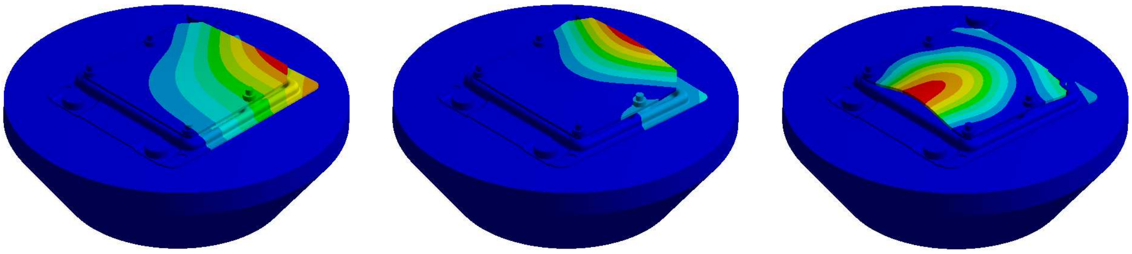

(a) Mode 1 -
Experiment: 321 Hz
D-PDJ: 319 Hz

(b) Mode 2 -
Experiment: 534 Hz
D-PDJ: 544 Hz

(c) Mode 3 -
Experiment: 813 Hz
D-PDJ: 799 Hz

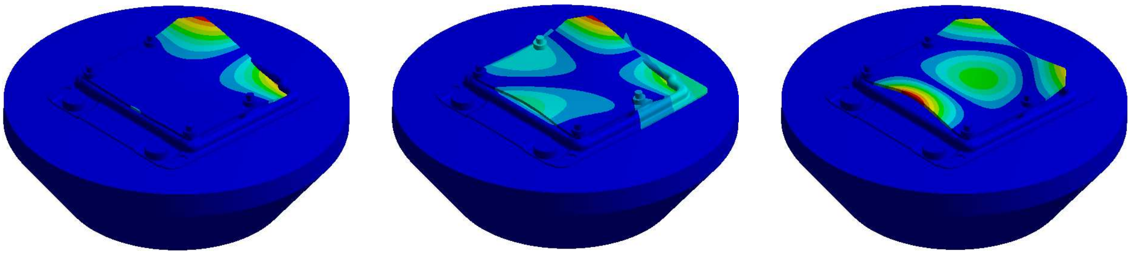

(d) Mode 4 -
Experiment: 1030 Hz
D-PDJ: 1018 Hz

(e) Mode 5 -
Experiment: 1190 Hz
D-PDJ: 1232 Hz

(f) Mode 6 -
Experiment: 1349 Hz
D-PDJ: 1347 Hz

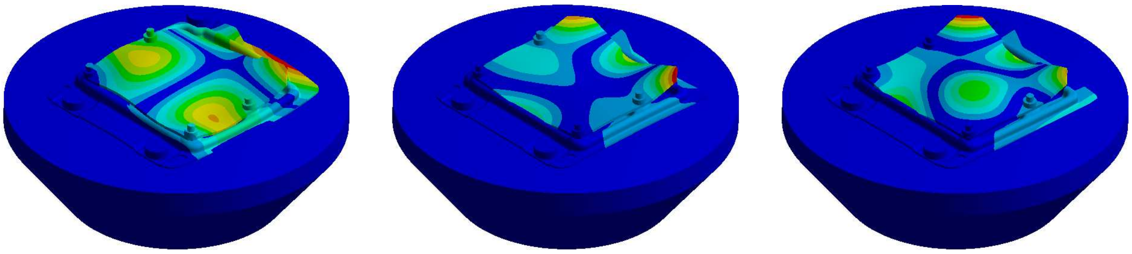

(g) Mode 7 -
Experiment: 1517 Hz
D-PDJ: 1517 Hz

(h) Mode 8 -
Experiment: 1768 Hz
D-PDJ: 1733 Hz

(i) Mode 9 -
Experiment: 2000 Hz
D-PDJ: 2007 Hz

Figure B.2: Mode shapes from modal analysis of Airbag ECU prototype test structure until 2 kHz. Till 1 kHz exists primary modes of PCB plate and after 1 kHz coupled modes exists.

Bibliography

[1] S. Adhikari. *Damping Models for Structural Vibration*. PhD thesis, Cambridge University Engineering Department, 2000.

[2] R. J. Allemang and D. L. Brown. A complete review of the complex mode indicator function (cmif) with applications. In *Proceedings of the International Conference on Noise and Vibration Engineering ISMA2006*, pages 3209–3246, Leuven, 2006.

[3] R. J. Allemang, D. L. Brown, and W. Fladung. Modal parameter estimation : A unified matrix polynomial approach. In *Proceedings of the International Modal Analysis Conference*, pages 501–514, 1994.

[4] A. Anandarajah. *Computational Methods in Elasticity and Plasticity: Solids and Porous Media*. Springer New York, 2010.

[5] S. Andersson, A. Soederberg, and S. Bjoerklund. Friction models for sliding dry, boundary and mixed lubricated contacts. *Tribology International*, 40:580–587, 2007.

[6] Inc Ansys. *Release 14 Documentation for Ansys*.

[7] J. F. Archard. Elastic deformation and the laws of friction. *Proceedings of Royal Society of London*, 243:190–205, 1957.

[8] M. R. Ashory. *High Quality Modal Testing Methods*. PhD thesis, Imperial College of Science, Technology and Medicine, London, 1999.

[9] C. F. Beards. *Structural Vibration: Analysis and Damping*. Arnold, 1996.

[10] W. Beitz, K. H. Kuettner, and H. Dubbel. *Dubbel - Tachenbusch fuer den Maschinenbau 17. Auflage*. Springer, 1990.

[11] G. Bfer. An isoparametric joint/interface element for finite element analysis. *International Journal for Numerical Methods in Engineering*, 21(4):585–600, 1985.

[12] E.K. Billups and M.N. Cavalli. 2d damping predictions of fiber composite plates: Layup effects. *Composites Science and Technology*, 68:727–733, 2008.

[13] U. Bittner. *Strukturakustische Optimierung von Axialkolbeneinheiten*. PhD thesis, Karlsruhe Institute of Technology, Karlsruhe, Germany, 2013.

[14] A. F. Bower and K. L. Johnson. The influence of strain hardening on cumulative plastic deformation in rolling and sliding line contact. *Journal of the Mechanics and Physics of Solids*, 37:471–493, 1989.

[15] T. M. Cameron and J. H. Griffen. An alternating frequency/time domain method for calculating the steady state response of nonlinear dynamic systems. *Journal of Applied Mechanics*, 56(1):149–154, 1989.

[16] A. Cardona, T. Coune, A. Lerusse, and M. Geradin. A multi harmonic method for non-linear vibration analysis. *International Journal for Numerical Methods in Engineering*, 37:1593–1608, 1994.

[17] A. Cardona, A. Lerusse, and A. Geradin. Fast fourier nonlinear vibration analysis. *Computational Mechanics*, 22:128–142, 1998.

[18] A. Carrella, D. J. Ewins, A. Colombo, and E. Bianchi. Identifying and quantifying structural nonlinearities from measured frequency response functions. In *Proceedings of the International Modal Analysis Conference- XXVIII*, Jacksonville, Florida, USA, 2010.

[19] T. K. Caughey and M. E. O'Kelly. Classical normal modes in damped linear dynamic systems. *Transactions of ASME, Journal of Applied Mechanics*, 32:583–588, 1965.

[20] W. R. Chang. An elastic-plastic contact model for a rough surface with an ion-plated soft metallic coating. *Wear*, 212:229–237, 1997.

[21] W. R. Chang, I. Etsion, and D. B. Bogy. An elastic-plastic model for the contact of rough surfaces. *Journal of Tribology*, 109(2):257–263, 1987.

[22] W. R. Chang, I. Etsion, and D. B. Bogy. Static friction coefficient model for metallic rough surfaces. *Journal of Tribology*, 110(1):57–63, 1988.

[23] G. Chen and David L. Russell. A mathematical model for linear elastic systems with structural damping. Technical Report MRC-TSR-2089, WISCONSIN UNIV-MADISON Mathematics Research Centre, 1980.

[24] Y. K. Cheung, S. H. Chen, and S. L. Lau. Application of the incremental harmonic balance method to cubic non-linearity systems. *Journal of Sound and Vibration*, 140(2):272–286, 1990.

[25] D. Cloutier, P. Avitabile, R. W. Bono, and M. A. Peres. Shaker/stinger effects on measured frequency response functions. In *Proceedings of the Twenty-Seveth International Modal Analysis Conference*, pages 197–203, February 2009.

[26] S. H. Crandall. The role of damping in vibration theory. *Journal of Sound and Vibration*, 11(1):3–18, 1970.

[27] L. Cveticanin. *Strongly Nonlinear Oscillators*. Springer International Publishing, 2014.

[28] P. R. Dahl. A solid friction model. Technical Report TOR-158(3107-18), DTIC Document, The Aerospace Corporation, EI Segundo, Calif, 1968.

[29] P. R. Dahl. Solid friction damping of mechanical vibrations. *Journal of Aircraft-American Institute of Aeronautics and Astronautics*, 14(12):1675–1682, 1976.

[30] H. H. Dai, M. Schnoor, and S. N. Atluri. A simple collocation scheme for obtaining

the periodic solution of the duffing equation and its equivalence to the high dimensional harmonic balance method : Subharmonic oscillations. *Computer Modeling in Engineering & Sciences*, 84(5):459–497, 2012.

[31] C. W. de Silva. *Vibration: Fundamentals and Practice*. CRC Press Tyalor and Francis Group, second edition, 2007.

[32] C. Canudas de Wit, H. Olsson, K. J. Astrom, and P. Lischinsky. A new model for control of systems with friction. *IEEE Transaction on Automatic Control*, 40(3):419–425, 1995.

[33] C. S. Desai, M. M. Zaman, J. G. Lightner, and H. J. Siriwardane. Thin-layer element for interfaces and joints. *International Journal for Numerical and Analytical Methods in Geomechanics*, 8(1):19–43, 1984.

[34] M. Eriten, A. A. Polycarpou, and L. A. Bergman. Physics-based modeling for partial slip behavior of spherical contacts. *International Journal of Solids and Structures*, 47:2554–2567, 2010.

[35] L. Gaul. The influence of damping on waves and vibrations. *Mechanical Systems and Signal Processing*, 13(1):1–30, 1999.

[36] L. Gaul and J. Lenz. Nonlinear dynamics of structures assembled by bolted joints. *Acta Mechanica*, 125:169–181, 1997.

[37] L. Gaul and R. Nitsche. The role of friction in mechanical joints. *Applied Mechanics Reviews*, 54(2):93–106, 2001.

[38] L. Gaul, J. Roseira, and J. Becker. Structural damping with friction beams. *Shock and Vibration*, 15:291–298, 2008.

[39] J. Geisler. *Numerische und experimentelle Untersuchungen zum dynamische Verhalten von Strukturen mit Fuegestellen*. PhD thesis, Technische Fakulitaet der Universitaet Erlangen-nuernberg, 2010.

[40] R. E. Goodman, Robert L. Taylor, and T. L. Brekke. A model for the mechanics of jointed rock. *Journal of the Soil Mechanics and Foundations Division*, 94(3):637–660, 1968.

[41] H. H. Gould and B. B. Mikic. Area of contact and pressure distribution in bolted joints. *Transactions of ASME, Journal of Manufacturing Science and Engineering*, 94(3):864–870, 1972.

[42] J. A. Greenwood. A unified theory of surface roughness. *Proceedings of Royal Society of London*, 393:133–157, 1984.

[43] J. A. Greenwood and J. B. P. Williamson. Contact of nominally flat surfaces. *Proceedings of Royal Society of London*, 295:300–319, 1966.

[44] J. A. Greenwood and J. B. P. Williamson. Developements in the theory of surface roughness. In *Surface Roughness Effects in Lubrication, 4th Leeds-Lyon Symposium on Tribology*, London, 1977.

[45] J. A. Greenwood and J. J. Wu. Surface roughness and contact: An apology. *Meccanica*, 36:617–630, 2001.

[46] M. Groper. Microslip and macroslip in bolted joints. *Experimental Mechanics*, 25(2):171–174, 1985.

[47] J. C. Halpin and J. L. Kardos. The halpin-tsai equations: A review. *Polymer Engineering and Science*, 16(5), 1976.

[48] H. Hanselka and U. Hoffmann. Damping characteristics of fibre reinforced polymers. *Technische Mechanik*, 10(2):91–101, 1999.

[49] S.W. Hudnut and D. D. L. Chung. Enhancing loss modulus of carbon fibre polymer matrix composites by addition of particles in interlaminar region. *Plastics, Rubber and Composites Processing Applications*, 25(2):77–81, 1996.

[50] G. M. Hulbert and I. Jang. Automatic time step control algorithms for structural dynamics. *Computer methods in applied mechanics and engineering*, 126:155–178, 1995.

[51] D. J. Inman. *Engineering Vibrations*. Prentice Hall, Englewood Cliffs, NewJersey 07632, 1996.

[52] L. Jezequel. Structural damping by slip in joints. *Journal of Vibration and Acoustics*, 105(4):497–504, 1983.

[53] K. L. Johnson. *Contact Mechanics*. Cambridge University Press, 1985.

[54] G. Prater Jr. and R. Singh. Eigenproblem formulation, solution and interpretation for non-proportionally damped continuous beams. *Journal of Sound and Vibration*, 143(1):125–142, 1990.

[55] N. Kikuchi and J. T. Oden. *Contact Problems in Elasticity: A Study of Variational Inequalities and Finite Element Methods*. Studies in Applied Mathematics. Society for Industrial and Applied Mathematics, 1988.

[56] M. C. Kim, H. J. Jung, and I. W. Lee. Solution of eigenvalue problems for non-classically damped systems with multiple frequencies. *Journal of Sound and Vibration*, 219(2):207–222, 1999.

[57] L. Kogut and I. Etsion. Elastic-plastic contact analysis of a sphere and a rigid flat. *Journal of Applied Mechanics*, 69(5):657–662, 2002.

[58] A. Konyukhov and K. Schweizerhof. *Computational Contact Mechanics : Geometrically Exact Theory for Arbitrary Shaped Bodies*. Springer-Verlag Berlin Heidelberg, 2013.

[59] V. Lampaert, J. Swevers, and F. Al-Bender. Modification of the leuven integrated friction model structure. *IEEE Transactions on Automatic Control*, 47(4):683–687, 2002.

[60] S. L. Lau and Y. K. Cheung. Amplitude incremental variational principle for non-linear vibration of elastic systems. *Journal of Applied Mechanics*, 48(4):959–964,

1981.

[61] T. A. Laursen and J. C. Simo. A continuum-based finite element formulation for the implicit solution of multibody, large deformation-frictional contact problems. *International Journal for Numerical Methods in Engineering*, 36:3451–3485, 1993.

[62] B. J. Lazan. Review of structural damping mechanism. Technical report, Wright Air Development Center, 1961.

[63] M. Lee and M. Richardson. Determining the accuracy of modal parameter estimation methods. In *Proceedings of 10th International Modal Analysis Conference*, 1992.

[64] J. Lenz and L. Gaul. The influence of microslip on the dynamic behaviour of bolted joints. In *Proceedings of IMAC XIII*, number 13, pages 248–254, Nashville, 1995.

[65] L. Liu, E. H. Dowell, and K. C. Hall. A novel harmonic balance analysis for the van der pol oscillator. *International Journal of Non-Linear Mechanics*, 42:2–12, 2007.

[66] L. Liu, J. P. Thomas, E. H. Dowell, P. Attar, and K. C. Hall. A comparison of classical and high dimensional harmonic balance approach for a duffing oscillator. *Journal of Computational Physics*, 215:298–320, 2006.

[67] M. Mayer. *Zum Einfluss von Fuegestellen auf das dynamische Verhalten zusammengesetzter Strukturen*. PhD thesis, Universitaet Stuttgart, Stuttgart, Germany, 2007.

[68] M. H. Mayer and L. Gaul. Segment-to-segment contact elements for modelling joint interfaces in finite element analysis. *Mechanical Systems and Signal Processing*, 21(2):724–734, 2007.

[69] K. G. McConnell and P. Cappa. Transducer inertia and stinger stiffness effects on frf measurements. *Mechanical Systems and Signal Processing*, 14(4):625–636, 2000.

[70] S. Meyer. *Modellbildung und Identifikation von lokalen nichtlinearen Steifigkeits- und Daempfungseigenschaften in komplexen strukturdynamischen Finite Elemente Modellen*. PhD thesis, Kassel University, 2003.

[71] R. D. Mindlin. Compliance of elastic bodies in contact. *Journal of Applied Mechanics*, 16:259–268, 1949.

[72] R. D. Mindlin, W. P. Mason, J. F. Osmer, and H. Deresiewicz. Effects of an oscillating tangential force on the contact surfaces of elastic spheres. In *Proceedings of 1st US National Congress of Applied Mechanics*, pages 203–208, Chicago, Illinois, USA, 1951.

[73] D. Muhs, H. Wittel, and D. Jannasch. *Roloff/Matek Maschinenelemente*. Vieweg Verlag, Wiesbaden, 18 edition, 2007.

[74] S. Neumark. Concept of complex stiffness applied to problems of oscillations with viscous and hysteretic damping. Technical report, Aeronautical Research Council, 1962.

[75] D. E. Newland. *Mechanical Vibration Analysis and Computation*. Longman, Harlow and John Wiley, Newyork, 1989.

[76] N. M. Newmark. A method of computation for structural dynamics. *Journal of Engineering Mechanics*, 85:67–94, 1959.

[77] R. G. Ni and R. D. Adams. The damping and dynamic moduli of symmetric laminated composite beams–theoretical and experimental results. *Journal of Composite Materials*, 18:104–121, 1984.

[78] M. E. J. O'Kelly. *Vibration of Viscously Damped Linear Dynamic Systems*. PhD thesis, California Institute of Technology, Pasadena, California, 1964.

[79] R. A. Onions and J. F. Archard. The contact of surfaces having a random structure. *Journal of Physics D: Applied Physics*, 6:289–304, 1973.

[80] G. N. Pande and K. G. Sharma. On joint/interface elements and associated problems of numerical ill-conditioning. *International Journal for Numerical and Analytical Methods in Geomechanics*, 3(3):293–300, 1979.

[81] P. Papadopoulos and J. M. Solberg. A lagrange multiplier method for the finite element solution of frictionless contact problems. *Mathematical and Computer Modelling*, 28:373–384, 1998.

[82] Z. K. Peng, Z. Q. Lang, S. A. Billings, and G. R. Tomlinson. Comparison between harmonic balance and nonlinear output frequency response function in nonlinear system analysis. *Journal of Sound and Vibration*, 311:56–73, 2008.

[83] N. Peyret and J. L. Dion. Energy dissipation by micro-slip in an assembly, analytic and experimental approach. In *Proceedings of the ASME 2011 International Design Engineering Technical Conferences & Computers and Information in Engineering Conference IDETC/CIE*, Washington, DC, USA, August 28-31 2011.

[84] A. S. Phani. On the necessary and sufficient conditions for the exsistance of the classical normal modes in damped linear dynanmic systems. *Journal of Sound and Vibration*, 264(741-745), 2003.

[85] A. S. Phani. *Damping identification in linear vibrations*. PhD thesis, Cambridge University Engineering Department, 2004.

[86] A. W. Phillips, R. J. Allemang, and W. A. Fladung. The complex mode indicator function (cmif) as a parameter estimation method. In *Proceedings of the 16th International Modal Analysis Conference,*, pages 705–710, Santa Barbara, CA, USA, 1998.

[87] W. Pinsker. Structural damping. *Journal of the Aeronautical Sciences (Institute of the Aeronautical Sciences)*, 16(11):699–704, 1949.

[88] A. A. Polycarpou and I. Etsion. Analytical approximations in modeling contacting rough surfaces. *Journal of Tribology*, 121(2):234–239, 1999.

[89] V. L. Popov. *Contact mechanics and Friction*. Springer, 2010.

[90] U. Prells and M. I. Friswell. A measure of non-proportional damping. *Journal of Sound and Vibration*, 14(2):125–137, 2000.

[91] M. S. Qatu. *Vibration of Laminated Shells and Plates*. Elsevier B.V, 2004.

[92] M. Rades. A comparison of some mode indicator functions. *Mechanical Systems and Signal Processing*, 8(4):459–474, 1994.

[93] M. Rades. Performance of various mode indicator functions. *Shock and Vibration*, 17:473–482, 2010.

[94] M. D. Rao, R. Echempati, and S. Nadella. Dynamic analysis and damping of composite structures embedded with viscoelastic layers. *Composites Part B: Engineering*, 28:547–554, 1997.

[95] L. Rayleigh. *Theory of Sounds (two volumes)*. Dover Publications, Newyork, second edition, 1945.

[96] M. H. Richardson and D. L. Formenti. Parameter estimation from frequency response measurements using rational fraction polynomials. In *Proceedings of the IMAC Conference*, Orlando, FL, 1982.

[97] D. Ross, E. E. Ungar, and E. M. Kerwin. Damping of plate flexural vibrations by means of viscoelastic laminae. In T.E. Ruzicka, editor, *Structural Damping Conference*, pages 48–88, Newyork, 1959.

[98] K. Schweizerhof, J. Neumann, and S. Kizio. On time integration error estimation and adaptive time stepping in structural dynamics. In *PAMM, Proceedings in Applied Mathematics and Mechanics*, volume 4, pages 35–38, 2004.

[99] K. Sharma and C. Desai. Analysis and implementation of thin-layer element for interfaces and joints. *Journal of Engineering Mechanics*, 118(12):2442–2462, 1992.

[100] Xi Shi and A. A. Polycarpou. Measurement and modeling of normal contact stiffness and contact damping at the meso scale. *Journal of Vibration and Acoustics*, 127(1):52–60, 2005.

[101] J. C. Simo and T. A. Laursen. An augmented lagrangian treatment of contact problems involving friction. *Computers & Structures*, 42(1):97–116, 1992.

[102] J. C. Simo and R. L. Taylor. Consistent tangent operators for rate-independent elastoplasticity. *Computer Methods in Applied Mechanics and Engineering*, 48(1):101–118, 1985.

[103] J. C. Simo, P. Wriggers, and R. L. Taylor. A perturbed lagrangian formulation for the finite element solution of contact problems. *Computer Methods in Applied Mechanics and Engineering*, 50(2):163–180, 1985.

[104] W. W. Soroka. Note on the relations between viscous and structural damping coefficients. *Journal of the Aeronautical Sciences*, 16(7):409–410, 1949.

[105] N. R. Sottos, J. M. Ockers, and M. Swindeman. Thermoelastic properties of plain weave composite for multilayer circuit board applications. *Journal of Electronic Packaging, ASME*, 121:37–43, 1999.

[106] D. Steinberg. *Vibration Analysis for Electronic Component*. Wiley-Interscience,

Newyork, 1988.

[107] R. Stribeck. Die Wesentlichen Eigenschaften der Gleit - und Rollenlager. *Zeitschrift des Vereins deutscher Ingenieure*, 46:1342–1348 and 1432–1437, 1902.

[108] C. T. Sun and J. M. Bai. Vibration of multi-degree-of-freedom systems with non-proportional viscous damping. *International Journal of Mechanical Sciences*, 37(4):441–455, 1995.

[109] W. Sun and J. T. Tzeng. Effective mechanical properties of EM composite conductors: an analytical and finite element modeling approach. *Composite Structures*, 58(4):411–421, 2002.

[110] S. R. Swanson. Hertzian contact of orthotropic bodies. *International Journal of Solids and Structures*, 41:1945–1959, 2004.

[111] J. Swevers, F. Al-Bender, C. Ganseman, and T. Prajogo. An integrated friction model structure with improved presliding behavior for accurate friction compensation. *IEEE Transaction on Automatic Control*, 45(4):675–686, 2000.

[112] M. H. Tsai and K. C. Chang. A study on modal strain energy method for viscoelastically damped structures. In *WCEE 12*, 2000.

[113] J. R. Turner. Contact of a transversely isotropic half-space or between two transversely isotropic bodies. *International Journal of Solids and Structures*, 16:409–419, 1979.

[114] E. E. Ungar. Loss factors of viscoelastically damped beam structures. *The Journal of the Acoustical Society of America*, 34(2), 1962.

[115] E. E. Ungar. Energy dissipation at structural joints; mechanisms and magnitudes. Technical Documentary Report FDL-TDR-64-98, Air Force Flight Dynamics Lab, Wright-Patterson Air Force Base, OH, 1964.

[116] M. Urabe and A. Reiter. Numerical computation of non-linear forced oscillations by galerkin's procedure. *Journal of Mathematical Analysis and Applications*, 14:107–140, 1966.

[117] G. von Groll and D. J. Ewins. The harmonic balance method with arc-length continuation in rotor/stator contact problems. *Journal of Sound and Vibration*, 241(2):223–233, 2001.

[118] D. Wagg and S. Neild. *Nonlinear vibration with Control*. Springer International Publishing, 2010.

[119] D. J. Whitehouse and J. F. Archard. The properties of random surfaces of significance in their contact. *Proceedings of Royal Society of London*, 316:97–121, 1970.

[120] J. R. Wills. Hertzian contact of anisotropic bodies. *Journal of the Mechanics and Physics of Solids*, 14(3):163–176, 1966.

[121] K. Worden and G. R. Tomlinson. Nonlinearity in experimental modal analysis. *Philosophical Transactions of the Royal Society of London*, 359:113–130, 2001.

[122] P. Wriggers. Finite element algorithms for contact problems. *Archives of Computational Methods in Engineering*, 2:1–49, 1995.

[123] P. Wriggers. Finite element methods for contact problems with friction. *Tribology International*, 29:651–658, 1996.

[124] P. Wriggers. *Computational Contact Mechanics*. Springer-Verlag Berlin Heidelberg, second edition, 2006.

[125] P. Wriggers and O. Scherf. Adaptive finite element techniques for frictional contact problems involving large elastic strains. *Computer Methods in Applied Mechanics and Engineering*, 151:593–608, 1998.

[126] V. A. Yastrebov. *Numerical Methods in Contact Mechanics*. John Wiley & Sons, 2013.

[127] L. F. Zeng, N. E. Wiberg, X. D. Li, and Y. M. Xie. A posteriori local error estimation and adaptive time-stepping for newmark integration in dynamic analysis. *Earthquake Engineering & Structural Dynamics*, 21(7):555–571, 1992.

[128] Z. L. Zhang. Explicit consistent tangent moduli with a return mapping algorithm for pressure-dependent elastoplasticity models. *Computer Methods in Applied Mechanics and Engineering*, 121(4):29–44, 1995.

[129] H. H. Ziada and A. K. Abd. Load pressure distribution and contact areas in bolted joints. *Institution of Engineers (India)*, 61:93–100, 1980.

[130] O. C. Zienkiewicz, R. L. Taylor, and J. Z. Zhu. *The Finite Element Method: Its Basis and Fundamentals*. Butterworth-Heinemann, 2000.

Curriculum Vitae

Family Name	Sharma
First Name	Anuj
Date of Birth	20.08.1987
Place of Birth	Shyamnagar, India
Nationality	Indian

Education

2002-2004	Senior Secondary School Kendriya Vidyalaya No. 1 Uppal Hyderabad, Telangana, India.
2004-2008	Bachelor of Technology Mechanical Engineering CVSR College of Engineering, JNT University Hyderabad, Telangana, India.
2009-2010	Master of Science Computational Mechanics Swansea University, Swansea, United kingdom.
2010-2011	Master of Science Computational Mechanics Stuttgart University, Stuttgart, Germany.
2012-2016	Doctoral Thesis Department of Mechanical Engineering Technical University Darmstadt Darmstadt, Germany.